1-1-2015

Study About Petrophysical And Geomechanical Properties Of Bakken Formation

Jun He

STUDY ABOUT PETROPHYSICAL AND GEOMECHANICAL PROPERTIES OF BAKKEN FORMATION

by

Jun He

Bachelor of Science, Southwest Petroleum University, 1995
Master of Science, University of North Dakota, 2013

A Dissertation

Submitted to the Graduate Faculty

of the

University of North Dakota

In partial fulfillment of the requirements

for the degree of

Doctor of Philosophy

Grand Forks, North Dakota
December
2015

This dissertation, submitted by Jun He in partial fulfillment of the requirements for the Degree of Doctor of Philosophy from the University of North Dakota, has been read by the Faculty Advisory Committee under whom the work has been done and is hereby approved.

Kegang Ling — 12/4/2015
Kegang Ling, Chairperson — Date

Richard LeFever — 12/4/2015
Richard LeFever — Date

12/4/2015
Yun Ji — Date

Clement Tang — 12/4/2015
Clement Tang — Date

12/4/2015
Yanjun Zuo — Date

This dissertation is being submitted by the appointed advisory committee as having met all of the requirements of the Graduate School of the University of North Dakota, and is hereby approved.

Dr. Wayne Swisher,
Dean of the Graduate School

December 4, 2015
Date

Title	Study about Petrophysical and Geomechanical Properties of Bakken Formation
Department	Petroleum Engineering
Degree	Doctor of Philosophy

In presenting this dissertation in partial fulfillment of the requirements for a graduate degree from the University of North Dakota, I agree that the library of this University shall make it freely available for inspection. I further agree that permission for extensive copying for scholarly purposes may be granted by the professor who supervised my dissertation work or, in his absence, by the Chairperson of the department or the dean of the Graduate School. It is understood that any copying or publication or other use of this dissertation or part thereof for financial gain shall not be allowed without my written permission. It is also understood that due recognition shall be given to me and to the University of North Dakota in any scholarly use which may be made of any material in my dissertation.

Jun He

December 4, 2015

TABLE OF CONTENTS

LIST OF FIGURES

LIST OF TABLES

ACKNOWLEDGMENTS

During the past several years at University of North Dakota (UND), I have gotten tons of help in the process of pursuing my Ph.D. degree. I want to acknowledge them for their generosity and kindness.

Firstly, I would like to express my sincere gratitude to my advisor Dr. Kegang Ling for the continuous support of my Ph.D. study and related research, for his patience, motivation, and immense knowledge. His guidance helped me in all the time of research and writing of this thesis. I could not have imagined having a better advisor and mentor for my Ph.D. study.

Besides my advisor, I would like to thank the rest of the members of my committee: Dr. Richard Lefever, Dr. Yun Ji, Dr. Clement Tang, and Dr. Yanjun Zuo, for their insightful comments and encouragement, but also for the hard question which induced me to widen my research from various perspectives.

My sincere thanks also goes to all my friends at the UND Petroleum Engineering Department, the Harold Hamm School of Geology and Geology Engineering, and the North Dakota Geological Survey. In particular, I am grateful to Dr. Zhengwen Zeng from the Harold Hamm School of Geology and Geology Engineering, who provide me an

opportunity to join his research team; to Julia Lefever from the North Dakota Geological Survey, who gave access to the core laboratory and research facilities. Without their precious support it would not be possible to conduct this research.

This research is supported in part by the U.S. Department of Energy (DOE) under award number DE-FC26-08NT0005643. I thank my fellow labmates, Hong Liu and Dr. Peng Pei, for the sleepless nights we were working together before deadlines, and for all the fun we have had.

Last but not the least, I truly appreciate my family, without their support I would not have realized my dream.

ABSTRACT

The objectives of this research are to measure the petrophysical and geomechanical properties of the Bakken Formation in North Dakota Williston Basin in to increase the success rate of horizontal drilling and hydraulic fracturing so as to improve the ultimate recovery of this unconventional crude oil resource from the current 3% to a higher level.

Horizontal drilling with hydraulic fracturing is a required well completion technique for economic exploitation of crude oil from Bakken Formation in the North Dakota Williston Basin due to its low porosity and low permeability. The success of horizontal drilling and hydraulic fracturing depends on knowing the petrophysical and geomechanical properties of the rocks.

A dataset of geomechanical and petrophyscial properties of the Bakken Formation rocks in the studied areas is generated, after petrophysical properties (including Density, Velocity, Porosity, and Permeability) and geomechanical properties (including uniaxial compressive strength, Young's modulus, Poisson's ratio, and Biot's coefficience) were measured. To obtain those parameters, we not only used regular methods but also proposed some new methods for solving special measurement problems which may also be faced by other tight rock researchers.

The results of this research can be used as a guideline and reference to optimize horizontal drilling and fracturing design to increase estimated ultimate recovery (EUR) in unconventional shale oil and gas productions.

CHAPTER I

INTRODUCTION

1.1. Motivations

After more than one hundred years of development and production, conventional oil and gas reserves are depleting significantly on a worldwide basis. In order to meet the increasing demand of hydrocarbon energy, it is essential to develop unconventional resources. Shale oil and gas become crucial supplements to the conventional hydrocarbon reservoirs. The Bakken Formation in the Williston Basin is an unconventional oil resource, which holds 3.65 billion barrels of technically recoverable oil, 1.85 trillion cubic feet of associated/dissolved gas, and 148 million barrels of natural gas liquids in Montana and North Dakota (Pollastro et al., 2008). Since the first oil production occurred in the Bakken Formation on the Antelope Anticline in 1953, the Bakken Formation has been produced for almost 60 years. But it has never become one of the major target reservoirs until 2006, after its oil production has been highly increased by new techniques, such as hydraulic fracturing and horizontal drilling.

Producing hydrocarbons from the Bakken Formation is challenging because of the low porosity and permeability. Thus fracturing completion is a critical component of

developing the Bakken Formation, indeed every shale play throughout the U.S. and Canada. Without fracturing, this resource could not be produced economically.

Hydraulic fracturing is the process of improving the ability of oil to flow through a rock formation by creating fractures. The process involves creating fractures and pumping into the fractures a mixture of water and additives that include various sizes of sand or ceramic particles called proppants that are designed to "prop" the fractures open, creating greater conductivity for fluids flowing to the wellbore. However, within the Bakken Formation, field data suggest that operators are unable to sustain propped fractures spatially or temporally (Vincent, 2011), resulting in significantly decreased oil production. The success of hydraulic fracturing has to rely on the knowledge of rock properties and in-situ stress. Although numerous investigations have been conducted to better understand rock properties of shale and the fluids properties and flow behavior in the Bakken Formation under reservoir condition, the progresses in rock and fluid characterizations and fluid-rock interaction description are impeded by the availability of experimental data on Bakken sample. One element that contributes to the rare experimental data of the Bakken Formation is the low porosity and extremely low permeability feature of the Bakken sample. Conventional methods to analyze core porosity and permeability do not work or cannot be afforded due to expensive cost and time consuming when they are applied to analyze the Bakken sample.

The objectives of this study are to measure the petrophysical and geomechanical

properties of the Bakken Formation in Williston Basin, North Dakota, USA to increase the success rate of horizontal drilling and hydraulic fracturing so as to improve the recovery factor of this unconventional oil resource. Some new methods were also developed to measure those properties for tight Bakken samples.

1.2. Dissertation Outline

Following this introductory chapter, Chapter 2 is a review of the Williston Basin and the Bakken Formation. It firstly provides an overview of the Williston Basin; then reviews the geology and the production history of the Bakken Formation.

Chapter 3 details the laboratory work on the Bakken Formation. This Chapter is divided into four main parts. The first is focused on the samples selection, the experiment schedule, and experiment facility description. The second part shows how to prepare samples for the following measurement. The third part is the measurement of the petrophysical parameters, such as porosity and permeability, of the samples. The last part in this chapter is the measurement of the geomechnical parameters, such as elastic moduli, compressibility, Biot's coefficient, and strength, of the samples.

Finally, conclusions of the study are presented in Chapter 4. The last chapter also gives recommendations for future work.

CHAPTER II

BAKKEN FORMATION REVIEW

2.1. Williston Basin

The Williston Basin (Figure 2.1) is an intracratonic sedimentary basin, which covers surface areas between 120,000 and 240,000 square miles in southern Saskatchewan, southwestern Manitoba, eastern Montana, western North Dakota, and northwestern South Dakota (Landes, 1970). The basin reaches approximately 475 miles north-south from southern Saskatchewan to northern South Dakota, and 300 miles east-west from eastern Montana to western North Dakota (Look2See1, 2015). The major structural features in the North Dakota portion include the Nesson anticline, the Little Knife anticline, the Billings anticline, and part of the Cedar Creek anticline (Heck et al., 2002).

This roughly oval-shaped basin began to subside during the Ordovician Period around 495 million years ago (Heck et al., 2002). After underwent episodic subsidence throughout the rest of the Phanerozoic Eon, the Williston Basin contains an incomplete sedimentary record from the Cambrian through the Quaternary on a surface of weathered basement rocks. The sedimentary rock column is more than 15,000 feet thick in thedeepest section. The sediments in the Williston Basin are divided into six major

sequences based on the transgression and regression events, and each sequence contains couple formations (Figure 2.2). These sequences are, in ascending order, the Sauk, Tippecanoe, Kaskaskia, Absaroka, Zuni, and Tejas (Sloss, 1963).

Figure 2.1 Williston Basin and its major structures (Heck et al, 2002).

In the Williston Basin, the most produced hydrocarbons are from carbonate reservoirs from the Ordovician through the Mississippian. Although several companies explored for oil starting in 1917, the boom in leasing and drilling activities in the Williston Basin is led by the first commercial oil discovery well, Amerada's Clarence Iverson No.1, which struck commercial quantities of oil south of Tioga, ND at a depth greater than 11,000 feet below the surface in 1951. This discovery well was completed in the Silurian Interlake Formation but subsequent development on the anticline focused on the Mississippian

Madison Group. The Williston Basin became a major oil producing region in the 1950s. In addition, it has been experiencing a steady and substantial increase in oil production since 2004, when the application of horizontal drilling technologies and stage fracturing facilitated the ability to extract oil from previously unviable deposits, the Bakken shales.

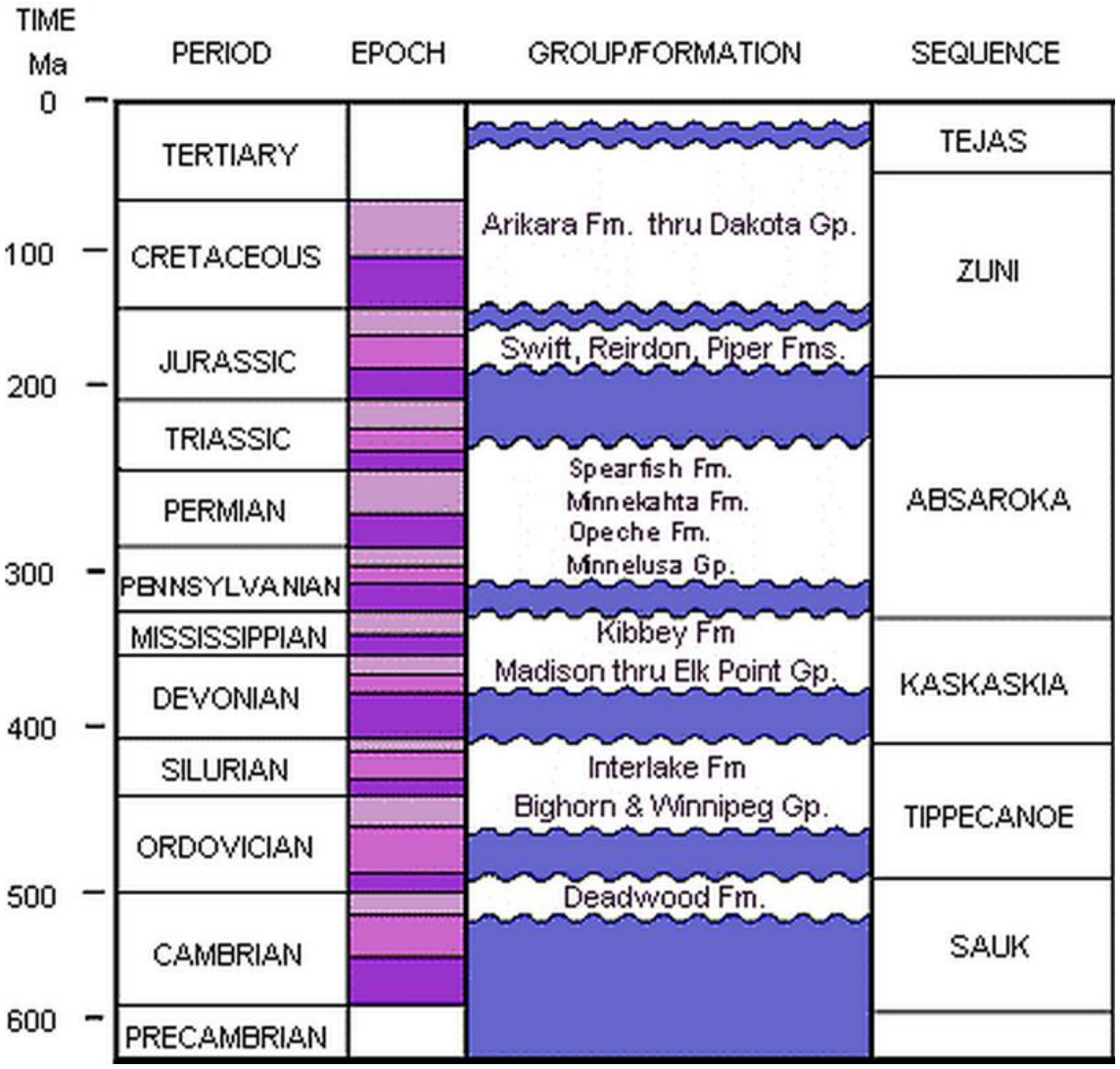

Figure 2.2 Time-stratigraphic column of the North Dakota Williston Basin (Fischer, 2005).

2.2. Bakken Formation

The Bakken Formation, a large subsurface formation within the Williston Basin (Figure 2.3), is known for its rich petroleum deposits. Currently, the Bakken Formation is considered the main reservoir and source of a huge portion of the oil generated and produced in the Williston Basin.

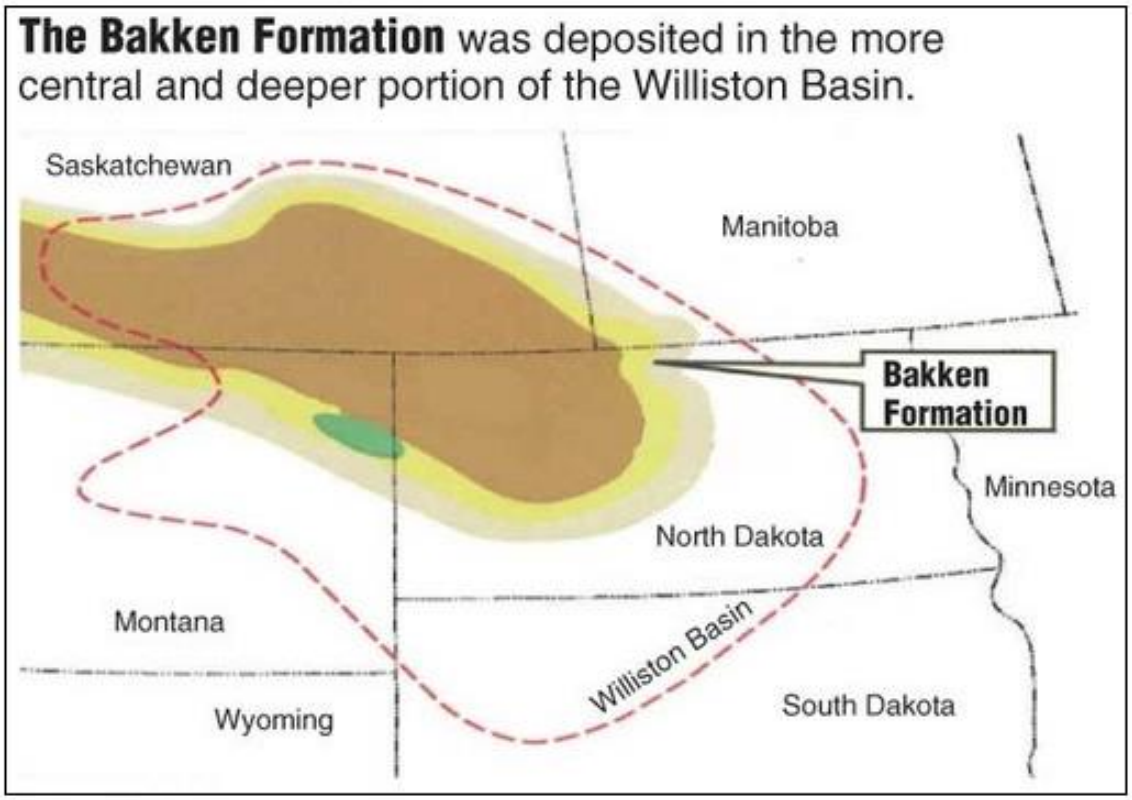

Figure 2.3 Map of the Bakken Formation (Dukes, 2013)

2.2.1. Geology of Bakken Formation

The Bakken Formation formed during the late Devonian and early Mississippian age, which is included in the Kaskaskia Sequence (Hester and Schmoker 1985). The Bakken Formation underlies the Mississippian Lodgepole Formation and overlies the Devonian

Three Forks Formation conformably in the Williston Basin, except that the unconformable contact exists at the flanks of the basin between the Bakken Formation and the Three Forks Formation.

With an offshore marine environment (LeFever, 1991), the Bakken Formation consists of three members: the upper shale, the lithologically variable middle member, and the lower shale. The thin and naturally fractured upper and lower shales have rich organic content, which are considered both a source and reservoir. In North Dakota, the middle member of the Bakken Formation is mainly gray interbedded siltstones and sandstones with a maximum thickness of 85 feet occurring at depths of approximately 9,500 to 10,000 feet (Heck et al., 2002).

2.2.2. Production History of Bakken Formation

The Bakken Formation is very thin compared to other oil producing horizons, but it has recently attracted much attention because the extremely high hydrocarbon content of the Bakken Formation has placed it among the richest hydrocarbon source rocks in the world. The estimate of original oil in place (OOIP) for the Bakken Formation ranges from 200 to more than 400 billion barrels (Price, 2000). This unconventional reserve in the Bakken Formation becomes increasingly important when the growth rate of demand outpaces the one of new reserves on oil and gas.

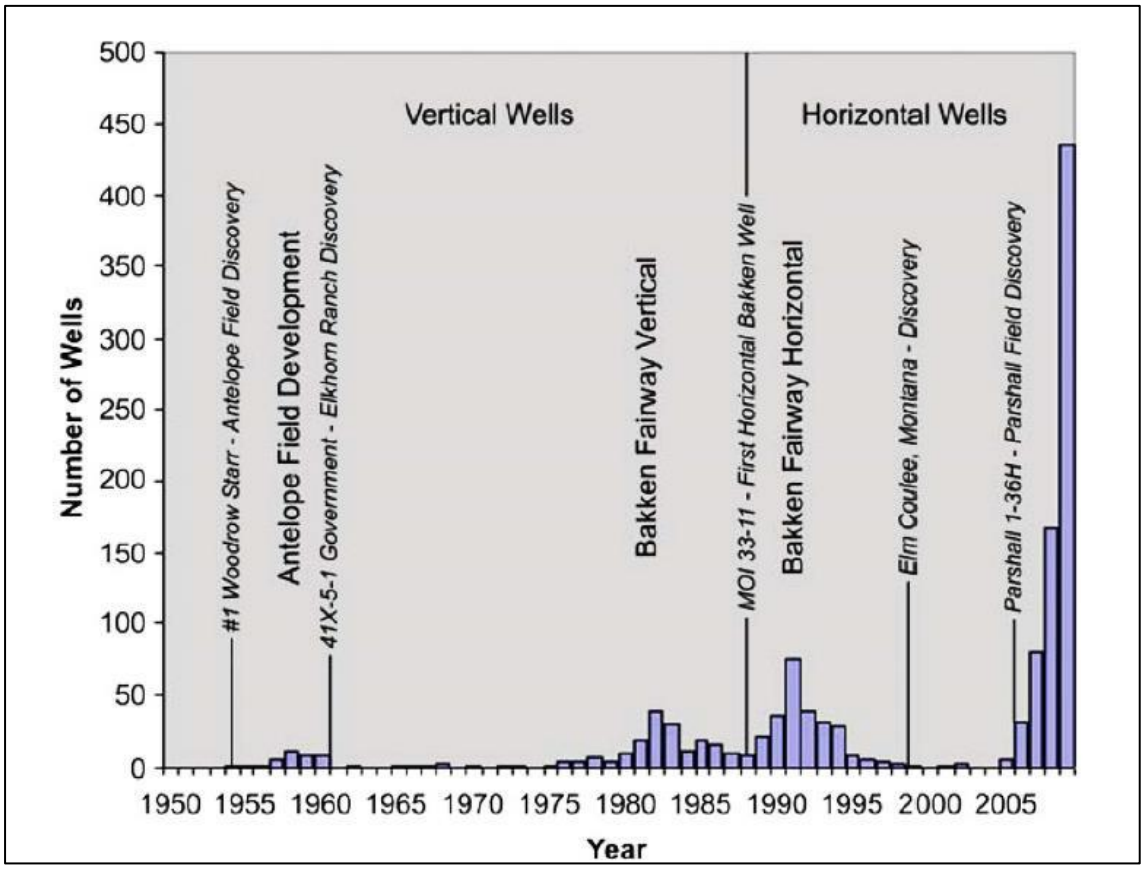

Figure 2.4 Development history of the Bakken in Williston Basin (Nordeng, 2010).

During the period from 1953 to 1987, vertical wells were drilled to recover the crude oil from the Bakken Formation (Figure 2.4). The wells that encountered natural fractures were successful, but those wells displayed high production at the beginning and soon dropped rapidly to a steady, low level production rate. In the beginning of 1990s, the horizontal drilling was extensively practiced in the Bakken Formation (Carlisle et al., 1996). These wells performed quite well in the "Bakken Fairway" area in North Dakota. Due to the high investment, the horizontal wells are usually drilled for two purposes: increasing the drainage area in thin layers, and/or connecting more fractures in naturally fractured reservoirs (Economides and Boney, 2000). The success of horizontal well

depends on two factors: (1) vertical permeability and (2) wellbore orientation with respect to natural fractures (Karcher et al., 1986; Mukherjee and Economides, 1991; Hudson and Matson, 1992). Using horizontal drilling has improved the performance to a certain degree, especially with the successful production of oil from the upper shale of the Bakken Formation.

The horizontal well also encountered new challenges: the borehole instability and the wellbore interference. The large investment and high risk in drilling horizontal well in the Bakken Formation kept the exploration and production activities at a low level until 2000 when new well construction technique was developed in Richland County, Montana (Lantz et al., 2007), which later extended to western North Dakota. This new technique combines horizontal drilling with hydraulic fracturing. Since 2006 a significant amount of oil has been successfully produced from the Bakken Formation.

CHAPTER III

METHODOLOGY

3.1. Sample Selection

As shown in Figure 3.1, the Bakken Formation in U.S. was divided into five continuous assessment units (AU): (1) Elm Coulee-Billings Nose AU, (2) Central Basin-Poplar Dome AU, (3) Nesson-Little Knife Structural AU, (4) Eastern Expulsion Threshold AU, and (5) Northwest Expulsion Threshold AU. The boundaries of these assessment units are consistent with the major structures in the area, and support the aforementioned geological heterogeneity.

The Bakken core samples were chosen as the specimens from eight wells in the five AU. These wells are chosen based on the thickness of the Bakken Formation and the condition of the core. The corresponding North Dakota Industrial Commission (NDIC) file number, the map number, and the tops of the members of the Bakken Formation are listed in Table 3.1 for each well.

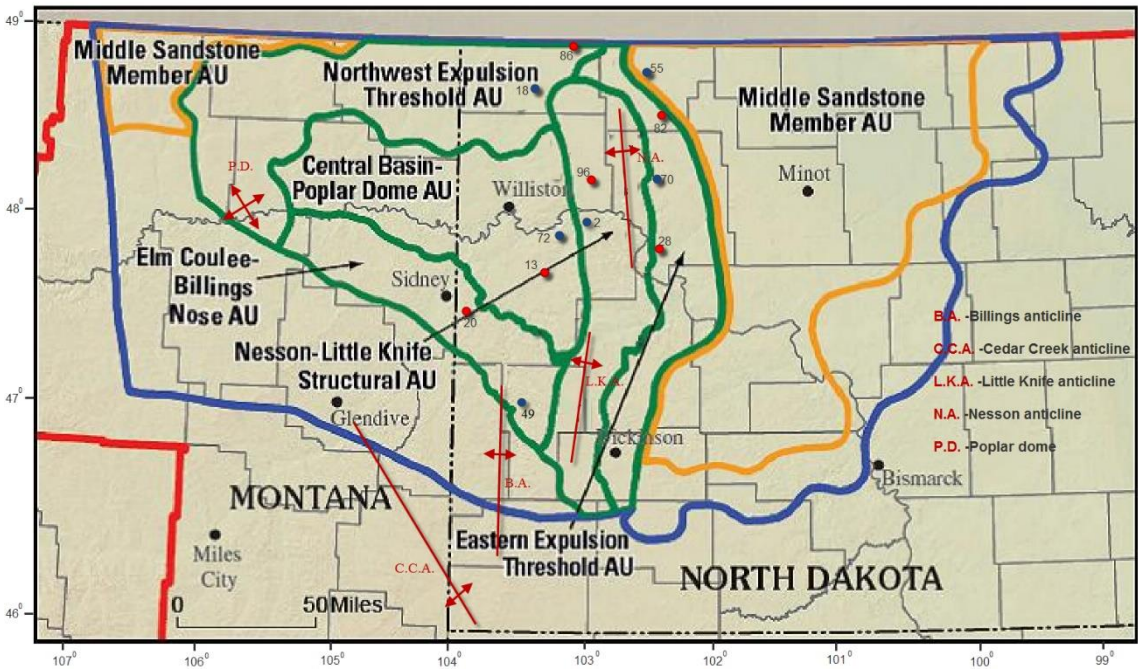

Figure 3.1 Five continuous assessment units of the Bakken Formation (Modified from Pollastro et al., 2008).

Table 3.1 Wells providing core samples for test in this study

Map Number	NDIC File Number	Assessment Unit	Top of Formation (ft)		
			Upper Bakken	Middle Bakken	Lower Bakken
2	11617	Nesson-Little Knife Structural AU	10310	10330	10380
13	15923	Central Basin-Poplar Dome AU	10985	11005	11050
18	16089	Northwest Expulsion Threshold AU	8595	8610	8675
20	16174	Elm Coulee-Billings Nose AU	10673	10683	10712
70	16862	Eastern Expulsion Threshold AU	8803	8820	8850
72	16985	Central Basin-Poplar Dome AU	10486	10510	10550
86	17450	Northwest Expulsion Threshold AU	7300	7355	7415
96	16771	Nesson-Little Knife Structural AU	10288	10307	10378

3.2. Sample Prepare and Main Equipment

Our literature review indicates that numbers of core analysis on shale are limited due to the difficulty in preparing shale plug from drilling cores. The brittle nature of shale makes the successful rate of preparing plug very lower from drilling core. Usually the successful rate ranges from 0 to 10%. To overcome the sampling difficulty, the freezing sample method is used in preparing the plug for core analysis. The core was pre-cooled at low temperature for several days, and drilled with the equipment show in Figure 3.2. The core plugs were prepared into cylindrical pieces of one inch in diameter and two inches in length. Two hundred and forty specimens in total were used in the test, of which 42 from Upper Bakken, 140 from Middle Bakken, and 58 from Lower Bakken.

Figure 3.2 Core plug sampling system used in this study

First, the dry bulk density of the specimens was measured after the specimens were oven

dried and weighed; then the non-destructive properties, porosity, permeability, velocity, elastic moduli, compressibility, and Biot's coefficient, were measured step by step; at the end the destructive properties (compressive strength) was measured.

Figure 3.3 AutoLab-1500 used in this study.

The main equipment that is used to perform our experiments is AutoLab-1500, which is made by New England Research Inc. AutoLab-1500 is a complete laboratory system with three integrated components: 1). a pressure vessel and four associated pressure intensifiers to generate pressures on the test sample; 2). an electronics console that interfaces with the mechanical system to precisely control the state of pressure and to condition and amplify signals from the transducers and devices measuring force, pressure,

displacement, strain, and temperature; and 3). a data acquisition system which generates reference signals to control the equipment, to acquire data, and to process the data collected on the experiment.

AutoLab-1500 supports a comprehensive suite of physical rock properties measurements as a function of the state of stress and temperature (AutLab-1500, 2009). Figure 3.3 is an image of AutLab-1500 used in this study. Figure 3.4 presents a conceptual diagram of the test facility. One temperature transducer (TT1) is used to measure the temperature. Four pressure transducers (PT1, PT2, PT3, and PT4) are used to measure the upstream reservoir pressure, the confining pressure at the flank of the core, the downstream reservoir pressure, and the axial pressure at the ends of the core, respectively. AutLab-1500 conveniently runs most standard rock mechanics test regimens, such as hydrostatic compression, pure shear, unconfined compression, confined compression, creep, and uniaxial strain. Each of these tests can be performed at pore pressures and temperatures representative of reservoir conditions. The system can also measure rock permeability, and sonic velocity.

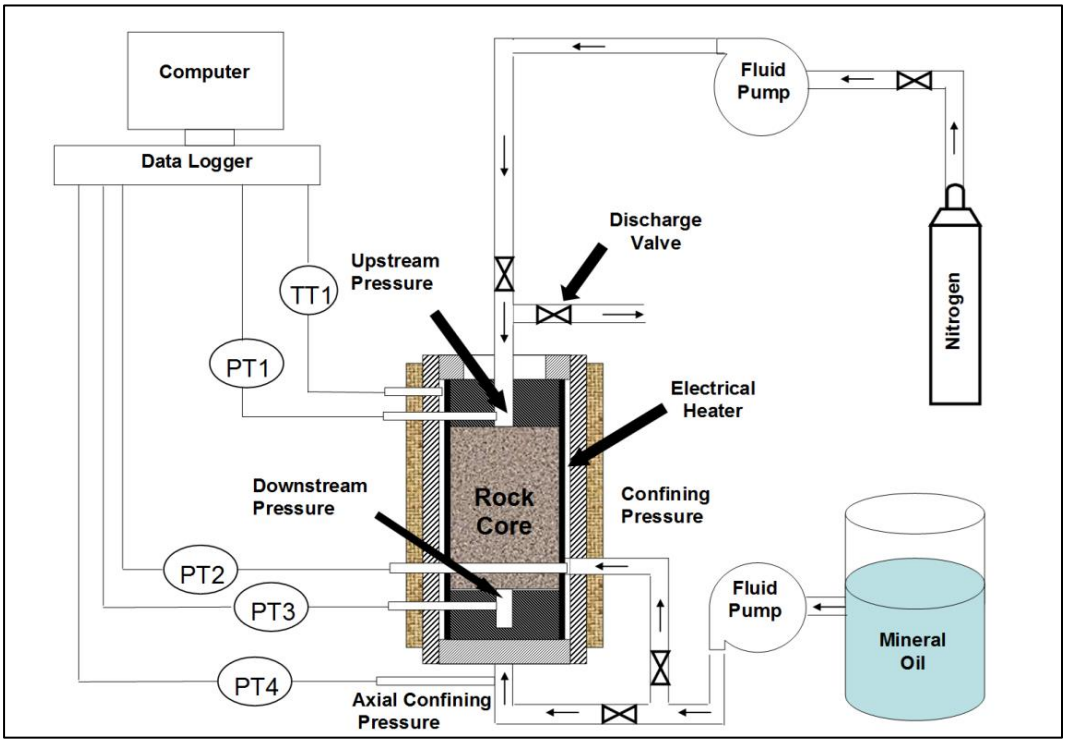

Figure 3.4 Schematic diagram for the experimental setup. The nitrogen vessel is the upstream extended reservoir and its pressure is measured by pressure transducer PT1; the pressure of the downstream reservoir (volume = 0.63cc) is measured by PT3; the mineral oil is used for confining pressure and axial pressure systems

3.3. Measurement of Petrophysical Properties

3.3.1. Porosity

Porosity is a measure of the void spaces in a rock, and is a fraction of the volume of voids over the total rock volume. There are two types of porosity: total or absolute porosity and effective porosity. Total porosity is the ratio of all the pore spaces in a rock to the bulk volume of the rock. Effective porosity is the ratio of interconnected void spaces to the bulk volume. Thus, only the effective porosity contains fluids that can be produced from wells.

For oil and gas reservoirs, porosity provides the space to store the fluid subsurface. Porosity measurements were conducted to evaluate the storage ability of Bakken Formation. In this study, the measured porosity is effective porosity.

Equipment

The porosity of core plug was measured by gas compression method which employs real gas law. Helium is used as the test fluid because it has small molecular size and inertial property, and it does not adsorb on the rock surface. The porosimeter apparatus is shown schematically in Figure 3.5. This system consists of gas source, three pressure gauges, and two chambers. The core is put in Chamber 2.

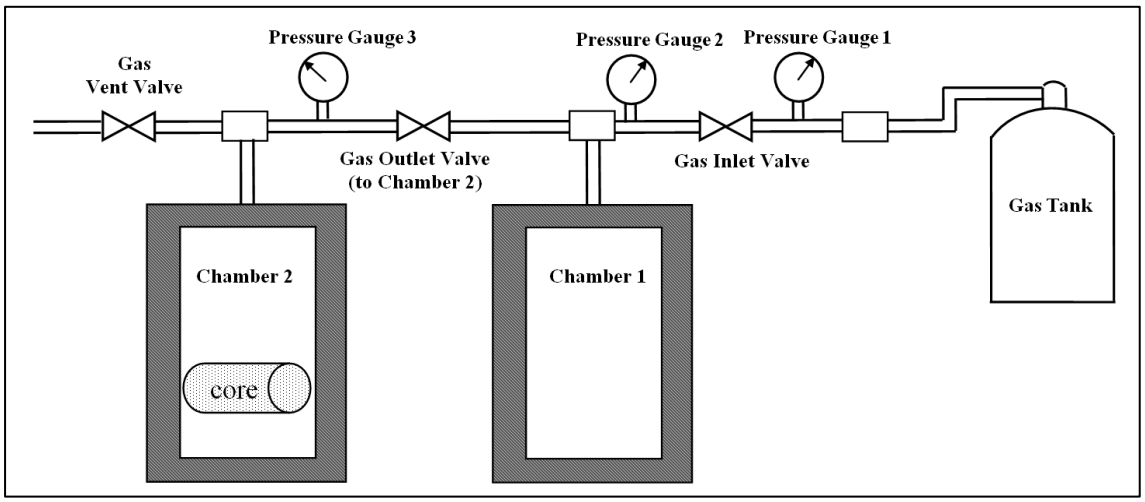

Figure 3.5 Schematic diagram of porosimeter apparatus

Measurement Principle

The measurement principle is based on real gas law. Followings are the derivation of governing equation to measure the core porosity.

Firstly, the sum of the volume of Chamber 1 and pipeline volume between Gas Inlet

Valve and Gas Outlet Valve is denoted as Volume 1, V_1.

$$V_1 = V_{\text{chamber 1}} + V_{\text{pipeline between Gas Inlet Valve and Gas Inlet Valve}} \tag{3.1}$$

Similarly, the sum of the volume of Chamber 2 (without core) and pipeline volume between Gas Outlet Valve and Gas Vent Valve is denoted as Volume 2, V_2.

$$V_2 = V_{\text{chamber 2}} + V_{\text{pipeline between Gas Outlet Valve and Gas Vent Valve}} \tag{3.2}$$

The bulk volume of core is denoted as $V_{bulk,\,core}$, which is calculated by

$$V_{bulk,core} = \frac{\pi}{4} D_{core}^2 L_{\text{core}} \tag{3.3}$$

Initially the pressure in Chamber 1 is p_1 and pressure in Chamber 2 is p_2, where $p_1 > p_2$. Then Gas Outlet Valve is open to allow gas flow from Chamber 1 to Chamber 2 and reach equilibrium. The equilibrium pressure, p_3, is recorded. According to real gas law we have

$$p_1 V_1 = z_1 n_1 R T_1 \tag{3.4}$$

$$p_2 \left[V_2 - V_{bulk,core} \left(1-\phi\right) \right] = z_2 n_2 R T_2 \tag{3.5}$$

$$p_3 \left\{ \left[V_2 - V_{bulk,core} \left(1-\phi\right) \right] + V_1 \right\} = z_3 \left(n_1 + n_2\right) R T_3 \tag{3.6}$$

The temperature is kept constant and pressure is changed in a narrow range. Therefore we have

$$z_1 \cong z_2 \cong z_3 \tag{3.7}$$

Equations (3.4), (3.5), and (3.6) can be simplified into

$$p_1 V_1 = z_1 n_1 R T_1 \tag{3.8}$$

$$p_2 \left[V_2 - V_{bulk,core} \left(1 - \phi \right) \right] = z_1 n_2 R T_1 \tag{3.9}$$

$$p_3 \left\{ \left[V_2 - V_{bulk,core} \left(1 - \phi \right) \right] + V_1 \right\} = z_1 \left(n_1 + n_2 \right) R T_1 \tag{3.10}$$

Summing Equations (3.8) and (3.9) we obtain

$$p_2 \left[V_2 - V_{bulk,core} \left(1 - \phi \right) \right] + p_1 V_1 = z_1 \left(n_1 + n_2 \right) R T_1 \tag{3.11}$$

Comparing the right-hand-sides of Equations (3.10) and (3.11) gives us

$$p_2 \left[V_2 - V_{bulk,core} \left(1 - \phi \right) \right] + p_1 V_1 = p_3 \left\{ \left[V_2 - V_{bulk,core} \left(1 - \phi \right) \right] + V_1 \right\} \tag{3.12}$$

Rearranging Equation (3.12) yields

$$\phi = 1 - \frac{V_2}{V_{bulk,core}} + \frac{\left(p_1 - p_3 \right) V_1}{\left(p_3 - p_2 \right) V_{bulk,core}} \tag{3.13}$$

Equation (3.13) is the governing equation to calculate the rock porosity. Three pressures (p_1, p_2, and p_3) are recorded in the measurement. Volume 1(V_1), and Volume 2 (V_2) can be determined using standard volume samples made of stainless steel (zero porosity). The approach is also based on real gas law. The bulk volume of core ($V_{bulk,core}$) is readily calculated from core diameter and height with Equation (3.3).

Measurement Procedure

The measurement of porosity of a specimen includes following steps:

1) Put the core into Chamber 2, close Gas Vent Valve, and open Gas Inlet Valve and Gas Outlet Valve to allow gas from gas tank fill Chambers 1 and 2 until pressure

reaches 100 psig.

2) Open Gas Vent Valve and allow gas from gas tank purge Chambers 1 and 2, Wait for 10 to 20 minutes until the purity of gas in Chambers 1 and 2 is high enough.
3) Close Gas Vent Valve, Gas Inlet Valve, and Gas Outlet Valve, record the pressure of Chamber 2, p_2.
4) Keep Gas Vent Valve and Gas Outlet Valve close, Open Gas Inlet Valve and allow gas from gas tank fill Chamber 1 until its pressure reaches target pressure, close Gas Inlet Valve and record the pressure of Chamber 1, p_1.
5) Open Gas Outlet Valve to allow gas flow from Chamber 1 to Chamber 2 (because $p_1 > p_2$), wait until pressure reaches equilibrium, or pressure at Pressure Gauge 3 equates pressure at Pressure Gauge 2, record equilibrium pressure, p_3.
6) Now we finish the porosity measurement of specimen. Porosity can be calculated by Equation (3.13).

3.3.2. Permeability

Permeability is a property of a porous medium and is an indicator of its ability to allow fluids flow through its inter-connected pores. Permeability is an inherent characteristic of the porous media only. It depends on the effective porosity of the porous media (Triad, 2004).

The fundamental SI unit of permeability is m^2, but the Darcy (D), named after French engineer Henry Darcy, is a practical unit for permeability. One Darcy is defined as

follows: a permeability of one Darcy will allow a flow of 1 cm^3/s of fluid of 1 centipoise (cp) viscosity through an area of 1 cm^2 under a pressure gradient of 1 atm/cm. One Darcy equals 0.986923×10^{-12} m^2. In the oil and gas industry, a smaller unit of permeability, milli-Darcy (mD), is used more commonly because the permeability for most rocks is less than one Darcy, and for the low permeability rocks, the use of micro-Darcy (μD) or nano-Darcy (nD) is common.

The range of the permeability of the petroleum reservoir rocks may be from 0.1 to 1,000 mD. One rock is considered to be tight when its permeability is below 1 mD (Triad, 2004). However, this criterion has been lowered to values of 0.1mD (Law & Spencer, 1993) due to the application of the new stimulation techniques to increase oil and gas production.

Tight rocks have been extensively studied for a wide range of applications that include CO_2 geological storage, deep geological disposal of high-level, long-lived nuclear wastes, and production of oil and gas from unconventional reservoirs. In the recent years, the increasing demands for oil and gas have stimulated the explorations and productions of petroleum from low permeability formations, such as Bakken shale. More realistic fluid flow simulation to model the process of producing the hydrocarbons in Bakken Formation requires more accurate measurements of permeability. Also it is urgent to investigate the low permeability of the Bakken Formation in order to gain better understanding of the process of well producing hydrocarbons from it.

Based on experimental work from Darcy (1856), many methods have been presented to improve the accuracy and efficiency of measurement. These methods, based on flow regime, can be classified into two categories: steady-state flow methods and unsteady-state flow methods. Steady-state flow methods measure permeability under steady-state conditions. Aside from low flow rates across the core plug being difficult to measure and control, these tests are quite time consuming. In this case, unsteady state flow is applied to estimate permeability. Brace et al. (1968) introduced a transient flow method to measure the permeability of Westerly granite. From this, many unsteady-state methods have been proposed to measure the permeability of tight rocks. Most of these methods fall into three categories: the pulse decay method, the Gas Research Institute (GRI) method, and the oscillating pulse method.

For the pulse-decay method, the sample has both an upstream reservoir and a downstream reservoir. A pressure pulse, which is applied at the upstream reservoir, will decay over time. The permeability is estimated by analyzing the decay characteristics of the pressure pulse (Brace et al., 1968). Dicker and Smits (1988) improved the pressure pulse-decay method by showing a general solution of the differential equation which describes the pressure decay curve. Based on this solution, they theoretically pointed out that fast and accurate measurements are possible when the volumes of the upstream and downstream reservoirs in the equipment are equal to the pore volume of the sample. Jones (1997) pointed out that the initial pressure equilibration step is the most

time-consuming part of the pulse-decay technique. To avoid the equilibrium state, Jones' method utilizes a smooth pressure gradient, which requires smaller upstream and downstream reservoirs. To account for adsorption during pulse-decay measurement, Cui et al. (2009) presented their method which can describe gas transport in low permeability reservoir more reliably and accurately. Metwally (2011) proposed another pulse-decay method by keeping the upstream reservoir pressure constant leading to an infinitely large volume of the upstream reservoir, so that the ratio of upstream reservoir volume to downstream reservoir volume is infinite. Thus, the solution of the pulse-decay measurements can be simplified.

The GRI method differs from the pulse-decay method in that the measurement is carried out on crushed rock samples; a pressure pulse is applies on unconfined crushed rock particles. Permeability is then obtained through the analysis of the pressure decay over time. Cui et al. (2009) developed a late-time method utilizing data from either pulse-decay or GRI experiment to determine the permeability. The GRI method has the advantage of a shorter experimental time as compared with other methods. Unfortunately, permeability measured from crushed samples can differ by 2 to 3 orders of magnitude among different commercial laboratories (Passey et al., 2010 and Tinni et al., 2012). Another limitation of this method is that the microcracks in the crushed particles essentially violate the GRI assumptions. This leads to an overestimate of permeability (Tinni et al., 2012). To improve the accuracy and consistency of the GRI method, Sinha

(2012) developed cylindrical calibration standards based on Darcy's law to calibrate the low permeability measurement apparatus. The GRI method is not used in this study because of large permeability differences between crushed and intact samples.

The oscillating pulse method estimates rock permeability by interpreting amplitude attenuation and phase retardation in the sinusoidal oscillation of the pore pressure as a pressure pulse propagates through a sample. At the beginning of the experiment, the sample pore pressure, the upstream reservoir pressure, and the downstream reservoir pressure are stabilized. Then a pressure wave is generated in the upstream reservoir and propagates through a core plug. The permeability can be obtained by using the information of the amplitude attenuation and phase shift between the upstream reservoir pressure wave and the derived downstream reservoir pressure wave at the downstream side of the sample. Although this method can measure the permeability in a relatively short time without destroying the sample, as the GRI method does, the accuracy of permeability obtained from this method relies on the signal-to-noise ratio and data analysis techniques (Kranz et al., 1990).

Normally, permeabilities measured by the different methods are not in good agreement. Bertoncello (2013) concluded that the steady-state method with critical fluid provides much more consistent and acceptable results after comparing permeability measurements performed at several commercial and research laboratories using four different techniques. However, Bertoncello (2013) did not mention the time of measurement for

each method. In fact, the measurement of tight rock permeability, such as in Bakken samples, is time consuming and expensive due to their low permeability. In addition, the results given by Lab_1 from transient methods are consistent and acceptable, and Lab_1 is the only laboratory which provides different methods.

We introduced a testing process to measure the permeability of tight rocks with three different methods under the same procedure. These methods are the oscillating pulse method, the downstream pressure build-up method, and the radius-of-investigation method. In this way, not only the comparability of the results from these three methods increased, but the difference among the results is also useful for indicating the heterogeneity and/or microcracks of the rock.

Method 1: Oscillating Pulse Measurement Method

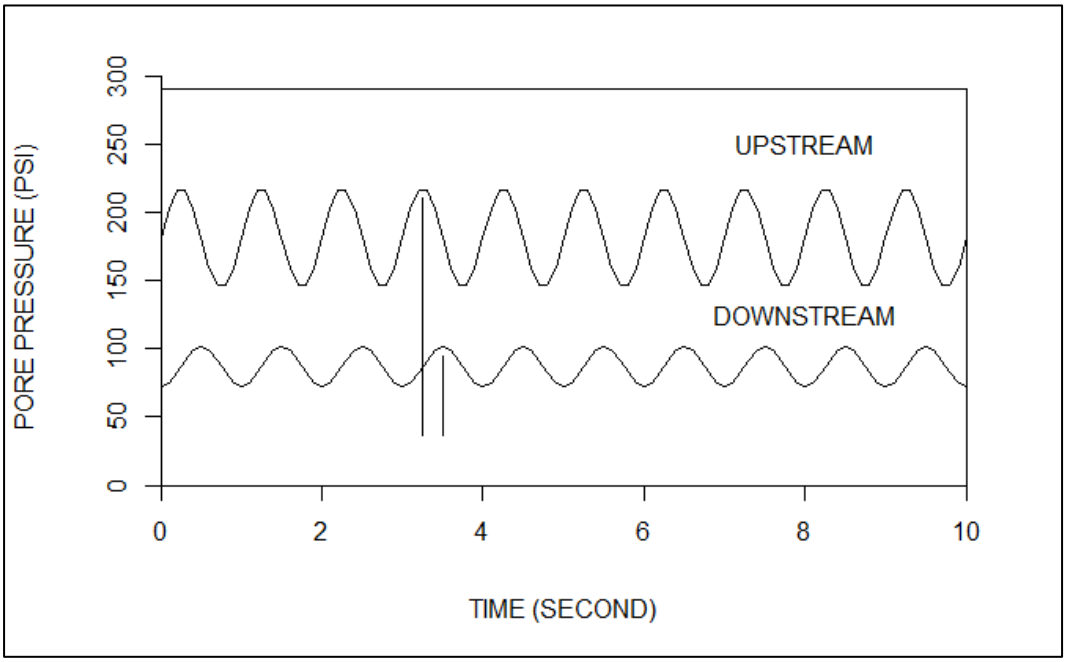

Figure 3.6 Illustration of the effect of the upstream input oscillation frequency on the resultant downstream amplitude and phase shift of the oscillating pulse method

Figure 3.6 indicates the theory of the aforementioned oscillating pulse method (Kranz et al., 1990). A pressure oscillation with fixed-amplitude and fixed-frequency in the upstream reservoir results in a reduced amplitude and phase-shifted pressure oscillation in the downstream reservoir after diffusing through the core sample. The amplitude ratio and phase shift provide information about the hydraulic properties of the rock. Based on these pressure responses, an analytical solution for permeability can be calculated from either the amplitude ratio or the phase shift. The relationship between the upstream and downstream perturbations is a function of the length, cross-sectional area, permeability, specific storage of the sample, the viscosity of the fluid, and the compressibility of the fluid. Appendix A provides the derivation of equations for this method given by Kranz et al. (1990). However, a strong dependence on the ratio of permeability to specific-storage creates a situation where an error in the determination of one parameter (i.e. specific storage) will lead to an error in the determination of the other (i.e. permeability).

Derivation of Diffusivity Equation

The estimations of permeability by the downstream pressure build-up method and the radius-of-investigation method require the solution of the diffusivity equation for the Darcy flow through the core sample. To derive the diffusivity equation, the following assumptions are made: 1) the core is homogeneous, 2) the properties of the rock are constant, 3) the flow in the cylindrical core is laminar, and 4) the flow in the core is isothermal. Because the permeability of tight rock is low, nitrogen gas is used as the test

fluid in our experiment. The gas flows from the left-side of the core, through the core, and out of the right-side of the core as shown in Figure 3.7.

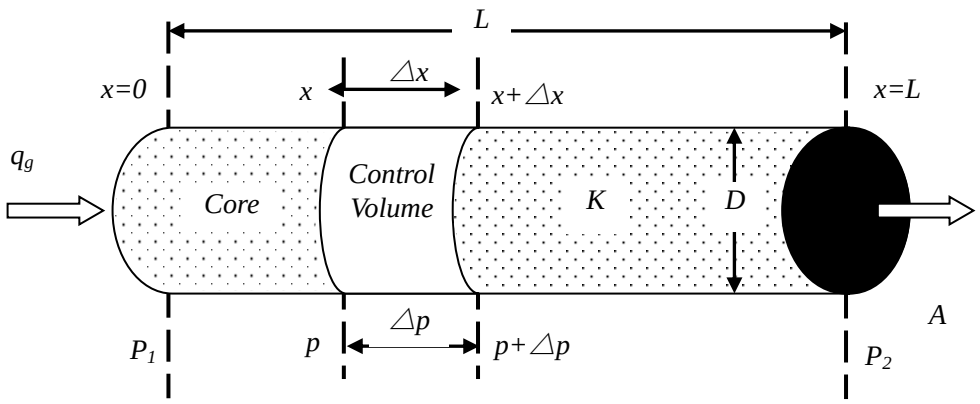

Figure 3.7 Schematic diagram depicting how gas flows through a core

Considering a control volume (from x to $x+\Delta x$), which is the volume that the gas flows in from x and out at $x+\Delta x$ during a certain time period Δt, and combining the mass conservation, Darcy's law, real gas law, and the gas pseudo-pressure concept (Al-Hussainy, 1966), a diffusivity equation for linear gas flow is stated as:

$$\frac{\partial^2}{\partial x^2}[m(p)] = \frac{\phi \mu c_t}{k}\frac{\partial}{\partial t}[m(p)] \tag{3.14}$$

where $m(p)$ is the gas pseudo-pressure, which is expressed as

$$m(p) = \int_{p_b}^{p} \frac{2p}{\mu z} dp \tag{3.15}$$

Method 2: Downstream Pressure Build-up Measurement Method

In the downstream pressure build-up method, the upstream reservoir pressure is kept constant throughout the entire test and the pressure build-up is observed in the

downstream reservoir when the gas flows through the core plug into it.

To calculate the permeability from the build-up curve of the measured downstream reservoir pressure, the solution to the diffusivity Equation (3.14) needs to be known. Permeability is then estimated through Equation (B.14). The derivation of equations for this method is in Appendix B.

Method 3: Radius-of-Investigation Measurement Method

Based on the Radius-of-Investigation Concept (Lee, 1982), a new method was proposed to measure core permeability. When doing the permeability test using the downstream pressure build-up method, it was observed that the downstream reservoir pressure did not increase immediately when the upstream reservoir was connected with the core plug. The lower the permeability, the longer the delay time was observed. The time that a pressure disturbance propagates through a core sample is a function of the permeability of the rock. Therefore, the low to extremely low permeability of Bakken samples can be calculated by measuring the delaying time, which is the time that the pressure disturbance propagates from the upstream end of the core plug to the downstream end of the core plug.

The pressure disturbance concept is applied here to estimate the propagation of pressure in the core plug. First, a pressure disturbance was introduced by increasing the upstream reservoir pressure or decreasing the downstream reservoir pressure instantaneously; then the time (t_m) at which the disturbance at location x reaches its

maximum was determined. With measured t_m and given core geometry, the permeability can be obtained using Equation (C.7). The derivation of equations for this method is in Appendix C.

Measurement Procedure

First, the cylindrical Bakken core plug was covered with copper sheeting in order to both form a gas-tight seal on the cylindrical wall of the sample and to apply radial confining pressure. Then the core plug was mounted in a sample holder with flexible rubber sleeves at both ends of the plug (Figure 3.7). Finally, the sample holder was put into a vessel flooded with mineral oil, in which the sample could be hydrostatically compressed by hydraulically applying force to the plug. To minimize the volume of the downstream reservoir, a small pocket was implemented inside the downstream end-cap (Figures 3.8). The volume of downstream reservoir was 0.63 cc.

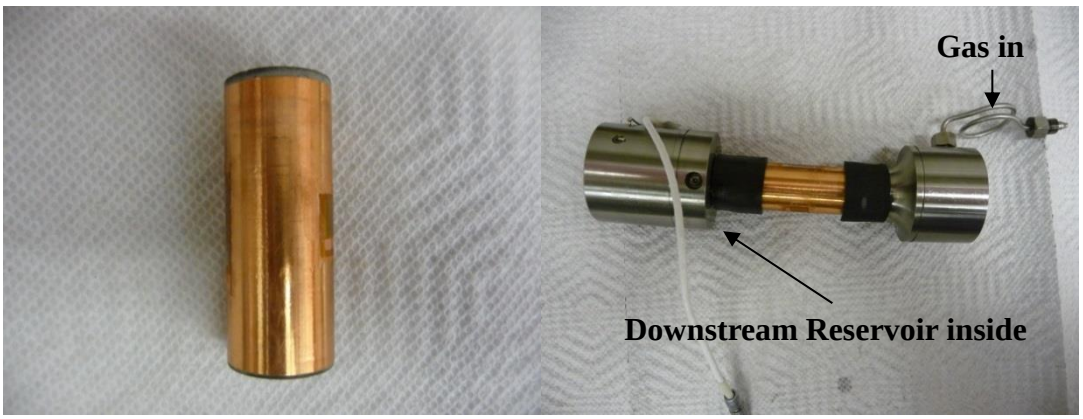

Figure 3.8 Core covered with copper sheeting, and assembled on End Caps for a low permeability test system

The equipment used to perform the experiments is AutLab-1500. The determination of

the permeability is a three-step process for all of these three methods, namely installing the core plug into the AutLab-1500, running the test, and analyzing the resultant data.

1) Installing the core plug into the AutLab-1500

First, the sample is placed into the vessel; then the vessel is filled with mineral oil and the confining pressure is increased to the desired level (p_c). The valve between the core plug and the upstream reservoir is closed. Dry nitrogen is used to fill the upstream reservoir, and the upstream reservoir pressure is increased to the desired level (p_1). The downstream reservoir is at atmospheric pressure. Notice that the confining pressure must be greater than the upstream reservoir pressure.

2) Running the test

The start time is recorded when the valve between the core plug and the upstream reservoir is opened. During the entire test, the upstream reservoir and confining pressures are constant. The pressures are monitored and recorded at both the upstream and downstream ends of the sample.

Figure 3.9 shows the change of downstream reservoir pressure during the test. A constant pressure is applied at the upstream end of the core plug, and the pressure at the downstream end of the core plug is built up. For the radius-of-investigation method, the test ends when the downstream reservoir pressure starts to increase, which is at point “B”. For the downstream pressure build-up method, the test ends when the downstream reservoir pressure is equal to the upstream reservoir pressure, which is at point “A”. For

the oscillating pulse method, the test ends at the point “C”.

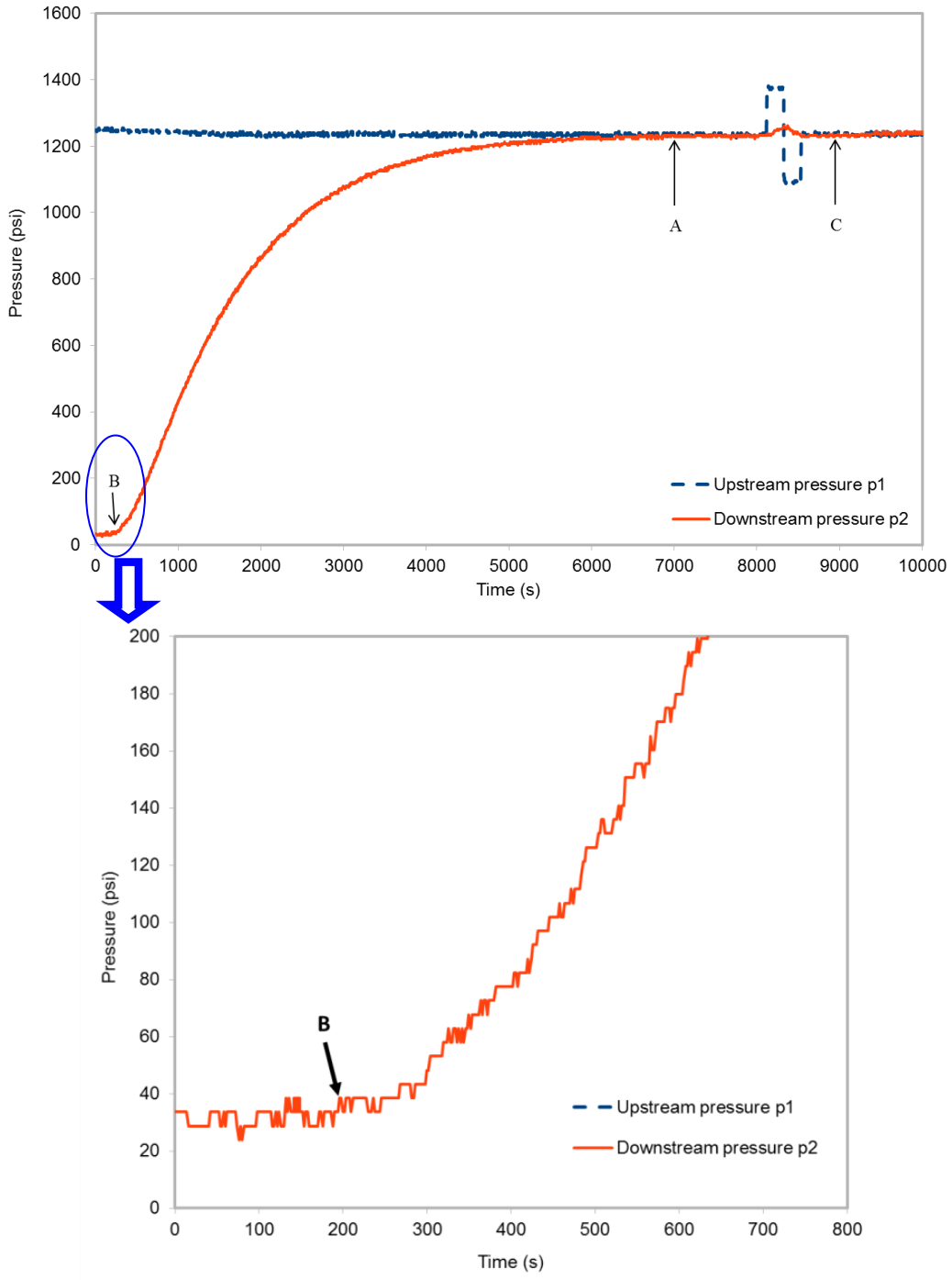

Figure 3.9 Changes of the upstream and downstream pressure during one experiment for Core #1.
Point “A” marks the time at which the downstream pressure build-up method stop, point “B” marks the time at which the radius-of-the investigation method stop, and point “C” marks the time at which the oscillating pulse method stop

3) Analyzing the resultant data

For the radius-of-investigation method, after finding the time of point "B", the permeability can be obtained using Equation (C.7) or (C.8). To better determine point "B", the section from constant downstream pressure to downstream pressure build-up is amplified.

The beginning point of the increasing in downstream pressure is selected as point "B", and the section "BA" shows the pressure change in the downstream reservoir as a function of time (Figure 3.9). To obtain the permeability using the downstream pressure build-up method, first the pressure difference is calculated using a logarithm scale form equation $\ln[\Delta p(t)] = \ln[p_1^2(0) - p_2^2(t)]$; then from the plot (Figure B.1), we obtain the slope s; finally, Equation (B.16) is used to obtain the permeability of the rock (see Appendix B).

For the oscillating pulse method, the AutLab-1500 system directly gives the permeability.

3.4. Measurement of Geomechanical Properties

3.4.1. Elastic Moduli

Rocks will behave a linear elastic material approximately if the stresses they are subjected to are considerably lower than their ultimate strengths. The basic elastic constants, such as Young's modulus, Poisson's ratio, shear modulus, bulk modulus, and Lame constant, are based on this linear elasticity theory, For homogeneous isotropic

linear materials, given any two elastic moduli, any other elastic moduli can be calculated with conversion formulas (Zhou, 2011). In our study, we measured two independent elastic constants, Young's modulus and Poisson's ratio; the other elasticity parameters can be derived from these two parameters.

Static Young's Modulus and Poisson's Ratio

Young's modulus, also known as the tensile modulus or elastic modulus, is a measure of the stiffness of an elastic material and is a quantity used to characterize materials. It is defined as the ratio of the stress along an axis to the strain along that axis in the range of stress in which Hooke's law holds. When Young's modulus is calculated from deformational experiment directly by dividing the tensile stress by the tensile strain in the elastic (linear) portion of the stress-strain curve (Figure 3.10), it is called static Young's modulus.

$$E_{static} = \frac{\Delta\sigma}{\Delta\varepsilon} \tag{3.16}$$

where E_{static} is the static Young's modulus, σ is the axial stress exerted on specimen, and ε is the strain of specimen in axial direction.

Poisson's ratio, ν, named after Siméon Poisson, is the negative ratio of transverse to axial strain. When a material is compressed in one direction, it usually tends to expand in the other two directions perpendicular to the direction of compression (Figure 3.11). This phenomenon is called the Poisson effect. The Poisson ratio is the ratio of the fraction of

expansion divided by the fraction of compression, for small values of these changes.

$$\nu_{static} = \frac{\varepsilon_r}{\varepsilon_a} \tag{3.17}$$

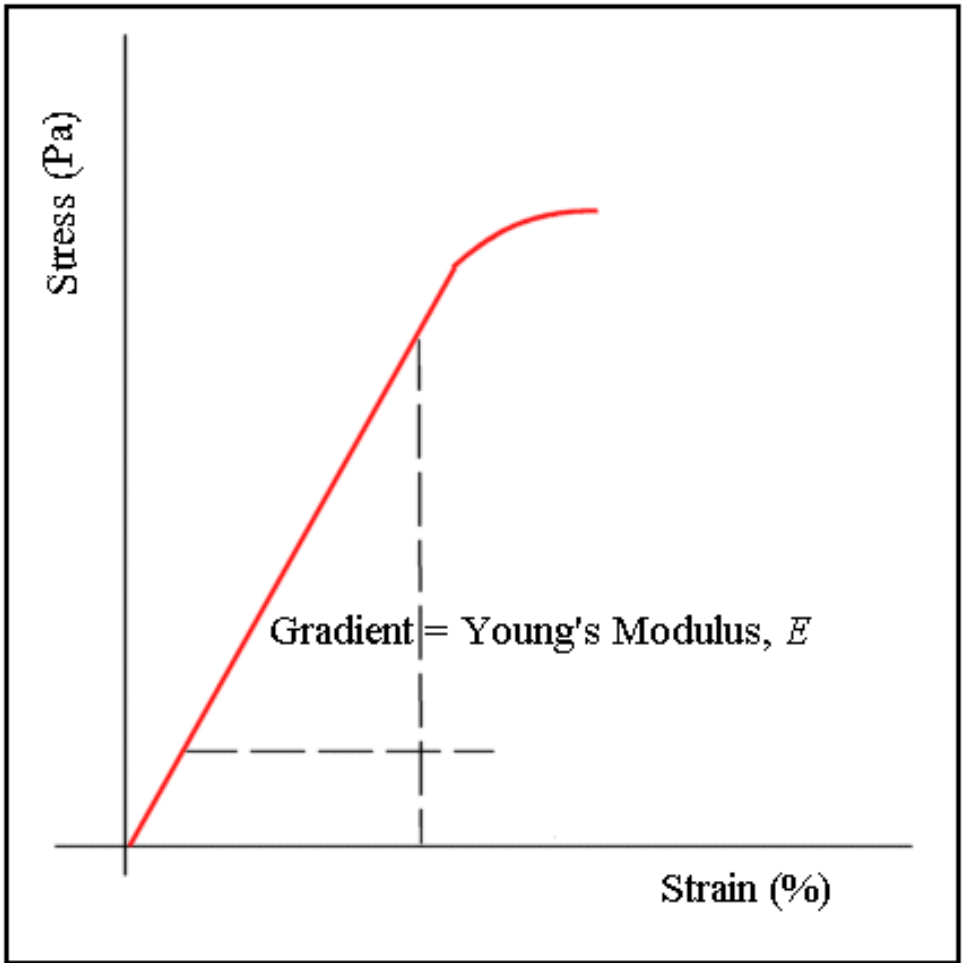

Figure 3.10 Static Young's modulus calculated from stress-stain relation

Based on the definition of strain (Jaeger, 2007), we have:

$$\varepsilon_r = \frac{\Delta r}{r} \tag{3.18}$$

$$\varepsilon_a = \frac{\Delta L}{L} \tag{3.19}$$

ε_r is the strain of specimen in radial direction, and ε_a is the strain of specimen in axial direction.

If the material is stretched, it usually tends to contract in the directions transverse to the direction of stretching. The Poisson's ratio will be the ratio of relative contraction to relative stretching, and will have the same value as above. Due to the requirement that Young's modulus, the shear modulus and bulk modulus have positive values, Poisson's ratio can vary from initially 0 to about 0.5. Generally, "stiffer" materials will have lower Poisson's ratios than "softer" materials. If Poisson's ratios are larger than 0.5, it implies that the material was stressed to cracking, or caused by experimental error, etc.

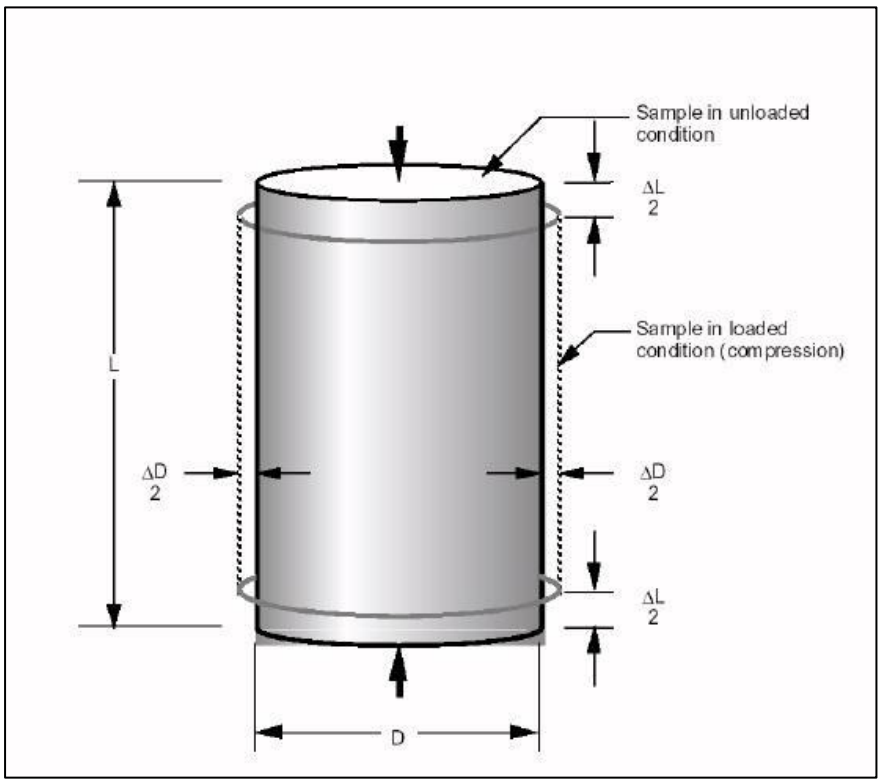

Figure 3.11 Poisson's ratio from a deformed cylinder-shape specimen (Poisson's Ratio, 2007)

Dynamic Young's Modulus and Poisson's Ratio

By definition, dynamic moduli and Poisson's ratio are those calculated from the elastic wave velocity and density. They are different from static dynamic moduli and Poisson's ratio moduli, which are directly measured in a deformational experiment. In this study, dynamic Young's modulus and Poisson's ratio are calculated from the primary wave (P-wave) and the secondary wave (S-wave) velocities and density.

$$E_{dynamic} = \rho v_s{}^2 \frac{3v_p{}^2 - 4v_s{}^2}{v_p{}^2 - v_s{}^2} \tag{3.20}$$

$$\upsilon_{dynamic} = \frac{v_p^2 - 2v_s^2}{2\left(v_p^2 - v_s^2\right)} \tag{3.21}$$

where $E_{dynamic}$ is the dynamic Young's modulus, $\nu_{dynamic}$ is the dynamic Poisson's ratio, ρ is the density of rock sample, v_p is P-wave velocity, and v_s is S-wave velocity.

Sonic velocity, or seismic velocity, is a measure of a formation's capacity to transmit seismic waves. It varies with lithology and rock textures, most notably decreasing with an increasing effective porosity. This means that a sonic log can be used to calculate the porosity of a formation if the seismic velocity of the rock matrix and pore fluid are known, which is very useful for hydrocarbon exploration. The velocity is calculated by measuring the travel time from the transmitter to the receiver. There are many types of seismic waves. Two types of wave, P-wave and S-wave are used to test the sonic velocity in rock in this study. P-wave is compressional wave that is longitudinal in nature. P-wave is pressure wave that travel faster than S-wave through the rock. S-wave is shear

wave that is transverse in nature. P-wave can travel through any materials. S-wave can travel only through solids, as fluids (liquids and gases) do not support shear stresses. S-wave is slower than P- wave.

Measurement Procedure

AutLab-1500 is used to perform our experiments. Static dynamic moduli and Poisson's ratio moduli are directly measured in a deformational experiment. The strains in the axial and radial directions of core plug are monitored by strain gages (Figure 3.12). The compressional stresses in the axial and radial directions are also recorded. Figure 3.13 shows an example of stress and strain in a non-destructive strength test in this study.

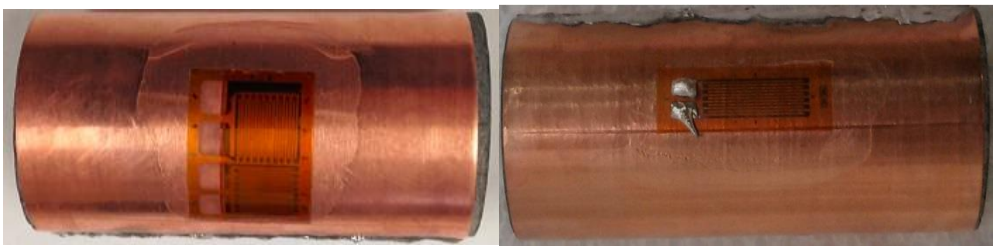

Figure 3.12 Image of sample with strain gages

Dynamic Young's modulus and Poisson's ratio are calculated from the results of sonic velocity test in the AutLab-1500, in which the ultrasonic signal is excited and captured by a pulser-receiver. Once the experiment has been completed, the data is edited and plotted.

The first step is to display the waveforms and pick the times of first arrival for each wave type: compressional or polarized shear wave. After the times of first arrival of P-wave (Figure 3.14), first S-wave (Figure 3.15), and second S-wave (Figure 3.16) are selected,

the velocities of P-wave and S-wave are calculated with the length of sample and the time. An example of the compression and shear wave velocities of core plug are shown in Figure 3.17.

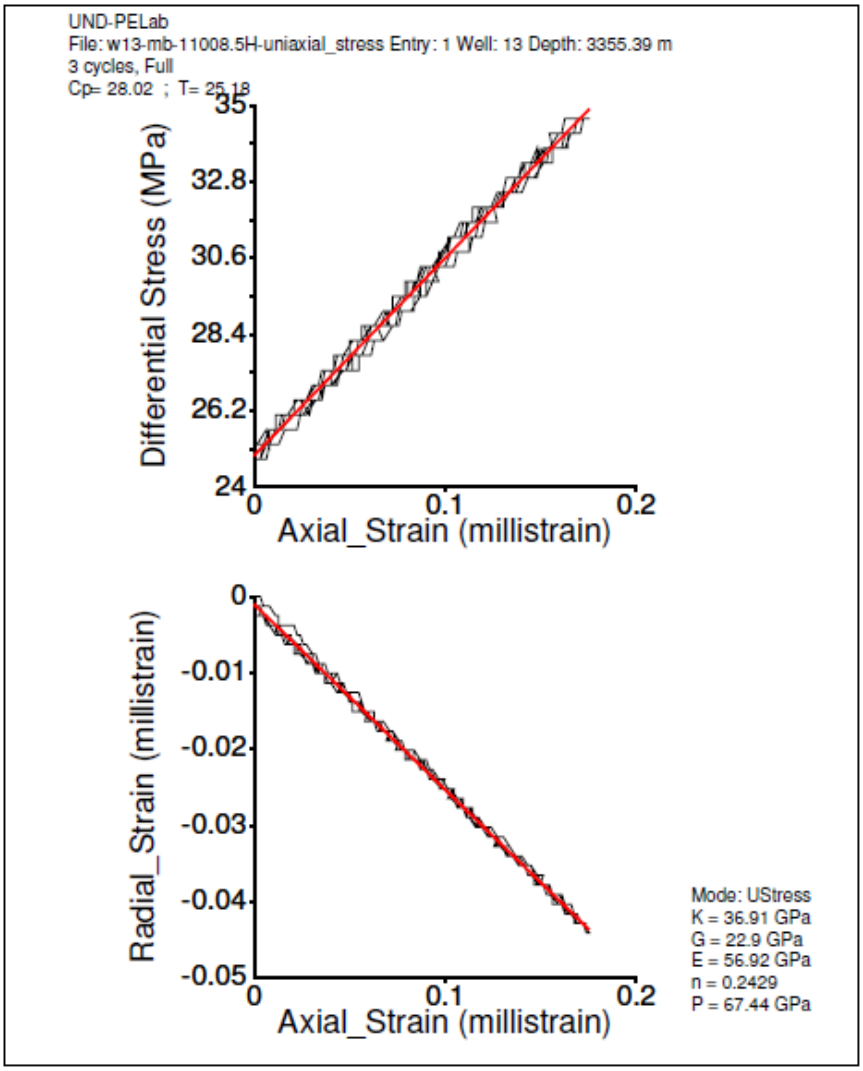

Figure 3.13 An example of stress and strain in a triaxial test

(K: Bulk modulus, G: Shear modulus, E: Young's modulus, n: Poisson's ratio, P: Constrained modulus.)

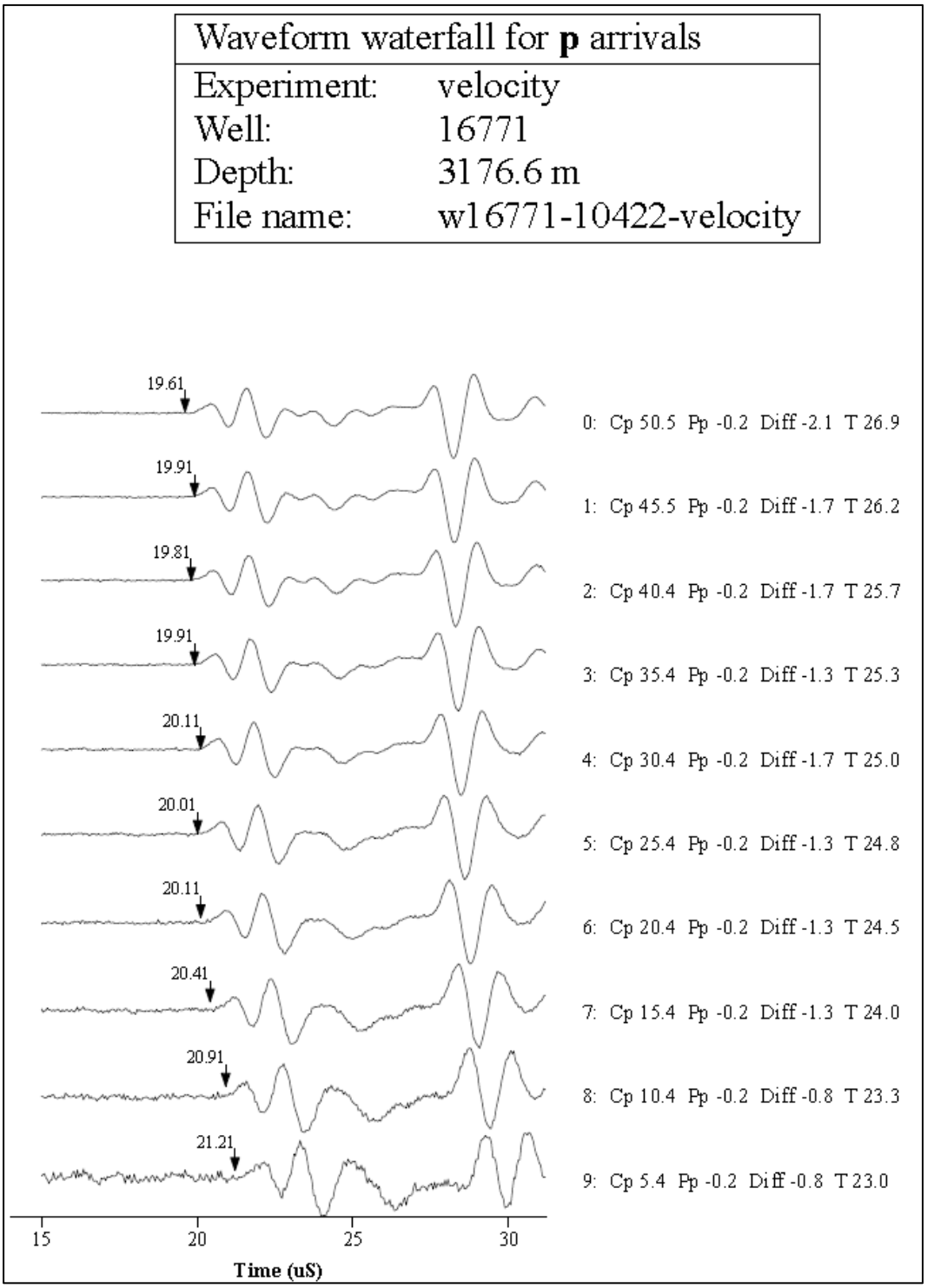

Figure 3.14 Waveform for P arrivals

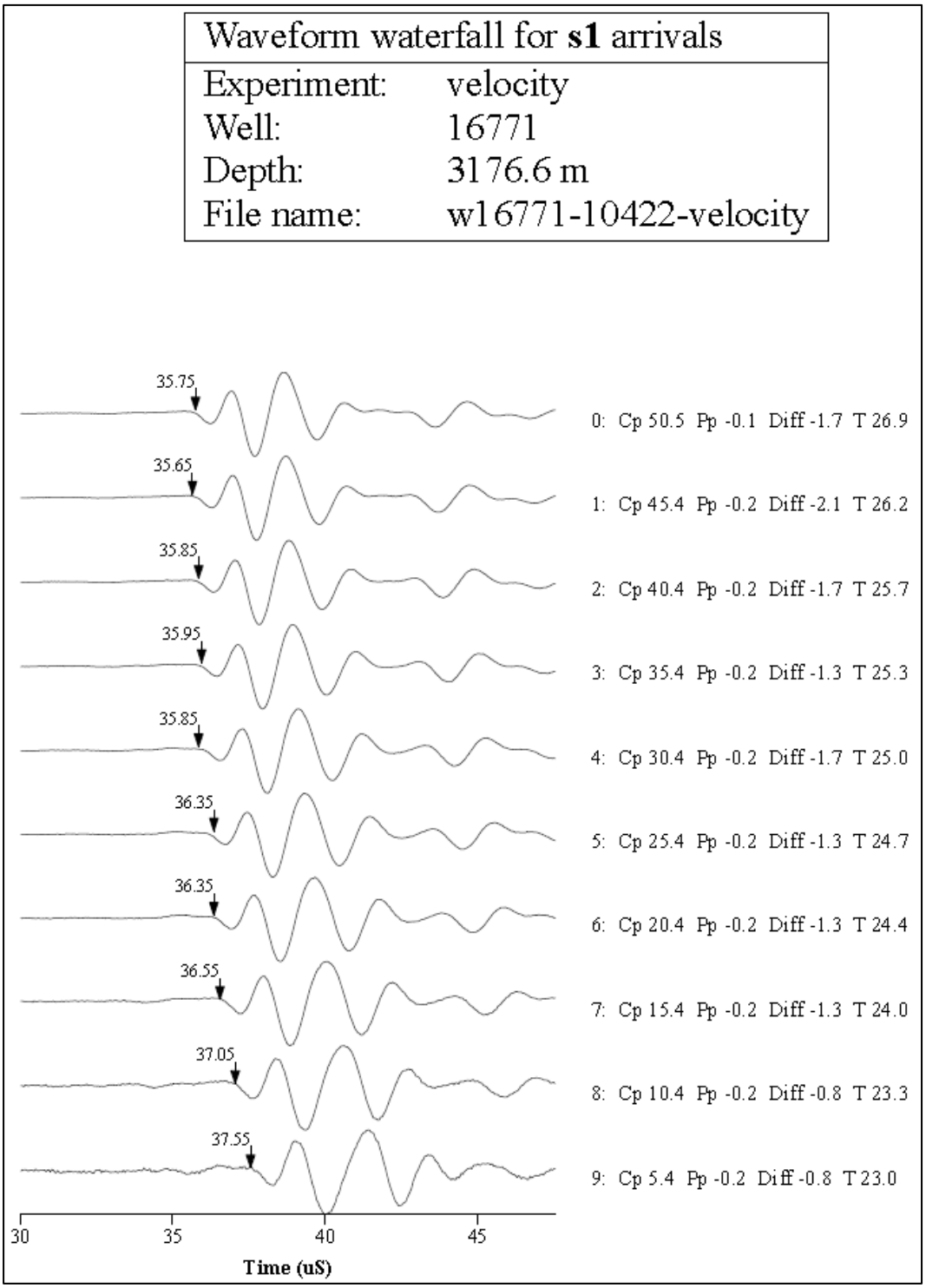

Figure 3.15 Waveform for S1 arrivals

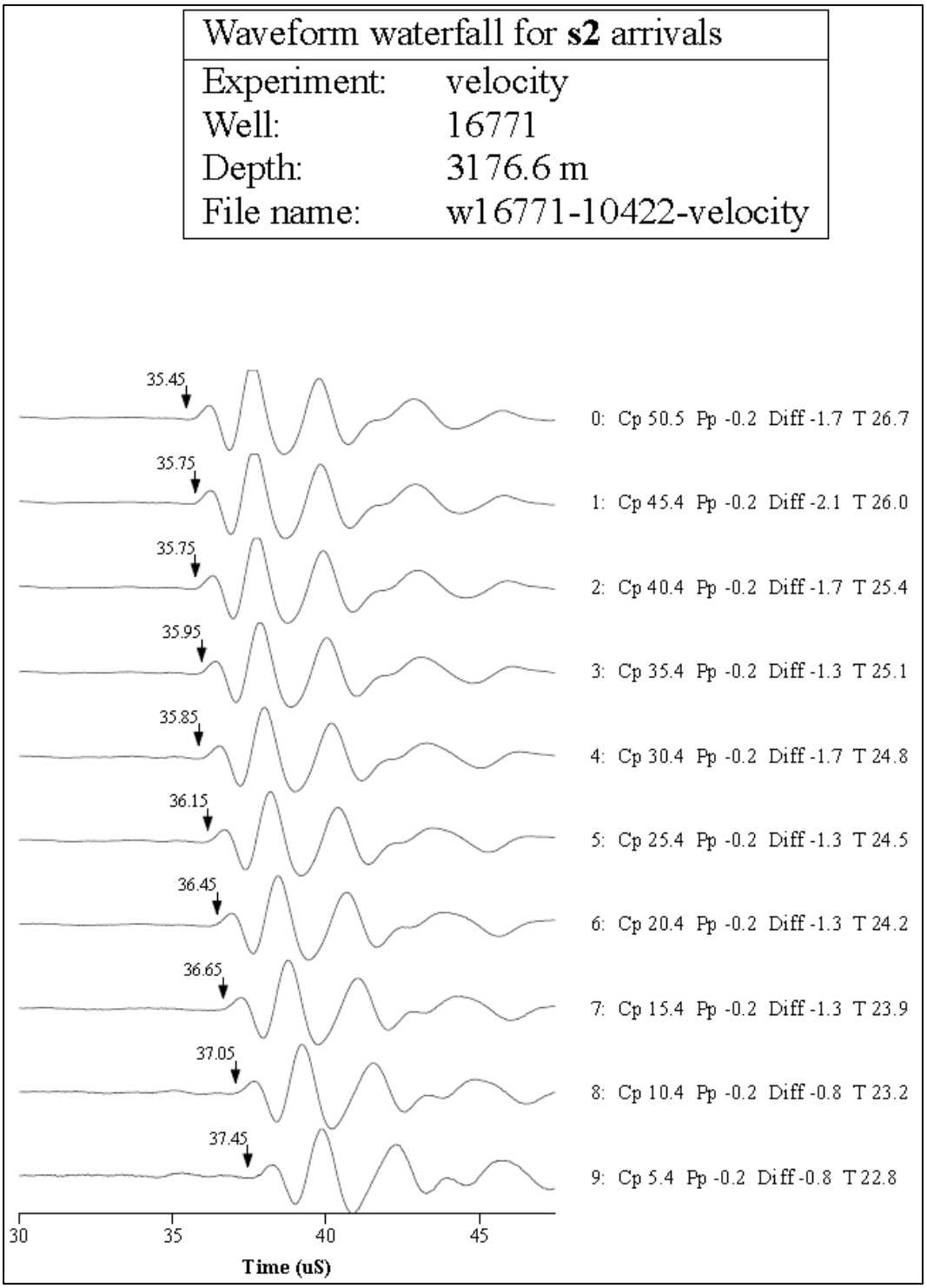

Figure 3.16 Waveform for S2 arrivals

Sample and Experiment Information for File w16771-10426.8-velocity			
Well:	16771	Organization:	UND
Depth:	3178.1 m	Transducer:	Vel_1in_new
Formation:	lower bakken	Rock type:	
Dry bulk density:	2.590 gm/cm^3	Porosity:	6.6%
Sat. bulk density:		Pore fluids:	Nitrogen
Diameter:	26.39 mm	Entered Length:	62.69 mm

Comments:	Geomechanics by Jun He
Expt name:	velocity
Expt date:	Tue Feb 19 13:13:46 2013
Print date:	Sun Apr 28 16:01:59 2013
A2D File:	

Observed Velocities and Moduli for File w16771-10426.8-velocity									
Event	Conf	Pore	Diff	Temp	V_p	$V_s^{(1)}$	$V_s^{(2)}$	Young's Modulus	Poisson's Ratio
	MPa	MPa	MPa	°C	m/s	m/s	m/s	GPa	
0	50.5	-0.2	-2.1	26.0	5189	3095	2965	59.03	0.241
1	45.4	-0.2	-2.1	25.4	5146	3095	2951	58.53	0.237
2	40.5	-0.1	-1.7	24.9	5276	3095	2979	59.83	0.252
3	35.4	-0.2	-1.7	24.6	5189	3080	2951	58.65	0.245
4	30.4	-0.2	-1.7	24.4	5232	3065	2910	58.17	0.258
5	25.4	-0.2	-1.6	24.2	5104	3080	2937	57.85	0.234
6	20.4	-0.2	-1.3	23.9	5104	3065	2910	57.30	0.239
7	15.5	-0.2	-0.7	22.5	5189	3050	2910	57.68	0.254
8	10.4	-0.2	-0.8	22.0	5232	3065	2883	57.79	0.261
9	5.4	-0.2	-0.4	21.4	5104	3065	2870	56.78	0.245

Figure 3.17 Dynamic properties calculated from sonic velocity

Because we want to compare the Young's modulus and Poisson's ratio from both tests, the measurement procedure is design as below.

First cover the sample with a copper foil and attach strain gages on the wall of the sample to monitor the deformation of the sample during the experiment. Then insert the sample between the velocity transducer assemblies, which are pulse-receiver embedded in the

two end-caps at both ends of the sample, to measure the velocities of P- and S-waves. Figure 3.18 shows a core holder with an instrumented Bakken sample that is jacketed and positioned between velocity transducer assemblies with strain-gauges attached. Finally, install the core holder into the pressure vessel of the AutoLab-1500.

Figure 3.18 Core holder with an instrumented Bakken sample that is jacketed and positioned between velocity transducers with strain gages attached

For appropriate comparison, the static and dynamic moduli were determined within the same situation. The tri-axial compression test was done with four loading cycles. The Young's modulus was obtained from the cycles except the first cycle to eliminate the effect of the first loading (Bruno, 1991). The test deformation rate is constant (0.01 mm per minute), the confining pressure is 30MPa, and the axial stress in the loading is nominally between 20 and 30 MPa, below failure criteria. The axial and radial strains of each sample were measured with strain gauges. From Equations (3.16) and (3.17), the static Young’s modulus and Poisson’s ratio are obtained respectively as shown in Figure

3.13.

After the four loading cycles of tri-axial compression test, the velocity test was started to get the dynamic moduli at the same situation as tri-axial compression test. When P- and S-waves propagated through the sample, the signals of P- and S-waves were recorded with the pulse-receiver, and the travel times for each wave type were read from their first arrivals. Thus the velocities for P- and S-waves were obtained by dividing the sample length by the travel time. With Equations (3.20) and (3.21) we got the dynamic Young's modulus and Poisson's ratio as shown in Figure 3.17.

The procedure for conducting the experiment is listed as follow:

1) Jacket the sample with copper foil.
2) Attach strain gages to the sample.
3) Secure the sample to the ultrasonic velocity transducer assembly.
4) Insert the transducer assembly with the jacketed sample into the pressure vessel.
5) Fill the pressure vessel with mineral oil.
6) Increase the confining pressure to reservoir level.
7) Increase the differential stress and the confining pressure to the initial value for the tri-axial compression measurement.
8) Set the loading rate, the range of the axial stress, and the number of loading cycles for the tri-axial compression test.
9) Start tri-axial compression test, and collect the data.

10) End tri-axial compression test.

11) Select P and S waves as the wave types for velocity test.

12) Start velocity test, and store the test data.

13) End velocity test.

14) Calculate static moduli with the data from tri-axial compression test.

15) Calculate dynamic moduli with the data from velocity test, after obtaining the travel time for P- and S-waves.

3.4.2. Compressibility

Rock compressibility is a measure of the relative volume change of a rock as a response to a pressure change. It is also called pore compressibility and is expressed in units of pore volume change per unit pore volume under per unit pressure change (Petrowiki). Rock compressibility is one of key parameters in designing oil and gas well drilling and completion, modeling fluids flow in reservoir, and forecasting well production.

There are two methods to obtain rock compressibility. One is direct measurement; another is indirect measurement. Direct measurement measures compressibility through uniaxial or triaxial stress experiment. Indirect measurement estimates compressibility from correlations or other measurements. The importance of rock compressibility is reflected by numerous investigations attempting to evaluate it accurately.

Carpenter and Spencer (1940) measured compressibility of consolidated oil-bearing sandstones collected from East Texas oil field at reservoir conditions. Hall (1953)

conducted tests to measure limestone and sandstone compressibility in the same manner as those reported in the Carpenter and Spencer's study. He developed correlation to estimate rock compressibility through porosity. Hall found that ignoring rock compressibility can lead to 30 to 40 percent overestimation of oil in place. Fatt (1958a) studied the variation of rock compressibility at different pressures. Fatt (1958b) found that rock compressibility is a function of pressure and cannot be correlated to porosity. Van der Knaap (1959) proved the nonlinear stress-volume relations of elastic porous media through theoretical and experimental analysis. Harville and Hawkins (1969) indicated that rock compressibility of geopressured gas reservoir is higher than that of normally pressured reservoir. Newman (1973) measured compressibility of 256 samples taken from consolidated and unconsolidated rocks and compared with Hall's and van der Knaap's studies. Greenwald and Somerton (1981a) measured compressibility of Berea, Bandera, and Boise sandstones. Comparison of these compressibilities to those available in the literature indicated qualitative agreement for each of the sandstone types and for their relative behavior. Greenwald and Somerton (1981b) developed a semi-empirical model to calculated rock compressibility. Variables required for their model are initial porosity, clay content, a pore shape factor, a length and aspect ratio of representative cracks in the matrix grains, the volumetric density of these cracks, and the mineralogical composition of the sample along with the elastic moduli of the minerals present. Zimmerman et al. (1986) developed relations to evaluate rock compressibility from confining and pore pressures. They verified relations through experimental

measurements on Berea, Bandera, and Boise sandstones. Poston and Chen (1987) determined formation compressibility and gas in place in abnormally pressured reservoirs simultaneously using material balance. Chalaturnyk and Scott (1992) summarized different geomechanical test procedures and analyzed the results. Khatchikian (1996) proposed a method using the Gassman equation and reservoir parameters evaluated through log analysis. Yildiz (1998) predicted rock compressibility using production data. His method is the same as Poston and Chen's method. Macini and Mesini (1998) measured sandstone and carbonate compressibility by both static (deformation tests) and dynamics (acoustic tests) investigations. Their study showed that compressibility is not constant, but is a function of reservoir pressure. Marchina et al. (2004) measured compressibility of reservoir rocks of a heavy oil field under in-situ conditions. Li et al. (2004) presented a model to calculate rock compressibility using the elastic modulus and the Poisson's ratio. Suman (2009) estimated rock compressibility under reservoir conditions at different depleted stages using sonic velocity derived from 4D seismic.

Because direct measurement of rock compressibility is time consuming and cost expensive. Estimation of rock compressibility from other readily available experimental data, such as sonic velocity and permeability experiment, is highly demanded.

We developed two methods to determine the rock compressibility using permeability experimental data. The combination of the proposed method with direct measurement can be employed to ensure the reliability of the direct measurement and to quantify the

uncertainty resulting from lab and human errors, irregular core plug, and/or non-uniform deformation.

At permeability test part, we proved that permeability is calculated with Equation (B.16) and Equation (C.8) for Downstream Pressure Build-up method and Radius-of-Investigation method, respectively. Because the total compressibility (C_t) is the sum of the rock compressibility (C_f) and the gas isothermal compressibility (C_g), Equation (B.16) and Equation (C.7) become:

$$k = \frac{2\phi\mu c_t L^2 s}{3 - 3\sqrt{1 + \frac{\phi\pi D^2 L}{3V_2}}} \tag{3.22}$$

$$k = \frac{\phi\mu(c_f + c_g)x^2}{t_m} \tag{3.23}$$

and we have:

$$C_f = \frac{3k\left(1 - \sqrt{1 + \frac{\varphi\pi D^2 L}{3V_2}}\right)}{2\varphi\mu L^2 s} - C_g \tag{3.24}$$

$$C_f = \frac{2tk}{\phi\mu x^2} - C_g \tag{3.25}$$

Rock compressibility can be estimated from Downstream Pressure Build-up method with Equation (3.24) given porosity, permeability, gas viscosity and compressibility, the sample size, and the volume of downstream reservoir. When we take the core length as the pressure disturbance propagating distance ($x=L$), rock compressibility can also be

estimated from Radius-of-Investigation method with Equation (3.25) given porosity, permeability, gas viscosity and compressibility, and the time for pressure disturbance travel through the core. The aforementioned derivation of Equation (3.24) or (3.25) uses gas as test fluid to measure low permeability rocks.

It should be noted that liquid will be used for high permeability rocks. Similarly, liquid properties can be combined with porosity and permeability, and pressure disturbance travel time to calculate rock compressibility. Porosity and core length can be measured readily. Gas viscosity and compressibility can be calculated given gas composition, pressure, and temperature. Time of pressure disturbance travel through core can be obtained by recording the time when pressure disturbance is generated and the time it travels to downstream of the core. Permeability can be obtained by steady-state or unsteady-state test such as oscillating pulse and pulse decay methods.

3.4.3. Biot's Coefficient

The poroelastic characteristics of the rock need to be known for better understanding and modeling the performance of rock under in-situ conditions. One of the key concepts about poroelastic is the effective stress introduced by Terzaghi (1936, 1943) and Biot (1941). This concept suggests that pore pressure helps counteract the mechanical stress carried through grain-to-grain contact. The relationship is:

$$\sigma' = \sigma - \alpha p_p \tag{3.26}$$

where σ' is the effective stress carried by the matrix called effective stress; *Pp* is the

stress carried by pore fluid called pore pressure; σ is the total stress related to the two above stresses; and α is a constant called Biot's coefficient.

Since both the elastic properties (Nur and Nyerlee, 1971) and the fracture properties (Brace and Martin, 1968, Bruno and Nakagawa, 1991, and jaeger et al. 2007) are controlled by the effective stress, it is of critical importance to accurately determine the Biot's coefficient. Based on the concept of effective stress, many methods have been presented to improve the accuracy and efficiency of the Biot's coefficient measurement.

Geertsma (1957) and Skempton (1961) indicated a conventional technique to calculate Biot's coefficient by using equation:

$$\alpha = 1 - \frac{K}{K_s} \tag{3.27}$$

where K is the bulk modulus of the rock and K_s is the matrix modulus of the rock, which are both measured in two different experiments. In the first experiment, K is obtained by setting the pore pressure to zero; and in the second experiment, K_s is obtained by setting the pore pressure and confining pressure equal to each other. Azeemuddin (2002) improved this technique by measuring and K_s with “static” and “dynamics”" methods. This is the conventional method for measuring Biot's coefficient. It shows that Biot's coefficient will be a function of the bulk modulus and the matrix bulk modulus. If the rock stiffnesses are near the matrix bulk modulus, then Biot's coefficient will approach zero and the pore pressure will have no impact on the effective stress.

Franquet (1999) proposed a technique to measure Biot's coefficient using equation:

$$\alpha = \frac{\Delta V_p}{\Delta V} \tag{3.28}$$

where ΔV_p is the variation of the pore volume, and ΔV is the variation of the total rock volume. Because these parameters are evaluated through measurement of the amount of fluid volume drained from the rock sample, an accurate pore volume measurement is needed. However, when testing the tight rock samples, we use gas instead of fluid due to the low permeability; this method will cause leakage due to the long operating time. Franquet (1999) also developed a "Mohr envelope" method to calculate the Biot's coefficient, but this method needs several tests to define the envelope.

Qiao (2012) determined the Biot's coefficient under the assumption that the permeability follows the effective-stress law. The author pointed out that the Biot's coefficient is a function of the permeability, pore pressure, and confining pressure. However, it is difficult to find the variation in permeability when the rock is tight. In this paper a new method is proposed so that an experiment can be carried out and the result is easy to be analyzed. This method simplified the measuring procedures to obtain the Biot coefficient by recoding the variation of the confining pressure used to keep the volume of sample constant while altering the pore pressure. In this proposed method, samples only need to be measured once, which is fewer than conventional methods, whose procedures require multiple core samples. Therefore, the proposed method can be accomplished

significantly quicker.

Measurement Principle

To better understand the new Biot's coefficient measurement, it is necessary to introduce the derivation of the governing equation. The equation is derived by making the following assumptions: the core is homogeneous, the properties of the rock are constant, and the core and fluid are isothermal.

The bulk modulus of the rock is defined as the ratio of the change in stress to the strain, expressed as follow:

$$K = \frac{\Delta\sigma'}{\Delta\varepsilon_v} \tag{3.29}$$

where $\Delta\sigma'$ is the variation of the effective stress, and $\Delta\varepsilon_v$ is the variation of the volumetric strain ε_v. Combining Equation 3.29 with Equation 3.26 we have:

$$K = \frac{\Delta\sigma'}{\Delta\varepsilon_v} = \frac{\Delta(\sigma - \alpha P_p)}{\Delta\varepsilon_v}$$

Rearranging above equation, we get:

$$\alpha = \frac{\Delta\sigma - K\Delta\varepsilon_v}{\Delta P_p} \tag{3.30}$$

Equation 3.30 can be simplified if we can make $\Delta\varepsilon_v$ zero, which means the volume of the rock sample is constant, and assuming K is constant.

$$\alpha = \frac{\Delta\sigma}{\Delta P_p} \tag{3.31}$$

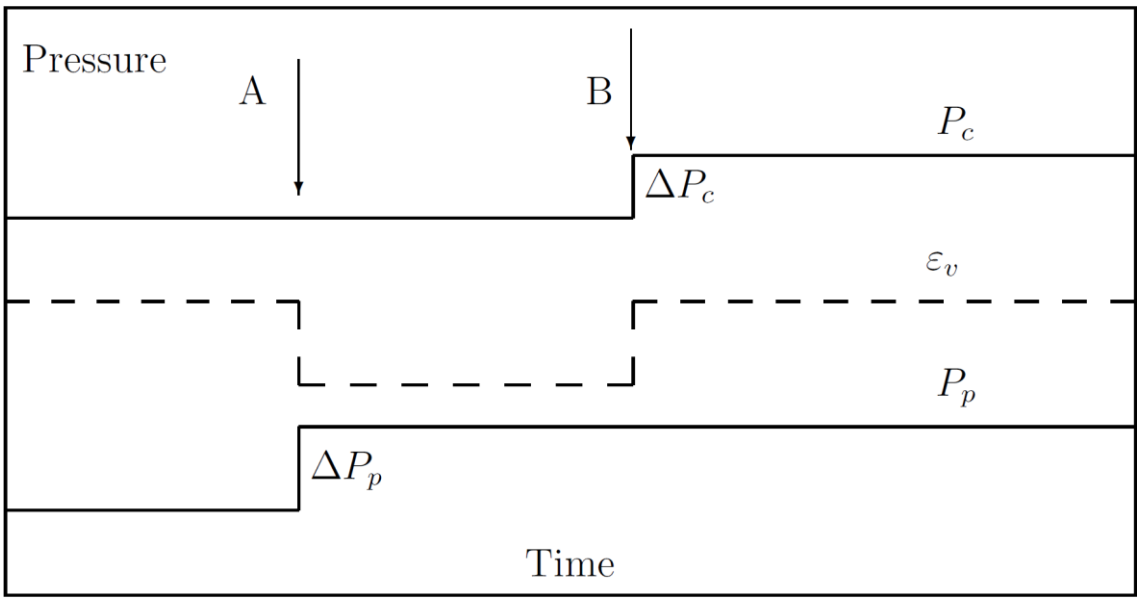

Figure 3.19 Schematic diagram of Biot's coefficient measuring process

Figure 3.19 shows the theoretical procedure. Once equilibrium has been attained, the pore pressure is increased P_P at time "A". This causes a decrease in the volumetric strain ε_v. The volumetric strain ε_v then returns to its original value at time "B" as the confining pressure P_c is increased ΔP_c. Finally, the Biot's coefficient can be calculated as a ratio as shown in Equation 3.31.

Measurement Procedure

Two problems arise when performing this experiment: 1). determine whether the volume of the sample has changed or not; 2). determine the magnitude that the confining pressure needs to be increased ΔP_c after the pore pressure has been increased ΔP_P to return the volumetric strain ε_v back to its original value. These problems can be solved with the

advent of high speed data-acquisition systems, accurate pressure transducers, strain gages, and digital computers.

Strain gages are attached on the wall of the core sample to monitor the variation of the core volume. There are an axial strain gage and a radial strain gage at one side of the sample; in addition, one more axial strain gage is on the other side of the sample (Figure 3.12). These strain gages will measure axial strain ε_a with Equation (3.19); and radial strain ε_r with Equation (3.18) during the experiment.

Let L as the original length of the sample, r as the original radius of the sample, and V as the original volume of the sample. Because the sample shape is cylindrical, the volumetric strain is expressed as follows:

$$\varepsilon_v = \frac{\Delta V}{V} = \frac{\pi(r+\Delta r)^2(L+\Delta L) - \pi r^2 L}{\pi r^2 L} \tag{3.32}$$

Because the strains are small, the high order terms can be neglected and Equations (3.18, 3.19, and 3.32) can be combined resulting in the following equation (Equation 3.33) to represent the volumetric strain:

$$\varepsilon_v = \varepsilon_a + 2\varepsilon_r \tag{3.33}$$

In this case, the first problem is solved by using the axial and radial strain gages. The second problem can be solved by using AutoLab-1500.

The measurement procedure is as the following:

1) Install the sample into AutoLab-1500 (like the permeability test part)
    a. Mount the sample in a core holder with flexible rubber sleeves at both ends of the plug (Figure 3.8). Connect the upstream end-cap to a servo-controlled hydraulic intensifier, which is used to control and monitor the upstream pressure. The downstream pressure at the other end of the sample is monitored by a miniature pressure transducer, which is located in the downstream end-cap.
    b. Put the core holder into the pressure vessel, which is filled with mineral oil, and apply confining pressure to a desired level.
    c. Fill the upstream reservoir with dry nitrogen. Because the permeability of Bakken sample is low, gas is used as the test fluid in the experiment.
    d. Connect the upstream reservoir with the sample to the downstream reservoir.
    e. Increase the upstream pressure to a desired level.
    f. Wait until the equilibrium of the downstream and upstream pressure reached.
2) Configure AutoLab-1500 system to the confining pressure self-adjusting mode so that the volumetric strain will keep constant
3) Increase the upstream pressure to the next level.
4) Wait until both the downstream pressure and the confining pressure reach their new equilibrium.

5) Record the variations of confining pressure and pore pressure, respectively.

6) Repeat 3) to 5) by increasing or decreasing the upstream pressure. Figure 3.20 shows one record of the experiments.

7) Remove the sample from the core holder, and disconnect the core from the end-caps.

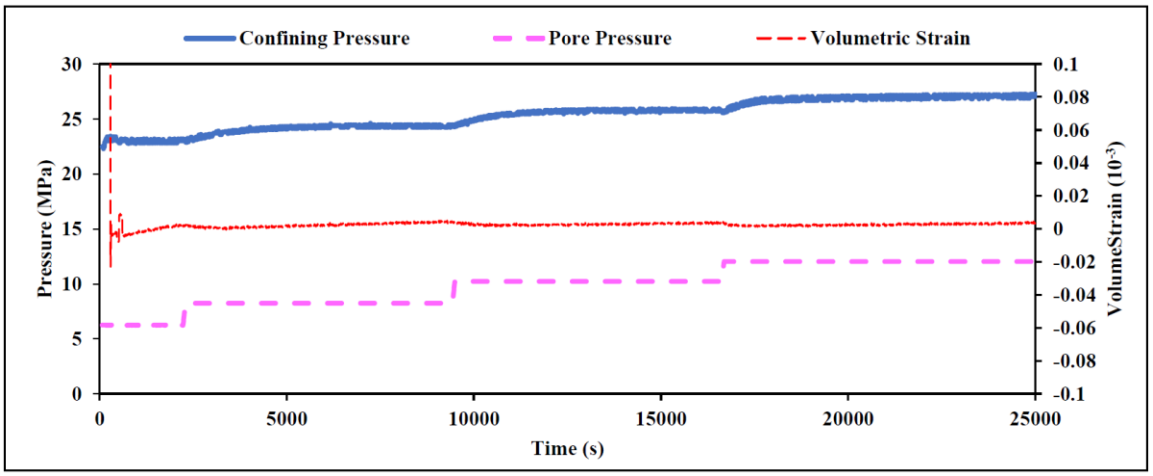

Figure 3.20 Recording curves in one experiment

Table 3.2 Biot's coefficient test on one sample

Pore Pressure (MPa)		Confining Pressure (MPa)		Biot's Coefficient
from	to	from	to	
6.20	8.20	22.87	24.27	0.70
8.20	10.20	24.27	25.77	0.75
10.20	12.30	25.77	27.09	0.63
Average				0.69

The results of the experiment recorded by Figure 3.20 are summarized in Table 3.2. After

the pre-equilibrium was achieved at pore pressure of 6.2 MPa and confining pressure of 22.87 MPa, the pore pressure was increased to 8.20, 10.20, and 12.30 MPa. To keep the volume of the sample constant, the confining pressure is raised to 24.27, 25.77, and 27.09 MPa automatically by AutoLab-1500. The Biot's coefficient of the sample then was obtained from Equation 3.31. The average Biot's coefficient of the sample is 0.69.

3.4.4. Compressive Strength

After all non-destructive were completed, we measured the compressive strength of Bakken sample with triaxial compression test. The equipment used to do triaxial compression test is AutoLab-1500.

The tri-axial compression test was done with a much lower deformation rate (0.005 mm per minute), the confining pressure is kept constant, and the axial stress in the loading is increased until the sample failed. The peak axial strength was recorded. The procedure for conducting the experiment is almost the same as the measurement of static Young's modulus, except that no strain gage was used and velocity transducers are not in the end-caps in this experiment. The following shows the procedure:

1) Jacket the sample with copper foil.
2) Insert the jacketed sample into the pressure vessel.
3) Fill the pressure vessel with mineral oil.
4) Increase the confining pressure to designed level.
5) Increase the differential stress and the confining pressure to the initial value for

the tri-axial compression measurement.

6) Set the loading rate.

7) Start tri-axial compression test, and collect the data.

8) End tri-axial compression test when the sample failed.

CHAPTER IV

EXPERIMENTAL RESULTS AND ANALYSIS

4.1. Porosity

4.1.1. Experiment Result

The porosity was measured successfully for 237 specimens among the total 240 Bakken specimens. The mean porosity of the specimens is 4.922% with a standard deviation 1.578 (Table 4.1). The porosity is normal distribution (Figure 4.1). Moreover, the porosity means of the Upper, Middle and Lower Bakken are low, in the range from 4 to 6%; and the Lower Bakken has the highest porosity and smallest distribution range, which is shown clearly in Figure 4.2.

Table 4.1 Statistic results of porosity test

Member of Bakken Formation	Total Numbers	Success Numbers	Porosity (%)			Standard Deviation
			Min	Mean	Max	
Upper Bakken	42	40	0.800	4.265	7.900	2.088
Middle Bakken	140	139	1.900	4.792	8.7	1.381
Lower Bakken	58	58	2.200	5.688	10.400	1.329
Total	240	237	0.800	4.922	10.400	1.578

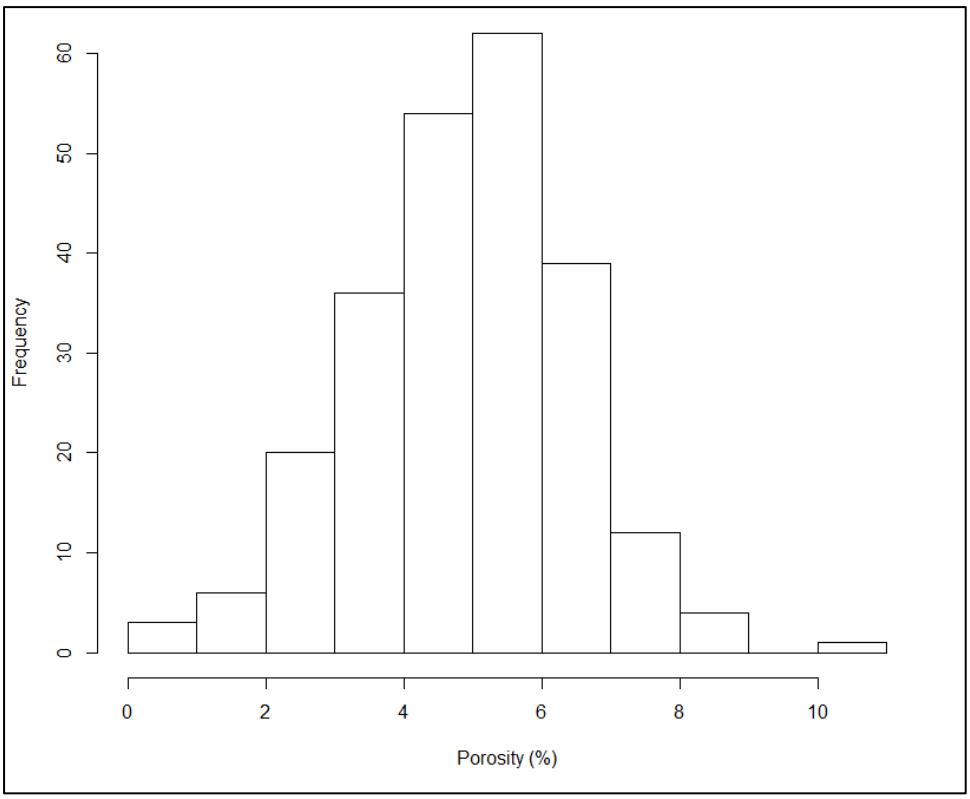

Figure 4.1 Histogram of porosity from 237 Bakken samples

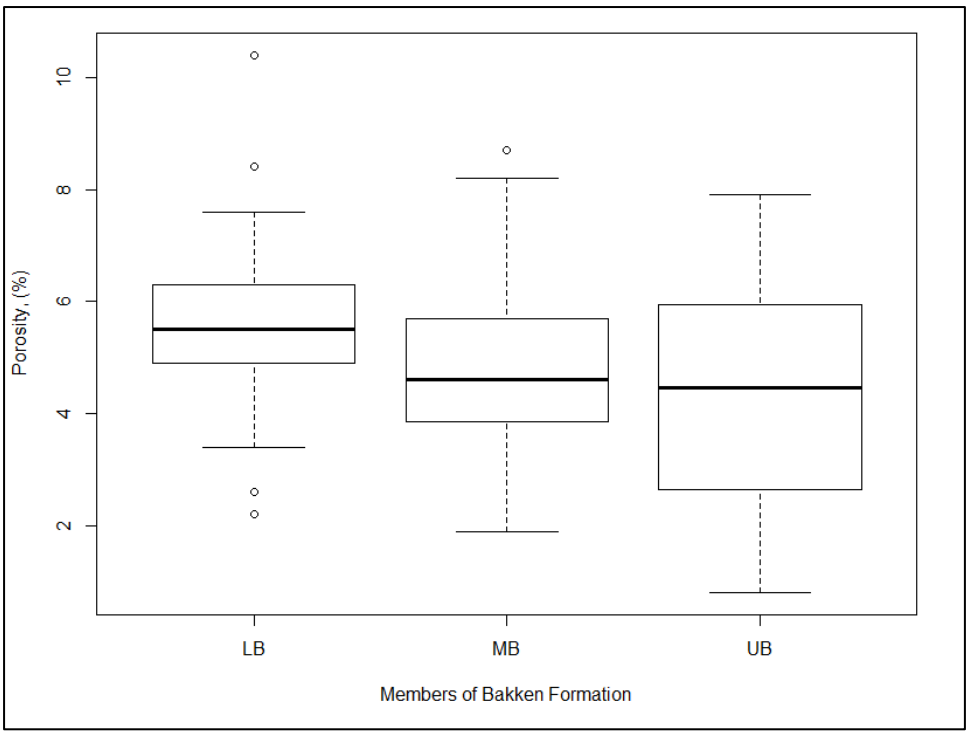

Figure 4.2 Boxplot of the porosity for three members of Bakken Formation

4.1.2. Impact of Freezing

Recall that the freezing sample method is used in preparing the plug to overcome the sampling difficulty. It is undoubted that the freezing will alter the rock texture and structure thus the rock properties such as porosity and permeability, but like discussed before, to the best of our knowledge it is the most successful approach to prepare the shale core sample for lab test. Therefore, to obtain original rock properties, it is imperative to quantify the difference before and after the freezing. Here we investigated how the porosity changes during freezing process as below.

The effect of temperature on elastic properties of porous materials had been studied by researchers of different fields, including petroleum engineering, civil engineering, and chemical engineering. For the purposes of this research we reviewed the studies that focused on the porosity change as a function of temperature. These researches can be classified into two main categories according to temperature below and above ice melting point (or water freezing point). The first category targeted temperature higher than ice melting point (or water freezing point). Another investigated temperature is lower than ice melting point under which the expansion of ice becomes the main cause that alters the rock properties. Followings list some important researches that can be identified as milestones that advance the understanding of effect of temperature on rock properties.

Somerton et al. (1965) studied the thermal effect on sandstone in the range of 400 to 800 ^{o}C. Their works showed that large changes in physical properties occur as a result of

heating and subsequent cooling to room temperature. They believed that the alteration of rock properties is caused by a number of reactions occur during heating, which include the differential thermal expansion of the quartz grains, the dissociation of dolomite at higher temperatures, and the "firing" of clays at lower temperatures. Sanyal et al. (1974) investigated the effect of temperature on petrophysical properties of reservoir rocks. From their literature review, there was no definite result known about the effect of temperature on porosity. The bulk volume increases slightly (<1%) with temperature increase up to 200 ^{o}C. However, a cubic pore model was analyzed to simulate the change in pore structure due to thermal expansion of mineral grains and cement. The expansion of the grain spheres and the quartz cement due to temperature increase was calculated using the thermal expansion coefficients of quartz. Different degrees of cementation were considered in the model. Change of pore radius at different temperature levels were obtained by subtracting new cement thickness from new grain radius. Vodak et al. (2004) studied the effect of temperature on strength-porosity relationship for concrete material at various temperatures ranging from 25 to 280 ^{o}C. Their study depicted that porosity increases as a result of microcracking mainly due to thermal incompatibility of hardened cement paste and aggregate during heating. Tian et al. (2009) obtained similar results in their experimental studies on sandstone, claystone, clayey sandstone, and sandy claystone where specimens were heated up to 1000 ^{o}C. It was observed that cracks were generated on the rock samples, especially claystone, due to the difference in thermal expansion properties of different minerals in the rock. Yao et al. (2012) and Hu et al.

(2012) presented further investigations on the microcracking mechanism during the procedure of heating rock and coal samples. In general, at the initial heating stage, increasing of temperature leads to the expansion of rock matrix, but the temperature is not high enough to generate microcracks. Therefore, at the initial heating stage, the porosity would slightly drop, or keep constant because of expansion of matrix and the inelastic property preventing restoration of deformation when specimens are cooled to ambient temperature. As the temperature continuously increases, the induced thermal stress reaches and exceeds the strength of matrix, thus leads to the generation of microcracks and increase of porosity. Therefore, there exists a "threshold temperature", where the sudden jump of porosity is observed, as the thermal stress becomes higher than the matrix strength and creates cracks in rocks. Yuan et al. (2012) conducted experimental study and simulated the effect of temperature on the voids in cement under high pressure and high temperature conditions.

The other studies have paid attention to the effect of freezing on rock properties. Hundere (1984) investigated the changes of unconsolidated core properties after freezing. Kindt (1985) studied the effect of freezing on permeability of unconsolidated sandstone through experimental measurement. Torsaeter and Beldring (1987) analyzed the effect of freezing on permeability of unconsolidated to slightly consolidated rocks and core plugs. Increasing in porosity, which ranges from 0.7% to 9.6%, was observed in their experimental data. Neaupane et al. (1999) presented a coupled thermo-hydro-mechanical

model to simulate the freezing and thawing process. Their study focused on the effect of phase change of pore water on the deformation of material. No discussion of the change of porosity by freezing is available in the paper. Coussy (2005) studied the poromechanics of freezing materials. The study focused on the liquid saturation degree as a function of temperature, and ice-dependent poroelastic properties.

From the descriptions above, most of the previous researches focused on the high temperature effect, or the effect of phase change of the pore water on the matrix structure in freezing process. The induced thermal stress due to freezing may result in fractures. It is expected that there also exists a "threshold temperature" during freezing, where sudden change of porosity due to fracturing would be observed. Some of aforementioned researches compared the rock or specimen porosity before and after freezing, and the porosity change with the variation of temperature.

Unfortunately it is unfeasible to measure porosity of Bakken shale core plug before freezing, because the Bakken shale core has to be frozen in order to drill plug successfully due to its brittle nature. In this case, we quantified the difference in rock porosity before and after the freezing basing on experimental data from numerous rock specimens. To do so, porosities of the samples were measured before they were frozen. Then samples were stored in freezer and frozen at temperatures of -13.8 and -85 ^{o}C for more than one week. After that they were taken out of freezer and allowed to return to temperature of 20 ^{o}C. Their porosities were measured again once temperature reaches

equilibrium.

Table 4.2 Porosity change caused by freezing

Samples	Diameter	Length	Porosity Φ(%)			$(\Phi - \Phi 20)/\Phi 20$		
	mm	mm	20 °C	-13.8 °C	-85 °C	20 °C	-13.8 °C	-85 °C
1	23.54	42.25	12.512	19.197	14.127	0.000	0.534	0.129
2	24.3	51.55	10.969	14.472	14.579	0.000	0.319	0.329
3	24.65	28.44	16.624	21.496	18.006	0.000	0.293	0.083
4	24.69	49.98	11.296	13.764	12.620	0.000	0.218	0.117
5	24.25	52.58	12.755	14.770	13.886	0.000	0.158	0.089
6	24.38	52.69	13.504	14.968	14.168	0.000	0.108	0.049
7	24.67	55.25	16.481	17.941	18.068	0.000	0.089	0.096
8	24.69	52.6	13.501	14.694	14.470	0.000	0.088	0.072
9	24.95	51.05	18.478	20.029	18.870	0.000	0.084	0.021
10	24.73	51.56	18.807	20.302	19.698	0.000	0.079	0.047
11	24.82	51.55	15.057	15.976	15.531	0.000	0.061	0.031
12	38.44	76.15	13.999	14.759	14.574	0.000	0.054	0.041
13	24.65	58.38	17.068	17.952	17.770	0.000	0.052	0.041
14	38.08	74.33	12.958	13.583	13.784	0.000	0.048	0.064
15	38.43	76	13.382	14.006	13.832	0.000	0.047	0.034
16	38.43	76.26	14.868	15.534	15.574	0.000	0.045	0.047
17	24.45	53.91	22.483	23.485	23.491	0.000	0.045	0.045
18	38.48	76.18	12.114	12.652	12.090	0.000	0.044	-0.002
19	38.42	76.25	13.699	14.209	14.493	0.000	0.037	0.058
20	38.25	75.21	13.212	13.646	13.804	0.000	0.033	0.045
21	38.47	74.14	13.728	14.125	13.931	0.000	0.029	0.015
22	24.76	46.6	12.995	13.364	14.038	0.000	0.028	0.080
23	38.38	75.77	13.778	14.138	13.951	0.000	0.026	0.013
24	25	51.95	15.194	15.569	16.415	0.000	0.025	0.080
25	38.42	76.26	13.802	14.134	14.209	0.000	0.024	0.029
26	24.63	50.37	22.060	22.566	24.060	0.000	0.023	0.091
27	24.81	49.62	15.094	15.311	15.583	0.000	0.014	0.032
28	38.44	76.05	14.238	14.350	14.268	0.000	0.008	0.002
29	24.3	52.37	12.875	12.953	15.676	0.000	0.006	0.218
30	24.27	52.95	17.583	17.684	18.736	0.000	0.006	0.066

Table 4.2 Cont

31	50.12	102.78	14.963	15.028	14.905	0.000	0.004	-0.004
32	38.47	76.14	12.412	12.426	12.603	0.000	0.001	0.015
33	50.27	105.05	15.611	15.591	15.491	0.000	-0.001	-0.008
34	38.3	75.81	13.334	13.279	13.177	0.000	-0.004	-0.012
35	38.2	76.15	13.547	13.453	13.512	0.000	-0.007	-0.003
36	50.16	102.78	15.057	14.910	14.936	0.000	-0.010	-0.008
37	25.68	50.31	21.884	21.660	22.118	0.000	-0.010	0.011
38	50.24	103.43	15.681	15.510	15.562	0.000	-0.011	-0.008
39	38.46	76.03	14.976	14.803	14.600	0.000	-0.012	-0.025
40	38.35	76.25	14.156	13.959	14.192	0.000	-0.014	0.003
41	38.46	78.17	16.881	16.635	16.845	0.000	-0.015	-0.002
42	24.78	50.78	16.586	16.338	16.901	0.000	-0.015	0.019
43	24.47	48.81	11.164	10.917	15.535	0.000	-0.022	0.392
44	24.84	48.97	15.599	15.234	15.533	0.000	-0.023	-0.004
45	38.45	76.15	14.352	13.970	13.954	0.000	-0.027	-0.028
46	24.5	52.55	15.155	14.658	15.408	0.000	-0.033	0.017
47	24.08	51.48	15.224	14.713	15.698	0.000	-0.034	0.031
48	24.17	50.09	9.821	9.386	13.411	0.000	-0.044	0.366
49	24.74	51.49	16.681	15.858	17.042	0.000	-0.049	0.022
50	24.58	51.65	13.062	12.199	15.665	0.000	-0.066	0.199
51	24.83	51.85	16.718	15.605	16.960	0.000	-0.067	0.014
52	24.8	50.45	15.283	14.235	17.547	0.000	-0.069	0.148
53	24.65	52.67	12.503	11.583	15.378	0.000	-0.074	0.230
54	24.17	50.45	11.694	10.684	13.892	0.000	-0.086	0.188
55	24.4	52.27	11.843	10.799	13.288	0.000	-0.088	0.122
56	24.25	52.56	13.886	12.305	16.040	0.000	-0.114	0.155

Two series of different size specimens were used in this work. The first series has a dimension of one inch in diameter by two inches in length, and another has a dimension of two inches in diameter by four inches in length. The porosities of rock before and after freezing were measured. Thus we obtain three porosities for each specimen: one before

freezing, one after freezing at -13.8 ^{o}C, and one after freezing at -85 ^{o}C.

To demonstrate the change of porosity by freezing distinctly, we calculate the relative porosity change using porosity of rocks at 20 ^{o}C as the base. Table 4.2 shows the experiment results.

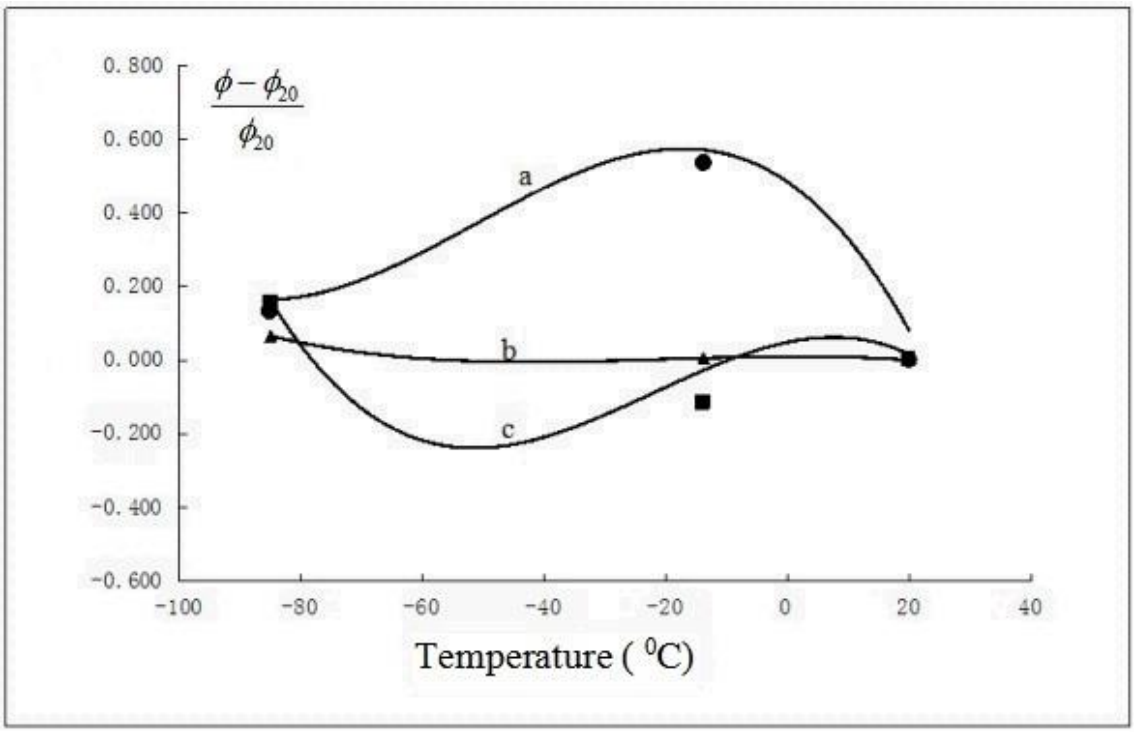

Figure 4.3 Regression analysis of porosity change caused by freezing

Based on the test data, three kinds of porosity change by freezing can be identified as shown in Figure 4.3, and they are corresponding to different types of rocks. For the first type (a), whose lithology is argillaceous sandstone, the porosity increases as the rock was frozen, and reaches maximum at temperature barely lower than 0 ^{0}C. After that local maximum, porosity declines as temperature is reduced further. For the second type (b), whose lithology is clean sandstone, the trend is similar to first type but with smaller

change. The porosity change by freezing is very small until temperature reaches the "threshold temperature", beyond that point the porosity begins to increases quickly. The third type (c), whose lithology is sandstone with high calcium carbonate concentration, follows the same trends as first and second types. A local maximum porosity is seen at temperature barely lower than 0 ^{0}C, but the change of porosity lies between first and second types. A "threshold temperature" also can be found as the temperature decrease continuously. The porosity increases again when the temperature is lower than the "threshold temperature".

Porosity change is the combined effects of expansion of the water inside the core due to phase change and the contractions of the matrix of the core and ice. When the core is stored in freezer at temperature lower than freezing point, the freezing causes the water inside the core to expand due to the fact that ice occupies a larger volume than liquid water. The relative volume change is

$$\frac{\Delta V_{\text{expansion}}}{V_{water}} = \frac{V_{ice} - V_{water}}{V_{water}} = 8.7\% \tag{4.1}$$

The expansion volume due to water phase change is

$$\Delta V_{\text{expansion}} = 0.087 V_{water} = 0.087 \phi S_w V_{bulk,core} \tag{4.2}$$

During the freezing, both ice and rock matrix contract. The volume change due to the contraction can be estimated using the thermal expansion coefficient. The contraction volumes of ice and rock matrix are calculated by

$$\begin{aligned}\Delta V_{\text{contraction,ice}} &= V_{\text{ice}}\left(T_{\text{freezing point}} - T_{\text{freezer}}\right)\alpha_{\text{ice}} \\ &= 1.087\phi S_w V_{bulk,core}\left(T_{\text{freezing point}} - T_{\text{freezer}}\right)\alpha_{\text{ice}}\end{aligned} \tag{4.3}$$

and

$$\begin{aligned}\Delta V_{\text{contraction,matrix}} &= \sum_i^n V_{i,\text{mineral}}\left(T_{\text{freezing point}} - T_{\text{freezer}}\right)\alpha_{i,\text{mineral}} \\ &= V_{bulk,core}\left(1-\phi\right)\sum_i^n f_{i,\text{mineral}}\left(T_{\text{freezing point}} - T_{\text{freezer}}\right)\alpha_{i,\text{mineral}}\end{aligned} \tag{4.4}$$

respectively.

where

$\alpha_{\text{ice}} = 50\times10^{-6}\ 1/^{\circ}\text{C}$

and the coefficients of thermal expansion of different minerals are listed in Table 4.3.

Table 4.3 Thermal expansion coefficients of common minerals in rock

Mineral	Thermal Expansion Coefficient	Reference
Quartz	$0.77\sim1.4\times10^{-6}$ 1/°C	http://www.engineeringtoolbox.com/linear-expansion-coefficients-d_95.html
Alkali Feldspar	$14\sim17\times10^{-6}$ 1/°C	Hovis, G., et al., 2008, A simple predictive model for the thermal expansion of $AlSi_3$ feldspars.
Plagioclase Feldspar	$10\sim17\times10^{-6}$ 1/°C	Tribaudino, M., et al., 2010, Thermal expansion of plagioclase feldspars:
Calcium Carbonate	$6\sim9\times10^{-6}$ 1/°C	http://www.supercivilcd.com/THERMAL.htm
Calcium Carbonate	8×10^{-6} 1/°C	http://www.engineeringtoolbox.com/linear-expansion-coefficients-d_95.html

Combing Equations (4.2), (4.3), and (4.4) we have the total volume change, which is

$$\Delta V_{total} = \Delta V_{\text{contraction,ice}} + \Delta V_{\text{contraction,matrix}} - \Delta V_{\text{expansion}}$$
$$= V_{bulk,core}\begin{bmatrix} 1.087\phi S_w \left(T_{\text{freezing point}} - T_{\text{freezer}}\right)\alpha_{\text{ice}} \\ +(1-\phi)\sum_i^n f_{i,\text{mineral}} \left(T_{\text{freezing point}} - T_{\text{freezer}}\right)\alpha_{i,\text{mineral}} \\ -0.087\phi S_w \end{bmatrix} \quad (4.5)$$

Therefore the relative volume change is

$$\frac{\Delta V_{total}}{V_{bulk,core}} = \begin{bmatrix} 1.087\phi S_w \left(T_{\text{freezing point}} - T_{\text{freezer}}\right)\alpha_{\text{ice}} + \\ (1-\phi)\sum_i^n f_{i,\text{mineral}} \left(T_{\text{freezing point}} - T_{\text{freezer}}\right)\alpha_{i,\text{mineral}} \\ -0.087\phi S_w \end{bmatrix} \quad (4.6)$$

Equation (4.6) gives the incremental porosity at freezer temperature. So the rock porosity at freezer temperature is

$$\phi_{freezer\ temperature} = \phi + \begin{bmatrix} 1.087\phi S_w \left(T_{\text{freezing point}} - T_{\text{freezer}}\right)\alpha_{\text{ice}} \\ +(1-\phi)\sum_i^n f_{i,\text{mineral}} \left(T_{\text{freezing point}} - T_{\text{freezer}}\right)\alpha_{i,\text{mineral}} \\ -0.087\phi S_w \end{bmatrix} \quad (4.7)$$

If the induced stress is less than the adhesive strength of rock and the rock is elastic, the rock should restore to its original condition when the temperature is restored to original temperature. Unfortunately no rock is completely elastic. Therefore rock cannot restore to its original condition exactly even the rock is not damaged by the induced stress. The residual porosity difference as a result of freezing-unfreezing cycle depends on the water and the percentage of inelastic component in rock.

If the induced stress is higher than the adhesive strength of rock, rock porosity after

freezing-unfreezing cycle will be larger than the original porosity because the microcracks and plastic component in the rock prevent the rock from restoring to original condition when temperature return to original value. To evaluate the occurring of microcrack it is necessary to introduce the definition of volumetric strain, which is defined as the ratio of the change in volume of the body to its original volume (Jaeger, et al., 2007).

$$\varepsilon_{\mathrm{V}} = \frac{\Delta V}{V_{\text{original}}} \tag{4.8}$$

Recalling that the volumetric strain is the sum of the three principal normal strains we have

$$\varepsilon_{\mathrm{V}} = \varepsilon_1 + \varepsilon_2 + \varepsilon_3 \tag{4.9}$$

The relationships between the three principal normal stresses and strains give us

$$\sigma_1 = \lambda\varepsilon_{\mathrm{V}} + 2G\varepsilon_1 \tag{4.10}$$

$$\sigma_2 = \lambda\varepsilon_{\mathrm{V}} + 2G\varepsilon_2 \tag{4.11}$$

$$\sigma_3 = \lambda\varepsilon_{\mathrm{V}} + 2G\varepsilon_3 \tag{4.12}$$

Summing up the three principal stresses gives

$$3\tau_m = \sigma_1 + \sigma_2 + \sigma_3 = (3\lambda + 2G)\varepsilon_{\mathrm{V}} \tag{4.13}$$

The mean stress is related to the volumetric strain through

$$\tau_m = \left(\lambda + \frac{2}{3}G\right)\varepsilon_{\mathrm{V}}$$
$$= \left(\lambda + \frac{2}{3}G\right)\begin{bmatrix} 1.087\phi S_w\left(T_{\text{freezing point}} - T_{\text{freezer}}\right)\alpha_{\text{ice}} + \\ (1-\phi)\sum_i^n f_{i,\text{min eral}}\left(T_{\text{freezing point}} - T_{\text{freezer}}\right)\alpha_{i,\text{min eral}} \\ -0.087\phi S_w \end{bmatrix} \quad (4.14)$$

where

$$\lambda = \frac{2Gv}{1-2v} \quad (4.15)$$

If the mean stress calculated from Equation (4.14) is higher than adhesive strength of rock, micorcrack will be created and increase in porosity will be expected.

Analysis of experimental data indicates that there is a “threshold temperature” for rock. When the rock is frozen at temperature high than “threshold temperature” and restored to original temperature, porosity decreases. Otherwise porosity increases. At temperature between freezing point and “threshold temperature”, the expansion resulting from water phase change to ice dominates over the contractions of rock matrix and ice. The expanded volume is larger than the contracted volume. The deformation occurring at this temperature range is partially inelastic and the rock cannot restore to original condition even temperature is restored to original temperature. It should be noted that the induced stress is below the adhesive strengths between cements and grains or the strength of matrix under this temperature range. At temperature lower than the “threshold temperature”, the contractions of ice and rock matrix dominates over the expansion due to the water phase change. The induced thermal stress resulting from strain caused by

contraction reaches and exceeds the adhesive strengths between cements and grains or the strength of matrix, thus lead to the creation of microcracks. These microcracks are the main reason porosity increases. Under such condition the expanded volume is smaller than the contracted volume. The deformation is damaging and irreversible, and again the rock cannot restore to original condition after temperature is restored to original temperature. Obviously the "threshold temperature" is a function of rock type, rock structure, texture, mineral composition, rock strength, water saturation, mineral hydration, and porosity. To calculate an accurate porosity change, it is necessary to know the volumetric fraction of minerals in rock, as well as the coefficient of thermal expansion of each mineral.

4.2. Permeability

4.2.1. Experiment Result

Permeability was measured for all 240 Bakken specimens using the Oscillating Pulse method with the AutLab-1500 (Boitnott 1997). The confining pressure and pore pressure are 30 MPa and 8 MPa, respectively. The success rate of test is about 85.5%. The median permeability of the specimens is 0.63 μD with a standard deviation 5169.97 (Table 4.4). Figure 4.4 shows that the permeability of the Middle Bakken is lower than that from Upper and Lower Bakken; moreover the permeabilities of the Upper Bakken and the Lower Bakken spread widely, even have much large permeability. These features may cause by the fractures in the Upper and Lower shale core plugs. Based on this hypothesis,

we not only investigated the existing methods to ascertain fractures, but proved one method to identify fractures in tight rocks with porosity-permeability relation as well.

Table 4.4 Statistic result of permeability test

Member of Bakken Formation	Total Numbers	Success Numbers	Permeability (μD)				Standard Deviation
			1st Quarter	Median	Mean	3rd Quarter	
Upper Bakken	42	33	6.79	239.00	6613.00	6760	10551.83
Middle Bakken	140	121	0.07	0.30	127.47	1.87	672.83
Lower Bakken	58	51	0.08	1.45	1185.67	72.40	3848.31
Total	240	205	0.09	0.63	1434.78	44.00	5169.97

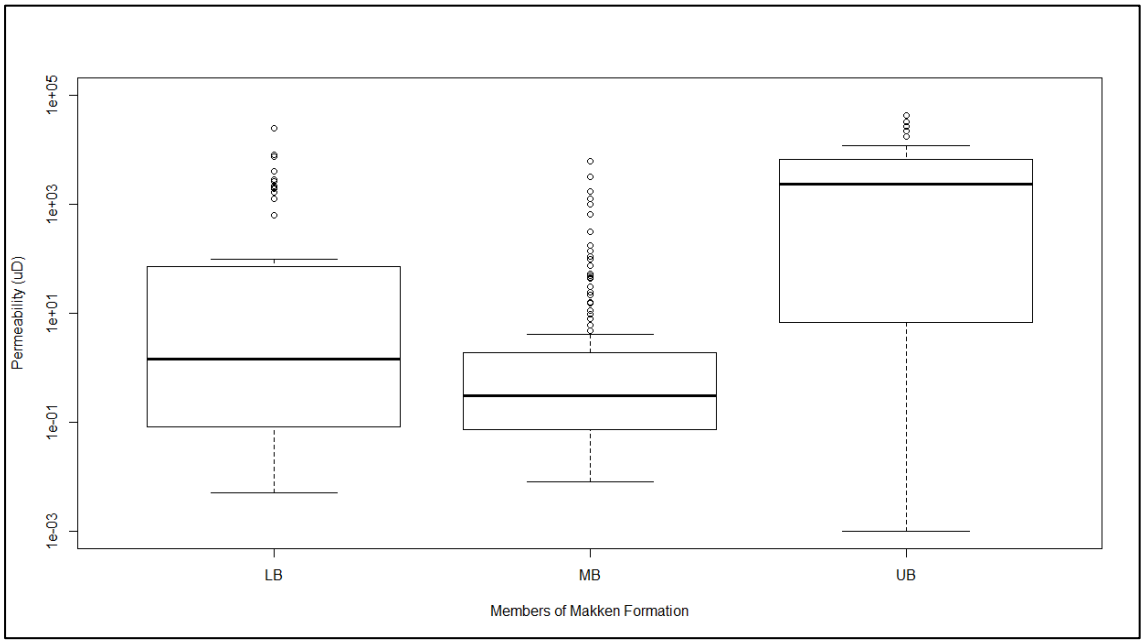

Figure 4.4 Boxplot of the porosity for three members of Bakken Formation

4.2.2. Identify fractures with porosity-permeability relation

Identification of fractures in the rock is critical in rock characterization and important to design multistage fracturing in horizontal well to maximize the production. Knowing the fracture direction helps determine the direction of horizontal lateral to maintain wellbore

stability during drilling and create long fractures in multistage fracturing. Therefore methods that can identify fractures and determine their directions are highly desired. Nelson (1976) conducted experiment to investigate the effect of temperature and confining pressure on fracture permeability in Navajo sandstone. Fertl and Rieke (1980) identified fractured shale by gamma ray spectral evaluation techniques. Thorpe (1981) characterized natural fractures in granitic rock using observation method. Brown and Scholz, (1985), Cart and Warriner (1987), Aviles, et al. (1987), applied fractal geometry to the objective description of rock fracture surfaces. Dennis and Slanden (1988) used imaging techniques consisting of Formation MicroScanner log and the Borehole Televiewer to locate the fracture on wellbore. Locker (1993) tracked the growth and interaction of microcracks using acoustic emission. Feng et al. (1958) mapped the fracture at exposed rock faces by applying close rang digital photogrammetry and geodetic total station. Labuz and Chen (2001), and Lin and Labuz (2010) utilized nondestructive technique of electronic speckle pattern interferometry to monitor the propagation of fracture initiated by a wedge indenter. Their experiments on Berea sandstone and Sioux quartzite showed a good agreement between the cavity expansion model and the experiments in terms of indentation pressure and size of the damage zone located beneath the indenter. El-Gezeery et al. (2008) employed real time logging while drilling resistivity imaging to identify fracture corridors in a fractured carbonate reservoir. Lin and Fairhurst (1991) used principle of combinatorial topology to analyze the three-dimensional network of fracture. Bravo and Aldana (2011) used different volume

curvature attributes to identify subtle faults and fractures in carbonate reservoirs. Han (2011) proposed an integrated method including electrical image tools such as well logging, core observation, production logs, and rate transient analysis, and outcrop observation to identify fractures. Stanchits et al. (2012) monitored the propagation of hydraulic fracture in heterogeneous rock samples using acoustic emission and ultrasonic transmission. Salehi and Ciezobka (2013) identified natural fractures in shale reservoir through the analysis of surface pumping parameters. Their analyses were confirmed by microseimic data and multiple production logs. Although imaging methods and other technologies have been used to characterize the fracture distribution, they are time consuming and expensive, and sometimes are constrained by the availability of equipment.

According to a capillary tube model of porous media (Ling, 2012), which should be followed by all fluid flow behaviors in the non-fractured core sample, the permeability is proportional to the square of porosity and inversely proportional to the cubic of tortuosity of rock. And empirical observations give a general relation between porosity and permeability as follow:

$$k = Ce^{n\varphi} \tag{4.16}$$

where C is a constant linear coefficient, and n is exponential coefficient.

It should be noted that C and n vary with different lithology. Same types of rocks share similar C and n unless there is/are fracture/s within them considering a small fracture can

contribute to the rock permeability significantly.

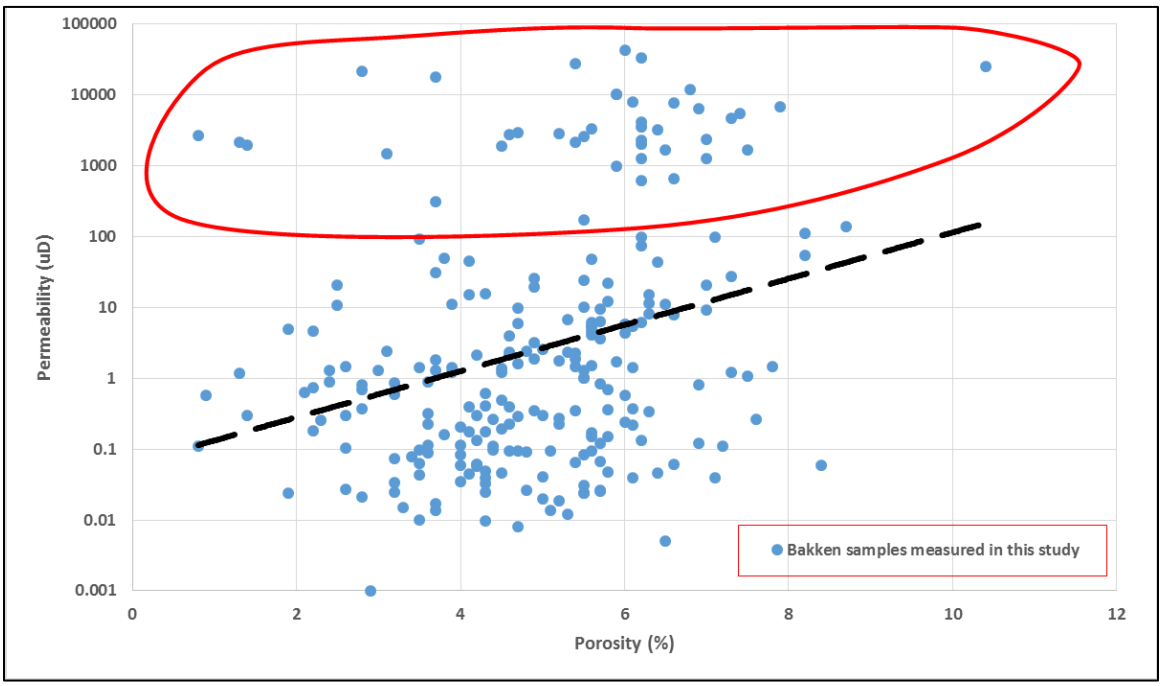

Figure 4.5 Porosity and permeability of the Bakken core plugs

Porosity and permeability of Bakken core plugs are plotted in Figure 4.5. The identification of fracture in the core plug is based on the following four principles: 1) similar rock type share the same porosity-permeability relation if no fracture exists, 2) fracture in the rock increases the rock permeability significantly, 3) fracture contributes a very small amount to the increase in porosity, and 4) porosity-permeability relation of fractured rock has a different trend from that of non-fractured rock due to the fracture's significant contribution to permeability.

Firstly, we identify samples with high permeability, which is a result of fracture contribution. High permeability causes the porosity-permeability relation deviate from the trend of non-fractured Bakken cores (as the dashed straight line) shown in Figure 4.5.

The high permeability samples that may contain fractures are marked by the red circle, and samples outside of red circle are believed to be fracture free. To develop the porosity-permeability relation for non-fractured core plugs, samples outside of red circle in Figure 4.5 are used to regress to estimate coefficients, C and n, in Equation 4.16. The regression gives C=0.0394 and n=0.5412 as shown in Figure 4.6. Therefore, the porosity-permeability relation for non-fractured Bakken cores becomes

$$k = 0.0394e^{0.5412\varphi} \tag{4.17}$$

To better understand the porosity-permeability relation of fractured Bakken cores, samples inside the red circle in Figure 4.5 are used to construct the relation and to evaluate coefficients, C and n, the plot in Figure 4.7 indicates that C=1977.9 and n=0.1153 for fractured cores, which are significantly different from those of non-fractured core correlation. The porosity-permeability relation for fractured Bakken cores becomes

$$k = 1977.9e^{0.1153\varphi} \tag{4.18}$$

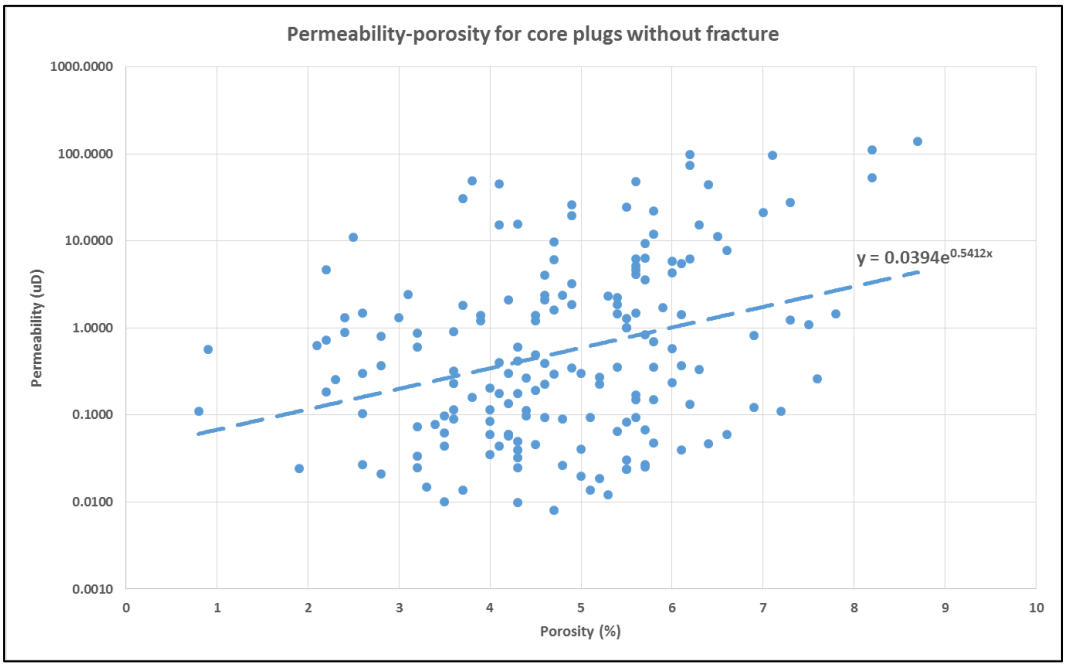

Figure 4.6 Porosity-permeability relation developed from core plugs without fracture

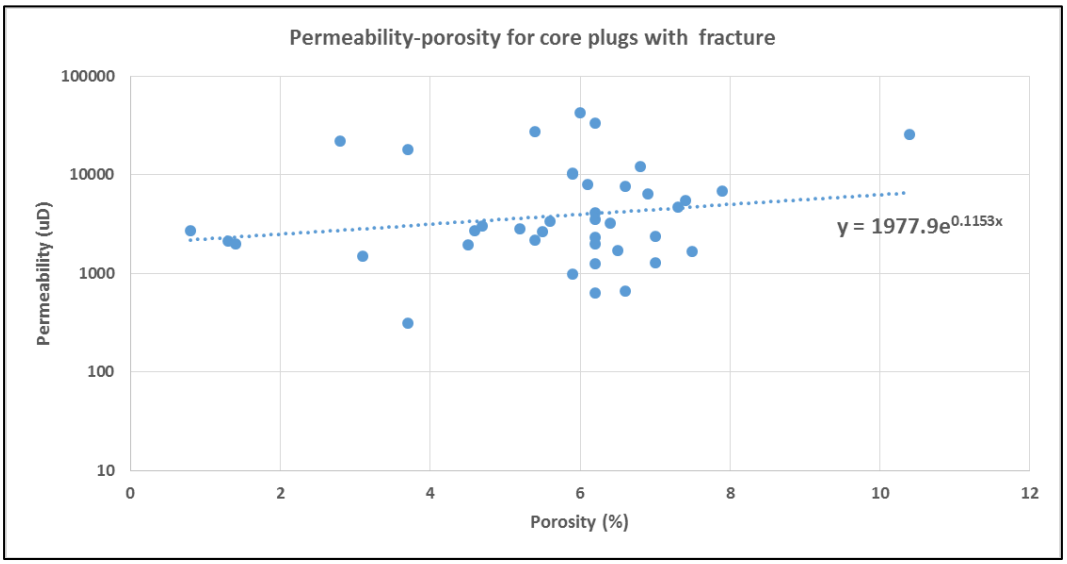

Figure 4.7 Porosity-permeability relation developed from core plugs with fracture

Equations (4.17) and (4.18) put the foundation for identifying fracture in Bakken core based on the porosity-permeability relation. It is reasonable to conclude that core with porosity-permeability relation similar to Equation (4.17) does not contains fracture, while core with porosity-permeability akin to Equation (4.18) contains fracture.

To validate the proposed method, visual observation on core plugs is applied to examine if there are fractures developed in a sample. For the 39 samples that are classified as fractured core plug based on porosity-permeability relation method, core observation indicates that 37 samples of them contain fractures. Therefore, there is a high agreement between porosity-permeability method and observation method.

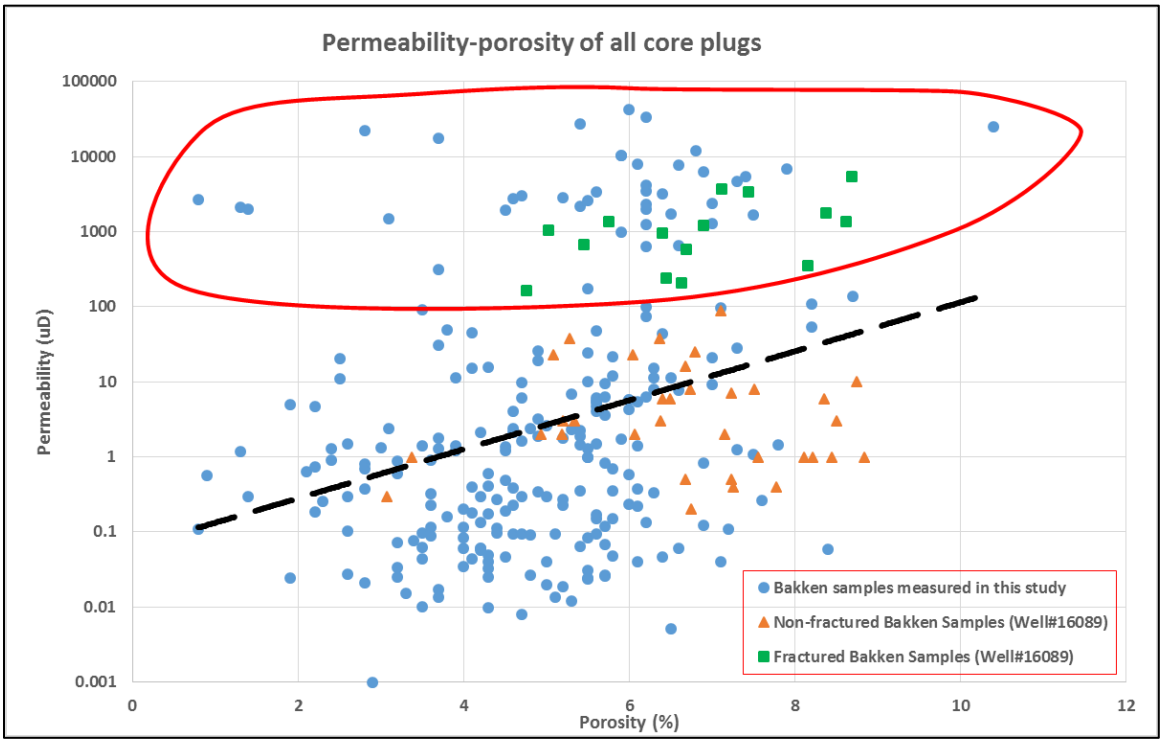

Figure 4.8 Porosity-permeability of Bakken cores measured in this study and measured by Corelab (Well#16089)

To further verify the proposed method, we overlapped other Bakken core data on Figure 4.5 as shown in Figure 4.8. These Bakken cores from well# 16089 (NDIC file name) were analyzed by Corelab (Samson Resources Company, 2006). In core analysis, porosity and permeability were measured; and the cores with fracture were identified through observation. As shown in Figure 4.8, there are 39 cores from well# 16089 of

which 15 cores (green data) locate inside the fractured core zone. Corelab's report denotes that these 15 samples contain fractures or are chipped sample. The other 24 samples (brown data points) lie in non-fracture core zone. No fracture was observed in these 24 samples according to Corelab's report. Therefore, the identification of fracture through the proposed model is reliable.

The developed method identifies fractures based on the permeability test under unsteady-state flow. Since it relies on permeability test data only, it does not require additional cost and equipment to conduct the test to generate images by imaging methods. The proposed method provides a practical, simple, and very low cost way to identify and characterize fractures in tight rocks. It can work as an important supplement to imaging methods for unconventional reservoirs

4.2.3. Comparison of Three Permeability Methods

The oscillating method with the AutLab-1500 system performs sensitivity studies to provide a means of computing errors associated with the insensitivity of the solution to the separation of permeability and specific storage. However, the data analysis technique is not shared by New England Research Inc.

To validate the permeability from the oscillating method, the permeabilities of six Bakken core plugs were measured using the oscillating pulse method, the downstream pressure build-up method, and the radius-of-investigation method. The pressure-time graphs are shown in Figure 3.9, Figure B.1, and Figures D.1 through D.10.

Table 4.5 Main parameters and permeability results from three methods on Bakken core plugs

	unit	Core 1	Core 2	Core 3	Core 4	Core 5	Core 6
L	in	2.7780	2.7224	2.7008	2.3882	2.6992	2.5819
D	in	1.0311	1.0394	1.0327	1.0323	1.0291	1.0315
ϕ	fraction	0.044	0.045	0.032	0.035	0.036	0.054
c_s	1/psi	0.000009	0.000009	0.000009	0.000009	0.000009	0.000009
c_g	1/psi	0.000125	0.000125	0.000125	0.000125	0.000125	0.000125
c_t	1/psi	0.000134	0.000134	0.000134	0.000134	0.000134	0.000134
μ	cp	0.0293	0.0293	0.0293	0.0293	0.0293	0.0293
V_2	ft^3	2.22E-05	2.22E-05	2.22E-05	2.22E-05	2.22E-05	2.22E-05
s	$Ln(psi^2)$ /h	-2.781108	-1.3644	-1.818	-1.2528	-2.4228	-78.12
μ	cp	0.0293	0.0293	0.0293	0.0293	0.0293	0.0293
t	h	0.0694	0.28	0.13889	0.14167	0.05556	0.0035
k (buildup)	µD	0.1864	0.09	0.1164	0.0791	0.158	5.2731
k (radius-of-investigation)	µD	0.2527	0.0615	0.0868	0.0728	0.2438	5.3546
k (oscillating pulse)	µD	0.108	0.046	0.0724	0.0438	0.11	2.25

The parameters that were used in the tests and experiment results are shown in Table 4.5. The permeabilities from the downstream pressure build-up method and the radius-of-investigation method are close to those from the oscillating pulse method (Figure 4.9). Therefore, the downstream pressure build-up method and the radius-of-investigation method provide the same order of magnitude of permeability as the oscillating pulse method for tight rocks. This indicates that the uncertainty has been reduced materially. Figure 3.9 shows that the measured time of the

radius-of-investigation method (ends at point “B”) requires less time than the oscillating pulse method (ends at point “C”).

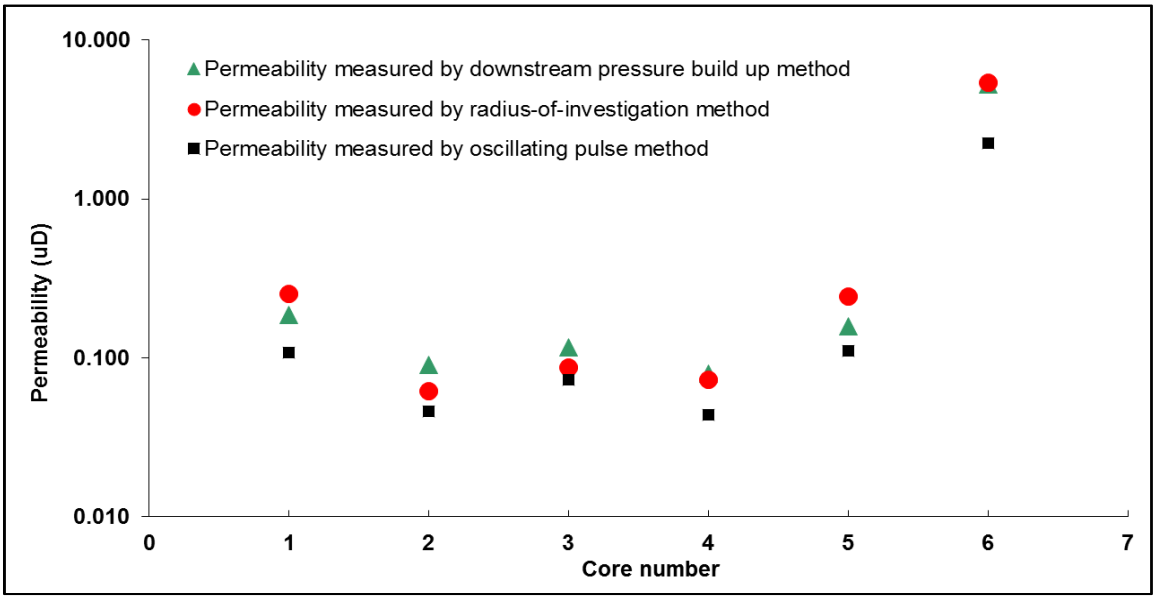

Figure 4.9 Comparison of permeabilities as measured by the three methods

The pressure build-up method, which is based on the pulse-decay method, is the transformation of a mature technique to measure the low permeability. Our study managed to reduce the downstream reservoir volume as much as possible in order to reduce the operation time. It requires less time than the oscillating pulse method and is a faster alternative to the steady-state, commonly accepted method. It is worth mentioning that to reduce the uncertainty during this procedure, the data that is chosen to calculate the slope (*s*) should be part of the data between point “B” and “A” with high signal-to-noise ratio (Figure 3.9). Because selecting the whole curve to fit will increase slope (*s*), or using the earlier data to fit will significantly reduce slope (*s*) (Figure A.1), middle data with high signal-to-noise ratio should be selected (Figure 4.10). Doing so

ensures the consistency of the calculation of the slope s and reduces the uncertainty in the obtained permeability.

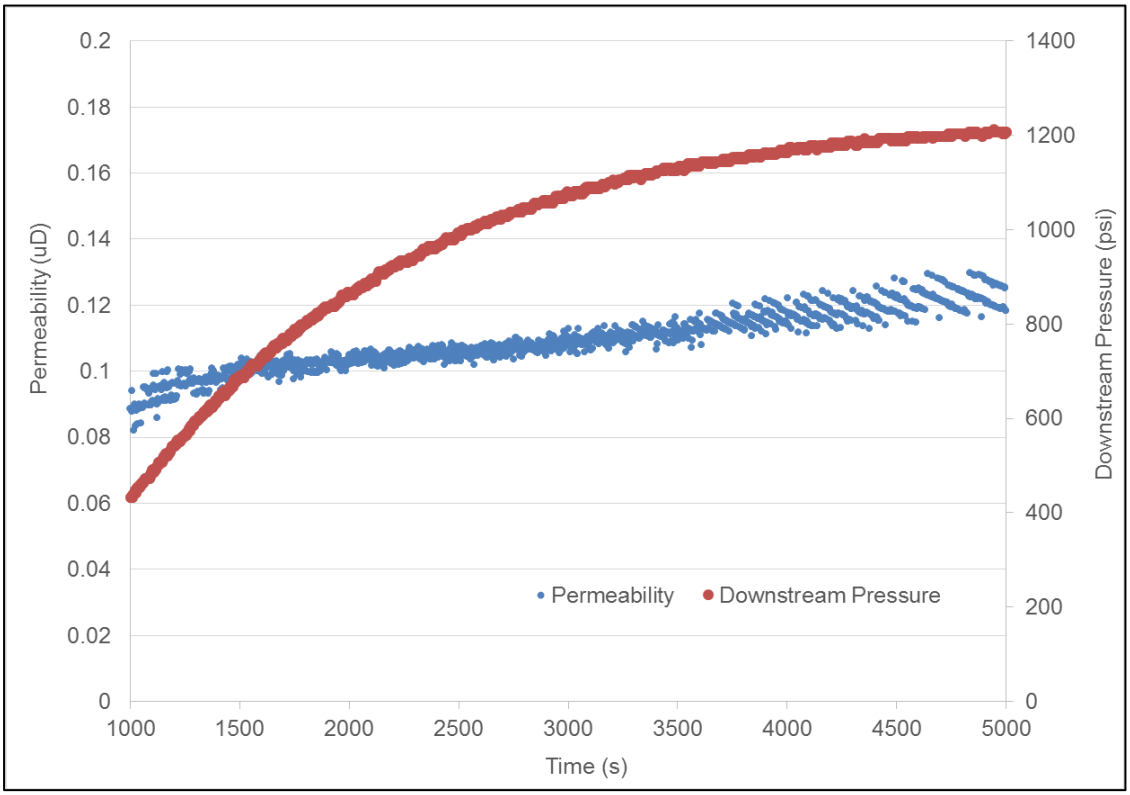

Figure 4.10 Downstream pressure during build-up and the calculated permeability for Core #1

For these tests, the permeability range of Core #1 (Figure 4.10) was checked after calculating the compressibility and viscosity of the gas as response variables depending on the pore pressure. The data in measurement time from 1500 s to 3500 s give a reliable permeability because of high signal-to-noise ratio. Permeability in this time interval ranges from 0.1 to 0.12 µD. Therefore, the average value of permeability is acceptable.

The radius-of-investigation method requires the least amount of the time to perform and results in reliable data. It utilizes the propagation speed of the pressure wave in a

certain media to calculate the permeability. This method provided a fast measurement of the low permeability. The measurement time for this method is 10 times less than the downstream pressure build-up method in this study. The radius-of-investigation method not only can be used to measure low permeability, but also can be used to measure high permeability by replacing the gas fluid with a liquid fluid. Other than the human introduced random error, the major uncertainty source in this method is mainly from the selection of point "B". To reduce the uncertainty, the beginning of the responding time (or point "B") is manually selected. It is easy to identify the starting point of downstream pressure build-up, which is point "B", through amplifying the short time interval as shown in Figure 3.9.

After we compared our results with those of Bertoncello's investigation (2013), the permeabilities from these three methods are close. This increases the confidence level. Therefore, the comparative measurement and analysis has value by providing fast and inexpensive measurements and can help quantify uncertainties.

In theory, the pore pressure differences in the three methods can cause the permeability difference because high pore pressure leads to a larger pore volume and thus a higher permeability. However, the results show that the lowest permeability is determined by oscillating pulse method, which is under the highest pore pressure. The reason is that the oscillating pulse method is proffered by AutLab-1500 system which considers the storage of the sample; this implies that the porosity of the samples is a variable in this method,

and the porosity decreases with the effective pressure increase. However, for the other two methods, in this study we assume that the value of porosity is constant. It is equal to the one measured at 1 atm. In fact with effective pressure increase, porosity will be reduced; thus, with a large porosity value, the permeability calculated by the other two methods is greater than the actual permeability.

If the results from these three methods are not close, it will not always be the case that the confidence level is low. It may indicate that the rock has a non-uniform pore structure. The heterogeneity of rock and/or microcracks may be the main causes. Considering the high pore pressure in the oscillating pulse and downstream pressure buildup methods and low pore pressure in the radius-of-investigation method, the heterogeneity and lamination of rock can be identified by the change of the permeability difference between the oscillating pulse and downstream pressure buildup methods and the radius-of-investigation method. The contribution of highly permeable parts of the rock becomes more important in the oscillating pulse and downstream pressure buildup methods than in the radius-of-investigation method as pore pressure increases. If microcracks exist in the rock, the permeability difference between the oscillating pulse and downstream pressure buildup methods and the radius-of-investigation method is higher than those caused by heterogeneity and lamination because the increase in the microcrack permeability is more significant than that in matrix permeability when pore pressure increases. It should be noted that heterogeneity and lamination can be coupled

with microcracks in many rocks, and make the decoupling of the effects of heterogeneity and lamination from microcracks very difficult. Therefore, further work needs to be done to quantify or identify the causes of differences through advanced imaging technology.

4.2.4. Investigation of Pore Pressure Impact

Many researches proved that permeability is reduced when the confining pressure is increased, depending upon the result of studying the effect of confining pressure on the permeability of porous media (Fatt, 1952 and 1953, mclatchie 1958, Dobrynin 1962, Zoback 1975). Although it is in general known that permeability declines as effective stress is increased, none of the correlations between permeability and effective stress can be used for all situations at the present time. Normally the change of effective stress is caused by the pore pressure decrease due to the depletion of reservoir during the production, and it is most difficult to measure Biot's coefficient for low permeability rocks, such as Bakken shale (He and Ling, 2014). Thus, a permeability-pore pressure correlation developed from experimental data is still needed.

With the aim of identifying the effect of pore pressure on permeability of Bakken samples, we have measured the permeability for 46 Bakken core plugs with Oscillating Pulse Method under different conditions in the range of 20-40 MPa and 3.5-7.5 MPa for the confining pressure and pore pressure, respectively. The confining pressure was maintained constant as changing the pore pressure, in order to correlate the applied pore pressure with the permeability and vice versa. The permeability measured in different

pressure conditions are shown in Figure 4.11.

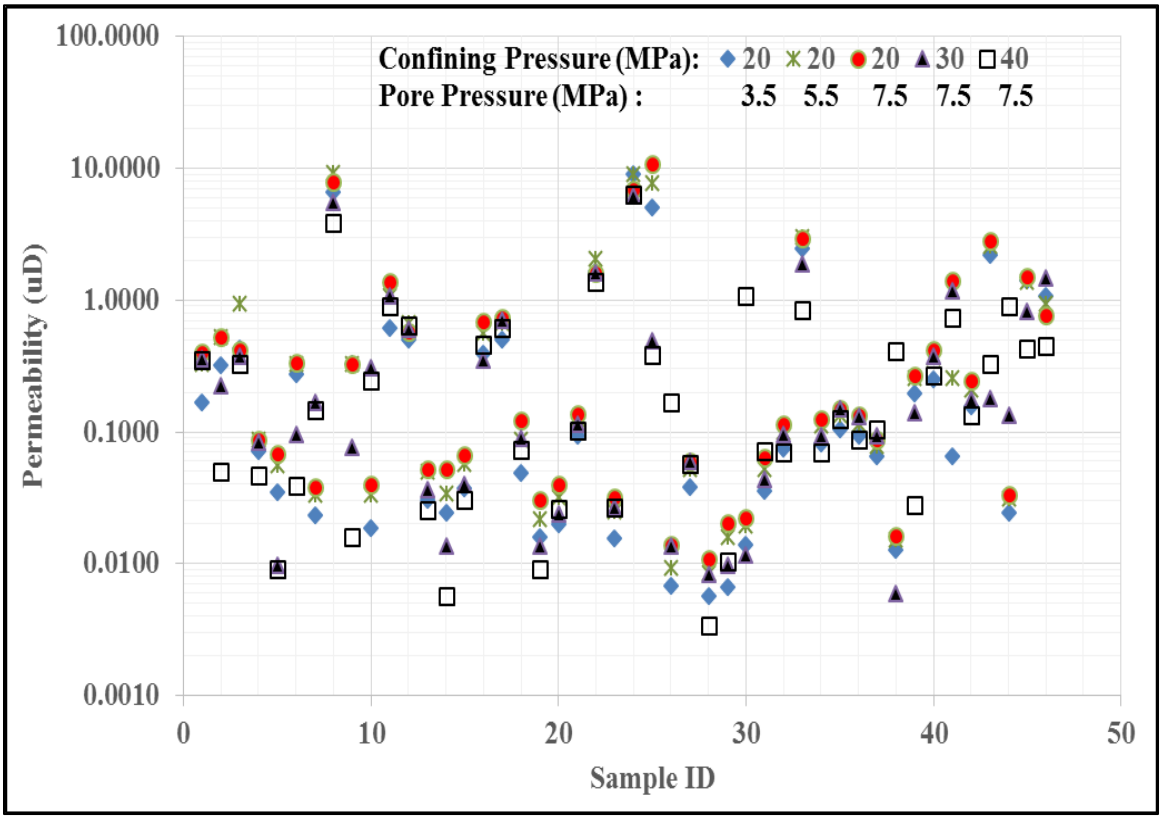

Figure.4.11 Permeability of 46 Bakken samples measured under different pressure Conditions

Figures 4.12, 4.13, 4.14, 4.15, and 4.16 are the distribution from of the permeability tests under different pressure saturations with the 46 Bakken samples. Those Figures clearly show that:

1) The most common permeability (80%) ranges from 0.001 µD to 1 µD.
2) The permeability increase as pore pressure increase. For instance, the percentage of samples whose permeability are great than 1µD is increase from 17% to 18% and 20%, as pore pressure increase from 3.5 MPa to 5.5 MPa and 7.5 MPa.
3) The permeability decrease as confining pressure increase. For instance, the

percentage of samples whose permeability are great than 1μD is decrease from 20% to 15% and 9%, as confining pressure increase from 20 MPa to 30 MPa and 40 MPa.

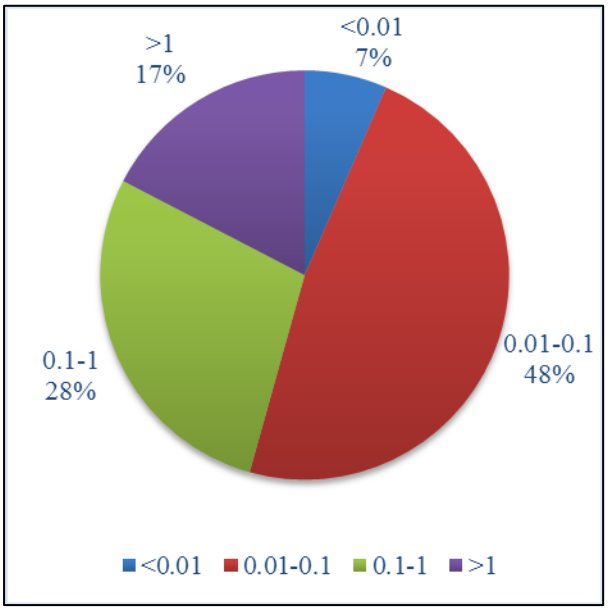

Figure 4.12 Permeability distribution (Confining pressure =20MPa, pore pressure = 3.5 MPa).

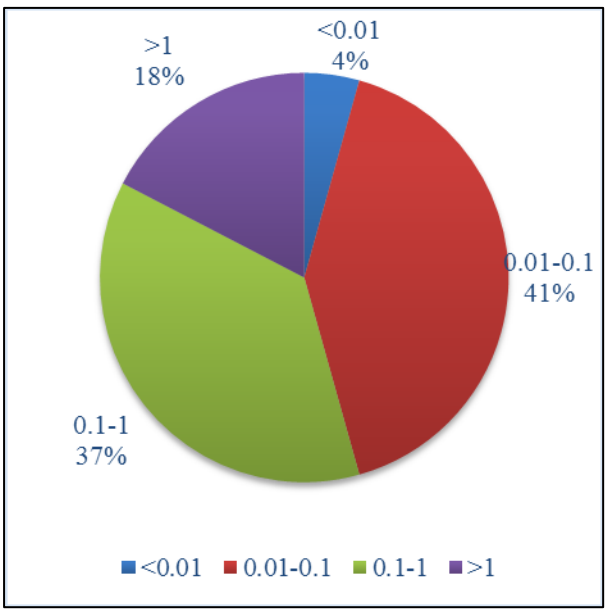

Figure 4.13 Permeability distribution (Confining pressure =20MPa, pore pressure = 5.5 MPa).

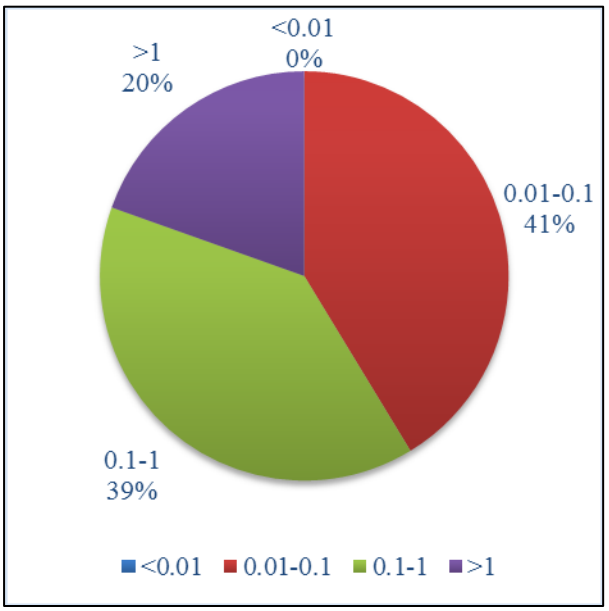

Figure 4.14 Permeability distribution (Confining pressure =20MPa, pore pressure = 7.5 MPa).

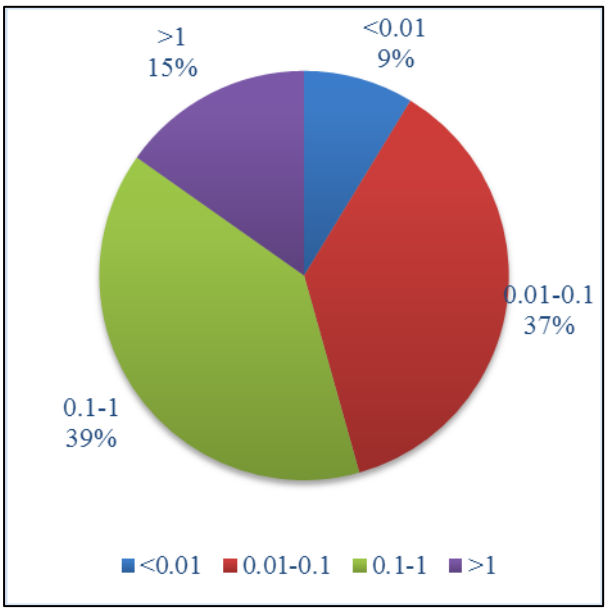

Figure 4.15 Permeability distribution (Confining pressure =30MPa, pore pressure = 7.5 MPa).

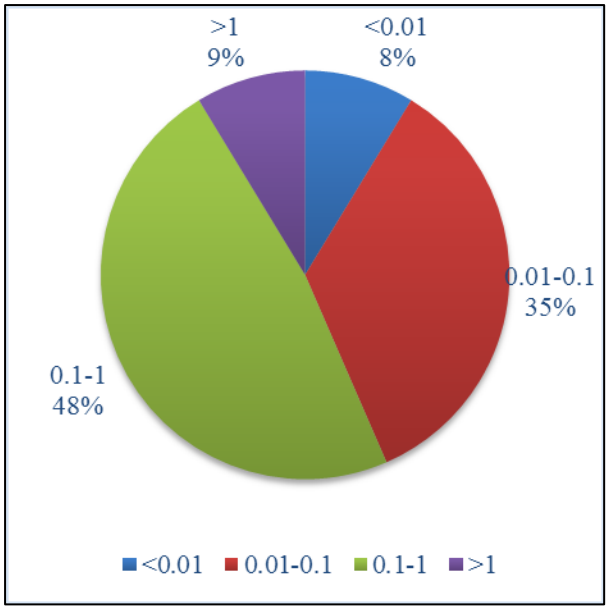

Figure 4.16 Permeability distribution (Confining pressure =40MPa, pore pressure = 7.5 MPa).

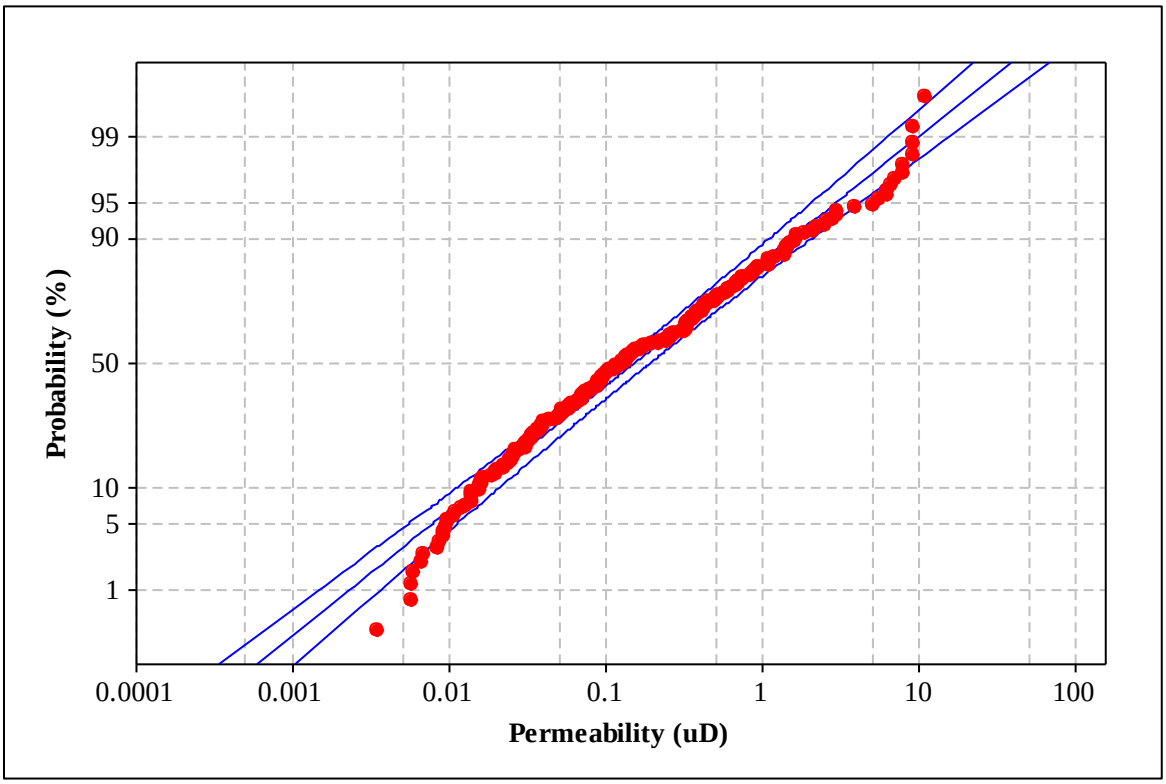

Figure 4.17 Permeability log-normal probability plot.

The measured permeability of Bakken samples fit to a lognormal distribution. This is

proved by the close fit of the data to a straight line as shown in Figure 4.17.

Table 4.6 contains the statistics of measured permeability with lognormal distribution. Those statistics strongly support that:

1) There is a proportional relationship between permeability and pore pressure. The evidence is that with a constant confining pressure as 20 MPa, the mean value of permeability increases from 0.122 μD to 0.175 μD and 0.199 μD when the pore pressure increased from 3.5 MPa to 5.5 MPa and 7.5 MPa, respectively. Moreover, the 95% confidence intervals for those three different pore pressure conditions are from 0.069 to 0.216 μD, 0.101 to 0.303 μD, and 0.117 to 0.337 μD, respectively.
2) Permeability is inversely proportional to confining pressure. With a constant pore pressure as 7.5 MPa, the mean value of permeability is decreases from 0.199 μD to 0.136 μD and 0.133 μD when the confining pressure increased from 20 MPa to 30Mpa and 40MPa, respectively. And the 95% confidence intervals for those three different confining pressure conditions are from 0.117 to 0.337 μD, 0.081 to 0.228 μD, and 0.080 to 0.221 μD, respectively.

Table 4.6 Statistics analysis of permeability of Bakken samples

Pore Pressure	Confining Pressure	Permeability (μD)					
(MPa)	(MPa)	Mean	Variance	Min	Max	95% Confidence Interval	
3.5	20	0.122	4.920	0.006	9.036	0.069	0.216
5.5	20	0.175	4.426	0.009	9.120	0.101	0.303
7.5	20	0.199	3.954	0.011	10.765	0.117	0.337
7.5	30	0.136	3.715	0.006	6.152	0.081	0.228
7.5	40	0.133	3.581	0.003	6.281	0.080	0.221

To develop the relation between the permeability and both of pore pressure and confining pressure, the mean values of permeability are used to regress. One regression equation is given as:

$$k = 0.1443 - 0.0036 p_c + 0.0163 p_p \quad (4.19)$$

and the R^2 of this regression equation is 0.8.

Equation (4.19) shows that permeability (K) will be reduced when the confining pressure (p_c) is increased, and the reduction factor from the confining pressure is 0.0036; on the other hand, permeability will be increased with the pore pressure increase, and the increment factor for the pore pressure is 0.0163. Thus, the pore pressure has a greater influence on permeability than the confining pressure has.

4.3. Elastic Moduli

4.3.1. Experiment Result

The test results for the static and dynamic elastic moduli are shown in Table 4.7, 4.8, 4.9 and Table 4.10. The static Young's modulus averages 74.05 GPa with a relatively higher standard deviation. The dynamic Young's modulus has a mean value as 57.61 GPa with a lower standard deviation. Because the Poisson's ratios from both static and dynamic tests almost have the same value 0.21, at the following discussion part, the comparison of static moduli and dynamic moduli was only for Young's modulus.

Table 4.7 Statistic result of static Young's modulus

Member of Bakken Formation	Total Numbers	Success Numbers	Young's Modulus (GPa)			Standard Deviation
			Min	Mean	Max	
Upper Bakken	42	33	41.62	78.22	172.30	27.32
Middle Bakken	140	125	30.60	70.11	653.00	56.48
Lower Bakken	58	51	32.76	81.02	219.23	39.91
Total	240	209	30.60	74.05	653.00	49.23

Table 4.8 Statistic result of Dynamic Young's modulus

Member of Bakken Formation	Total Numbers	Success Numbers	Young's Modulus (GPa)			Standard Deviation
			Min	Mean	Max	
Upper Bakken	42	40	43.26	61.87	89.26	8.71
Middle Bakken	140	132	40.05	55.95	71.52	5.98
Lower Bakken	58	52	40.62	58.55	81.01	9.31
Total	240	224	40.05	57.61	89.26	7.69

Table 4.9 Statistic result of static Poisson's ratio

Member of Bakken Formation	Total Numbers	Success Numbers	Poisson's Ratio			Standard Deviation
			Min	Mean	Max	
Upper Bakken	42	33	0.034	0.232	0.628	0.112
Middle Bakken	140	125	0.003	0.199	0.490	0.088
Lower Bakken	58	51	0.004	0.225	0.484	0.117
Total	240	209	0.003	0.211	0.628	0.101

Table 4.10 Statistic result of Dynamic Poisson's ratio

Member of Bakken Formation	Total Numbers	Success Numbers	Poisson's Ratio			Standard Deviation
			Min	Mean	Max	
Upper Bakken	42	40	0.170	0.240	0.320	0.041
Middle Bakken	140	132	0.056	0.206	0.310	0.040
Lower Bakken	58	52	0.032	0.221	0.349	0.051
Total	240	224	0.032	0.215	0.349	0.045

4.3.2. Velocity Correlation between P-wave and S-wave

A linear relationship, Equation (4.20), was found between the velocities of P- and S-waves (Figure 4.18). The relatively higher regression coefficient ($R^2 = 0.7$) reveals that a strong correlation exists between the two velocities. In the oil industry, obtaining V_p

from seismic data is cheaper and easier than getting V_s, so with Equation (4.20), V_s can be estimated from V_p.

$$V_s=0.3015V_p + 1464.8 \quad (4.20)$$

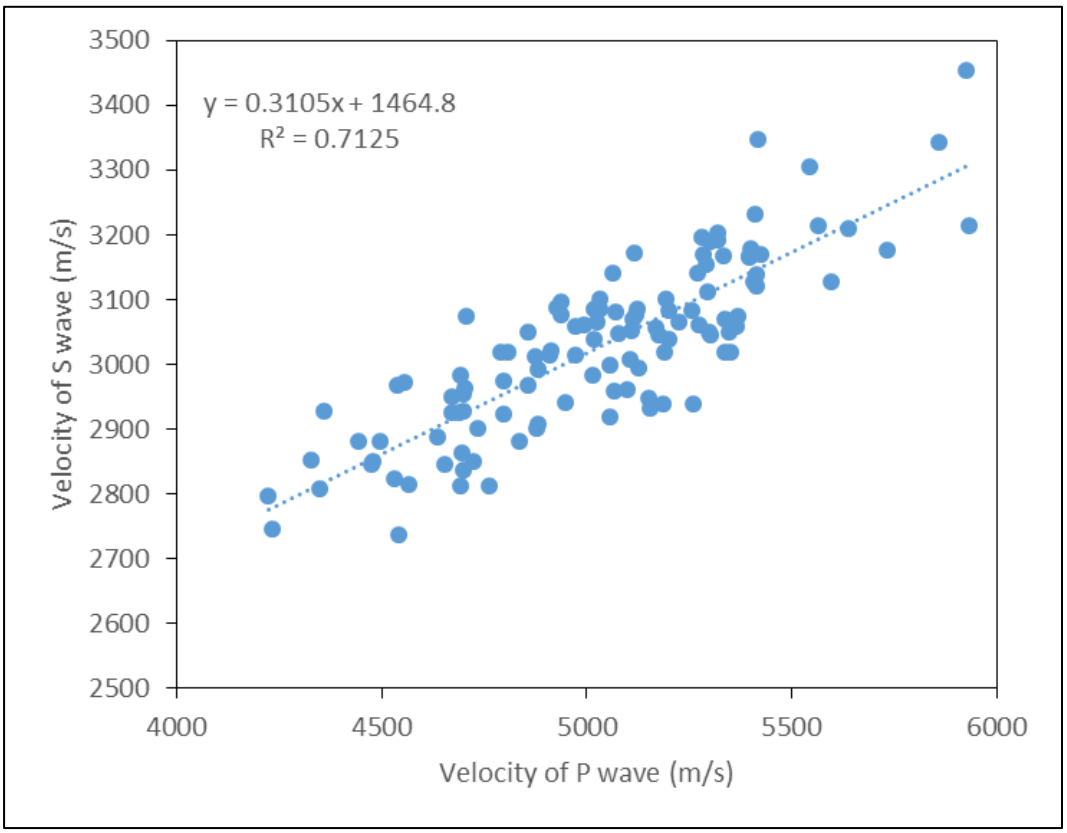

Figure 4.18 Correlation between V_s and V_p

4.3.3. Comparison of Dynamic Moduli and Static Moduli

By definition, dynamic moduli and Poisson's ratio are calculated from the elastic wave velocity and density. They are different from static dynamic moduli and Poisson's ratio moduli, which are directly measured in a deformational experiment. The static and dynamic moduli of the same rock may significantly differ from each other. The main reason is likely to be the difference in the deformation, or strain, amplitude between the

dynamic and static experiments. Predicting static moduli from dynamic moduli is meaningful because measuring static moduli is more difficult than determining dynamic moduli.

Ide (1936) pointed out that the dynamic moduli of rock are different from the static moduli because the equations to calculate the dynamic moduli are derived based on the assumption that the rock is homogeneous, isotropic and perfectly elastic. Unfortunately, most rocks cannot satisfy such an assumption. The author also indicted that the values of the dynamic moduli are higher than those of the static moduli for the fine-grained, igneous rocks. Mavko (2009) compiled a series of linear functions to calculate the static moduli from the dynamic moduli for different rocks, such as for microcline-granite by Belikov, for igneous and metamorphic rocks from the Canadian Shield by King, for Granites and Jurassic sediments in the UK by McCann and Entwisle, for clay, sandy, and wet soil by Gorjainov and Ljachowickij, and for soft and hard rocks by Wang and Nur. Hilbert (1994) studied the nonlinear static and dynamic properties of Berea sandstone. Canady (2011) introduced a non-linear function to model the correction for elastic moduli.

Fjaer (2008) pointed out that the equations of calculating dynamic moduli from the P- and S- wave velocities are derived through elastic wave propagation, Newton's second law of motion, and the Hooke's law. Usually, Newton's second law of motion is always applicable. Thus, the correlation between dynamic and static moduli is controlled by the

adaptiveness of elastic wave propagation and the Hooke's law.

Hilbert (1994) investigated the influence of elastic wave propagation to the static and dynamic non-linear behavior. The experimental results and analyses show that nonlinear static and dynamic properties of Berea sandstone are due to the strain amplitude of the loading, and dynamic moduli match static moduli in small-strain, small-stress amplitude cycles. By studying the Castlegate sandstone, Plona (1995) also found that the difference between the static and dynamic moduli is negligible when the experiments are in small load-unload cycles, and recommended that the comparison of static and dynamic moduli should be avoided in the first major load-unload cycle in which the significant difference exists because of hysteresis.

However, most researchers focused on the factors that made the conditions violate Hook's law. Canady (2011) summarized the behavior of acoustic velocities in four regimes of formation consolidation, including unconsolidated formations, and three consolidated formations which are hetrogenuous, linear, and non-linear regimes. The linear regime only exists in the consolidated formations in which Hooke's law is valid.

Because of the complexity of the correction between the static and dynamic moduli, there is no general empirical equation to estimate the static moduli from the dynamic moduli. In this study, by comparing the dynamic and static moduli obtained in lab with the samples taken from Bakken Formation of Williston Basin, we found that the dynamic moduli of Bakken samples are considerably different from the static moduli. Three

empirical correlations are developed to estimate the static moduli from the dynamic moduli.

These correlations can be employed to adjust the uncertainty of elastic moduli calculated from the seismic and well-log data for Bakken Formation and to lower the expensive cost and test time on conducting static tests. These correlations are of importance in investigating reservoir properties where no core sample is available for direct measurement of elastic moduli.

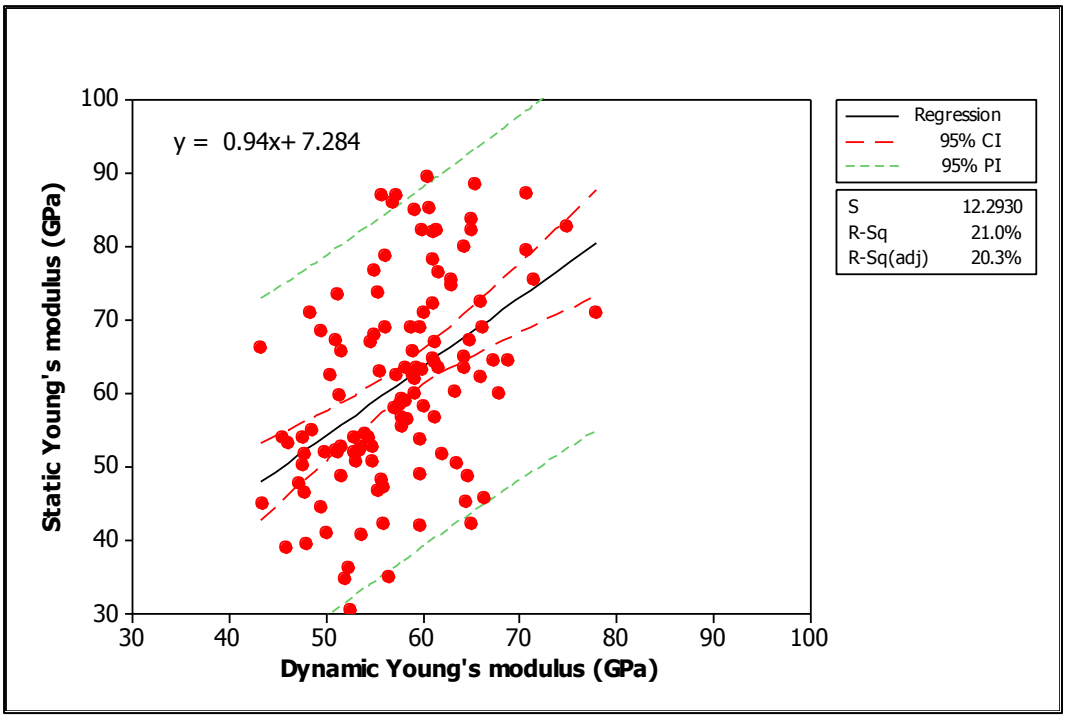

Figure 4.19 Correlation between static and dynamic moduli (All Bakken Samples)

To compare the static and dynamic moduli, 117 Bakken samples have been studied, among which 89 were from the middle Bakken, and 28 were from the upper and lower Bakken. From the results of these Bakken samples (see Figure 4.19), the empirical

equation developed to calculate static moduli from dynamic moduli is:

$$E_{static} = 0.94E_{dynamic} + 7.284 \quad (4.21)$$

After comparing the static moduli to the dynamic moduli in Figure 4.19, we found that the difference exists between both moduli. The range of dynamic moduli is from 40 to 80 GPa, and the range of static moduli is much wider, from 30 to 90 GPa. However, the average values are about 60 GPa for both static and dynamic moduli (Table 4.11). Moreover, for some samples the dynamic moduli are greater than the static moduli, but for other samples, they are not.

Table 4.11 Statistic results of comparison of static and dynamic Young's moduli

Member of Bakken	Number	Porosity	Clay Content	Young's Modulus		Empirical equation
				Static	Dynamic	
		%	%	GPa	GPa	
Upper Lower	28	5.052	44.523	65.065	59.065	$E_{static} = 0.7327E_{dynamic} + 21.79$
Middle	89	4.959	7.583	60.279	57.137	$E_{static} = 0.9501E_{dynamic} + 6.0$
Total	117	4.981	16.423	61.424	57.598	$E_{static} = 0.94E_{dynamic} + 7.284$

Fjaer (2008) indicated that the elastic response of a rock may be affected by the pore fluid which is strongly related to the porosity of the rock. In this study, porosity cannot be the cause of the difference of the static and dynamic moduli because the porosities are small and in the same range for all samples (Table 4.11).

Sone and Zoback (2013) indicated that elastic properties are a function of material composition. They found that the shale elastic properties are a strong function of

composition and fabric anisotropy. Those anisotropies of shale were caused by clay and organic content. According to the lithology of the Bakken Formation, the upper and lower Bakken members are shale, containing a large amount of clay and organic contents. This could be a reason to cause the difference. After separating the samples to the middle and upper-lower members, and getting the clay content of the samples from gamma ray well-log (see Table 4.11), we see that the samples of the upper-lower member have greater clay content. Comparing Figures 4.20 and 4.21, there is no big difference in the static moduli between the middle Bakken and the upper-lower Bakken, but the range of the dynamic moduli of the upper-lower Bakken (50~70GPa) is narrower than that of the middle Bakken (40~80GPa). Thus clay content will influence the correlation of static-dynamic moduli.

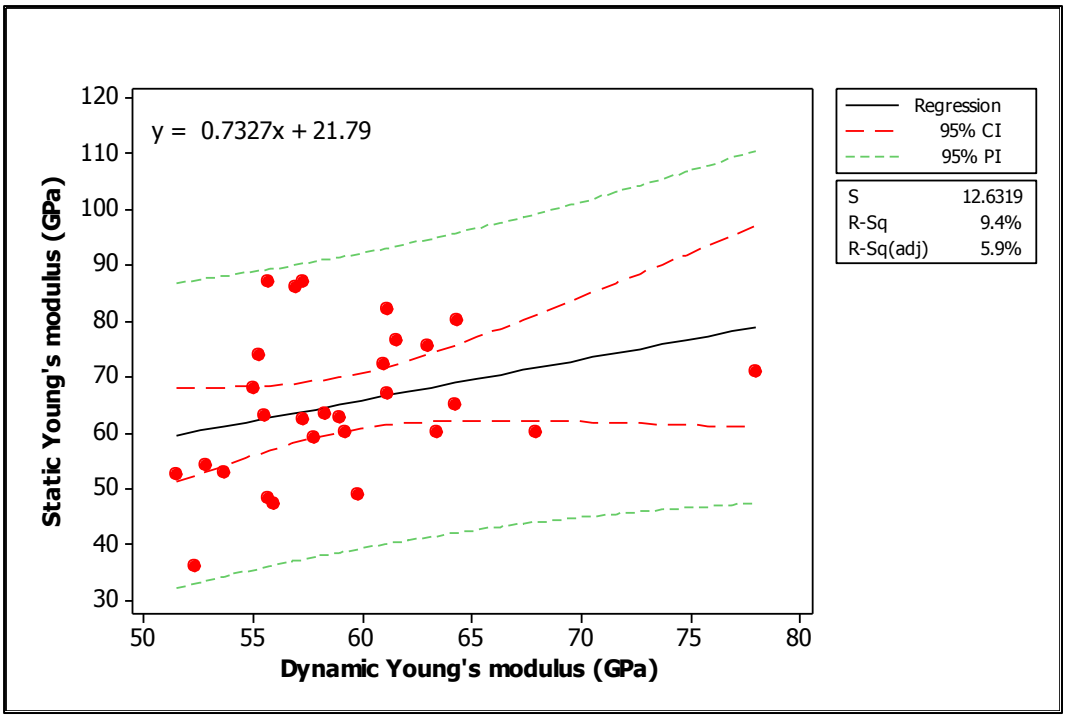

Figure 4.20 Correlation between static and dynamic moduli (Upper and Lower Bakken

Samples)

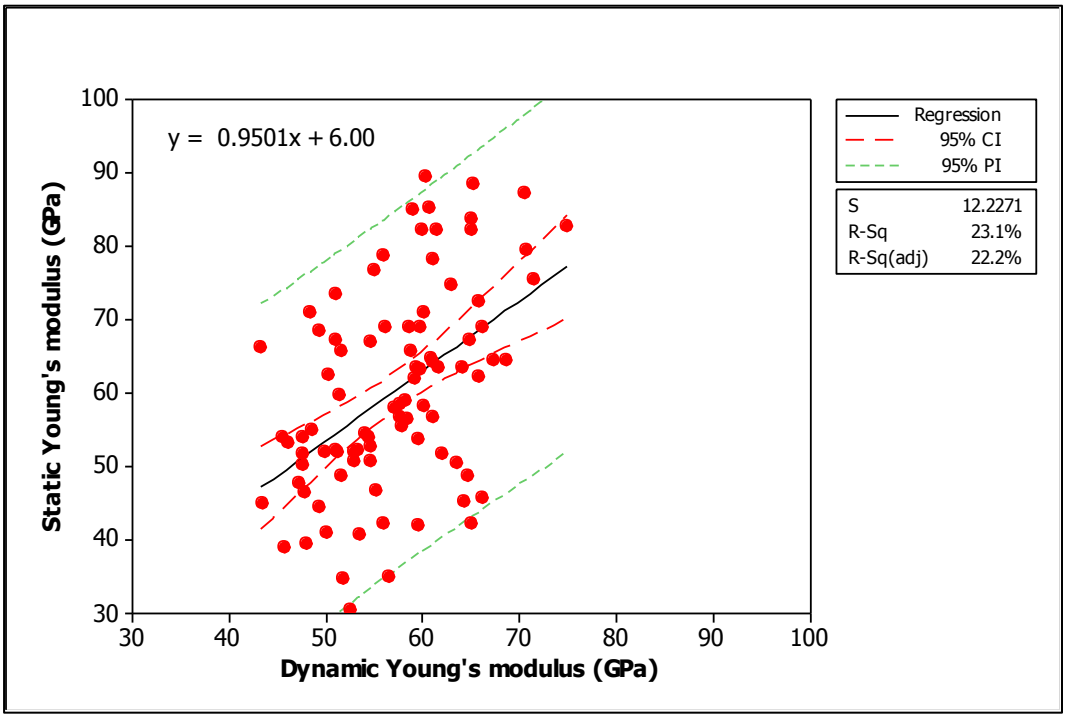

Figure 4.21 Correlation between static and dynamic moduli (Middle Bakken Samples)

When considering the permeability, we found that when permeability is low, less than 1μD, the static and dynamic moduli almost have the same value; when permeability is in the middle, between 1μD and 100μD, the static moduli are greater than dynamic one; and when permeability is high, greater than 100μD, the static moduli are less than dynamic one (see Figure 4.22). Because the porosity is in the same range for all samples, the permeability must be influenced by the micro-fracture. In this case, the micro-fracture is one of the key reasons causing this difference. Figure 4.22 also shows that the static moduli are less than the dynamic moduli for soft samples with the lower Young's modules, and greater than the dynamic moduli for hard samples with higher Young's modulus.

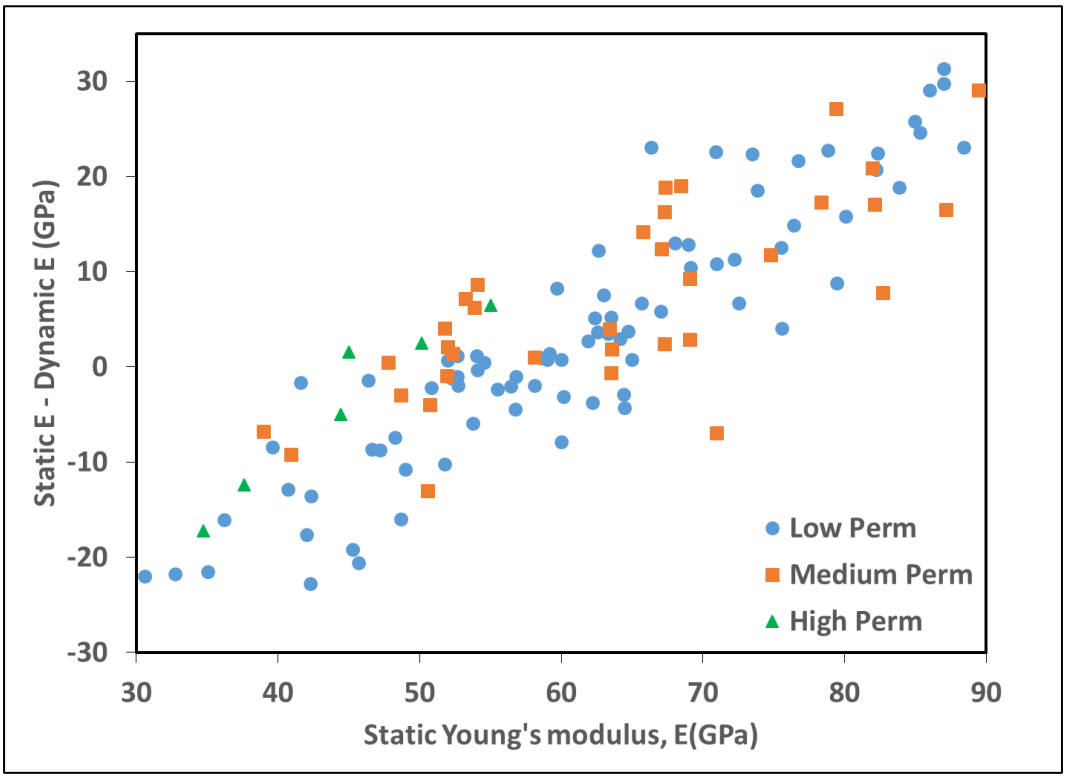

Figure 4.22 Influence of permeability on moduli relationship of static-dynamic

Wang and Nur (2000) proved that the correlations of static and dynamic Young's modulus are as follows for soft and hard rocks:

$E_{static} = 0.41E_{dynamic} - 1.06$ (Static Young's modulus < 15GPa)

$E_{static} = 1.153E_{dynamic} - 15.2$ (Static Young's modulus > 15GPa)

We observe that the dynamic moduli is greater than the static moduli for soft rocks and some hard rocks, for which the static Young's modulus is less than 100GPa approximately; and that the static moduli will be greater than the dynamic one when static Young's modulus is over 100GPa.

In this case, the critical value of static Young's modulus is around 60GPa for our study as

comparing to the value of 100GPa for the study of Wang and Nur (2000). As commented by Mashinsky (2003), the difference between the dynamic and static moduli of rock comes from the viscoelastic and micro-plastic behavior of the rock, and from the inelastic mechanisms. Thus when the rock is harder, the plastic behavior of the rock will be less, this should be the most important factor causing the Estatic and Edynamic difference for the Bakken samples.

4.4. Compressibility

We did a feasibility study for the proposed methods which use permeability experiment data to obtain rock compressibility. The lab measurements of 6 cores were used for verifying Downstream Pressure Build-up method (Table 4.12), and other 9 cores were measured for verifying Radius-of-Investigation method (Table 4.13). The measure procedure is exactly the same as the permeability experiment has.

After the compressibility was obtained from the permeability experiment, we compared the compressibility with the one which was measured directly with the triaxial stress experiment to evaluate the accuracy of the proposed methods. As shown in Figure 4.23, and 4.24 for Downstream Pressure Build-up method and Radius-of-Investigation method, respectively, the compressibilities from the proposed methods are close to those from triaxial stress experiments. Therefore the proposed methods provide a reliable way to determine rock compressibility.

Table 4.12 Compressibility calculated from pressure build-up model and measured from triaxial stress experiment

	unit	Core 1	Core 2	Core 3	Core 4	Core 5	Core 6
L	in	2.7780	2.7224	2.7008	2.3882	2.6992	2.5819
D	in	1.0311	1.0394	1.0327	1.0323	1.0291	1.0315
ϕ	%	4.4	4.5	3.2	3.5	3.6	5.4
c_g	Psi^{-1}	0.0022	0.00098	0.00103	0.00132	0.0022	0.00146
μ	cp	0.0246	0.0246	0.0246	0.0246	0.0246	0.0246
V_2	ft^3	2.22E-05	2.22E-05	2.22E-05	2.22E-05	2.22E-05	2.22E-05
s	$Ln(psi^2)/h$	-2.4588	-1.3644	-1.818	-1.2528	-2.4228	-78.12
k	µD	2.28	0.56	0.78	0.65	2.20	48.36
C_f (Proposed Method)	10^{-7}/psi	2.92	0.898	1.85	2.11	3.03	1.86
C_f (Triaxial Method)	10^{-7}/psi	2.704	1.069	1.694	1.994	3.33	1.57
Relative error	%	7.39	-19.04	8.43	5.50	-9.90	15.59

Table 4.13 Compressibility calculated from radius-of-investigation model and measured from triaxial stress experiment

	unit	Core 1	Core 2	Core 3	Core 4	Core 5	Core 6	Core 7	Core 8	Core 9
L	in.	2.02	2.06	2.03	2.01	2.04	2.02	2.03	2.05	2.04
t	hour	0.127	0.246	0.078	0.099	0.057	0.051	0.049	0.090	0.040
ϕ	%	5.7	4.2	7.3	6.4	8.4	8.7	9.3	6.8	10.4
k	µD	0.15	0.06	0.32	0.21	0.52	0.59	0.68	0.26	1.0
c_g	10^{-6}/psi	125	125	125	125	125	125	125	125	125
μ_g	cp	0.0474	0.0474	0.0474	0.0474	0.0474	0.0474	0.0474	0.0474	0.0474
C_f (Proposed Method)	10^{-6}/psi	6.1	5.3	8.4	6.3	11.5	11.2	15	8.1	22.3
C_f (Triaxial Method)	10^{-6}/psi	6.6	4.5	7.3	6.2	9.7	9.5	12.5	7.5	15.5
Relative error	%	-8.20	16.81	14.49	2.06	18.64	18.18	20.30	8.08	44.12

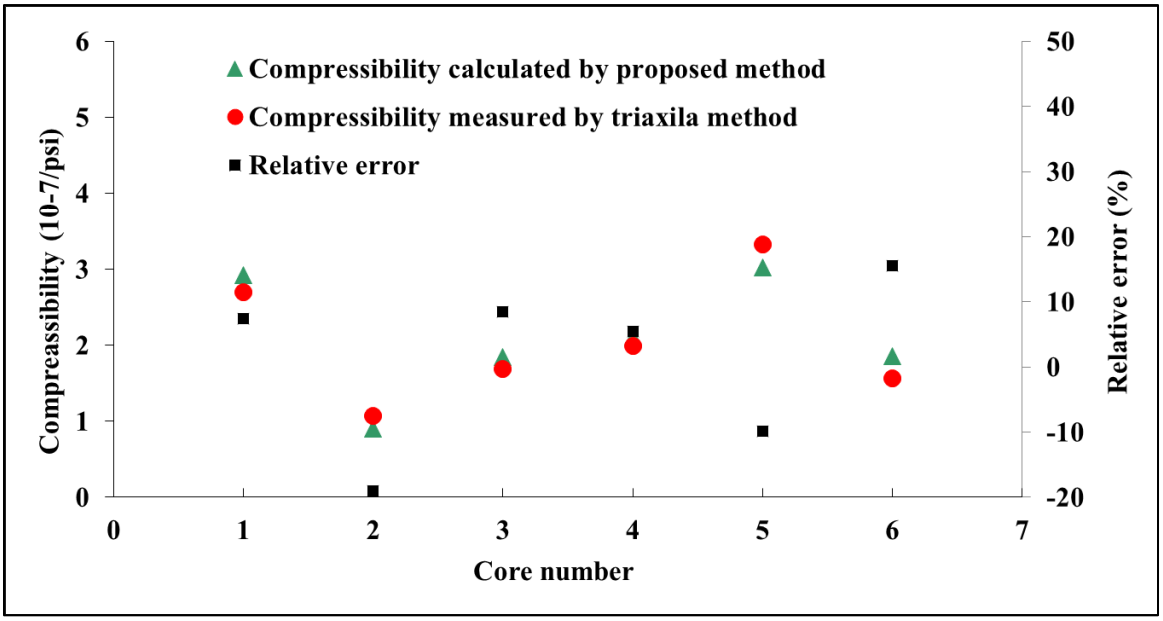

Figure 4.23 Comparison of compressibilities calculated by the proposed model (pressure build-up) and measured by triaxial stress experiment

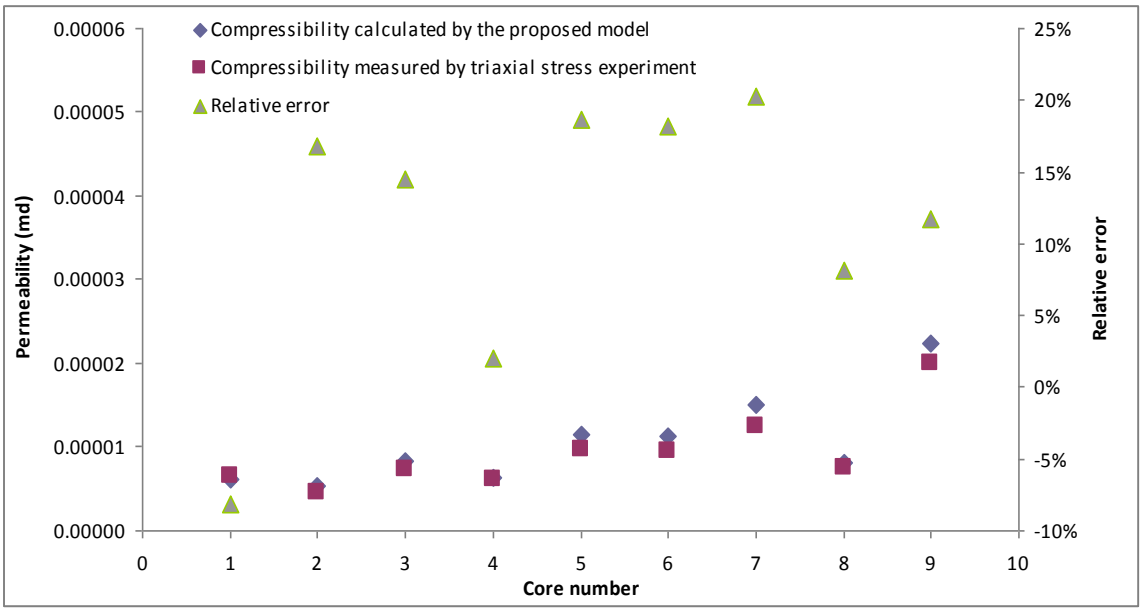

Figure 4.24 Comparison of compressibilities calculated by the proposed model (radius-of-investigation) and measured by triaxial stress experiment

The limitation of the Radius-of-Investigation method is the sensitivity of the pressure gauge needed to be high enough to detect small pressure change. The accuracy of this method depends on the accuracies of rock porosity, permeability, core length, and gas

compressibility. With a high resolution pressure gauge, a correct capture of pressure wave arrival can be guaranteed. A good estimation of gas viscosity and permeability at measured conditions is also important.

The cost to measure rock compressibility can be high and time consuming. The proposed model provides a way to estimate rock compressibility from permeability experimental data in case direct compressibility measurement is not available. In the event direct compressibility measurement is available, the model can serve as a quality control tool.

4.5. Biot's Coefficient Experimental Result

Table 4.14 shows the result of the Biot's coefficients for 27 Bakken samples using the proposed method, including 10 vertical direction samples (V-sample, taken perpendicular to the bedding) and 17 horizontal direction samples (H-sample, taken along the bedding plane).

Comparing the H-samples to the V-samples in Figure 4.25, we see that the average Biot's coefficient of H-sample (0.67) is larger than that of V-sample (0.61). According to Figures 4.25, 4.26, and 4.27, the Biot's coefficient of H-sample is higher than that of V-sample. This anisotropy of Biot's coefficient of Bakken rock indicates that the Bakken Formation is heterogeneous. The influence of the pore pressure to the in-situ stress is greater along the bedding plane than perpendicular to the bedding.

Table 4.14 Results of Biot's coefficient test

Sample ID	Permeability k : (μD)	Porosity ϕ: (%)	Direction	Biot's Coefficient
1	3.73	4.62	V	0.65
2	0.08	5.73	V	0.66
3	0.05	5.76	V	0.60
4	0.07	4.19	V	0.57
5	0.24	4.03	V	0.61
6	0.20	3.58	V	0.59
7	2.19	5.61	V	0.58
8	0.19	5.57	V	0.61
9	1.45	5.93	V	0.63
10	1.54	5.34	V	0.58
11	0.64	4.30	H	0.67
12	0.14	4.56	H	0.70
13	0.09	3.47	H	0.59
14	0.40	4.93	H	0.67
15	0.08	3.97	H	0.68
16	0.07	4.18	H	0.66
17	0.33	4.59	H	0.70
18	1.17	2.23	H	0.69
19	1.60	5.46	H	0.68
20	4.68	7.26	H	0.69
21	0.09	5.45	H	0.67
22	1.60	2.39	H	0.67
23	1.58	2.39	H	0.67
24	1.44	2.39	H	0.67
25	1.39	2.39	H	0.67
26	0.71	6.01	H	0.68
27	0.23	5.18	H	0.70

The Biot's coefficient is shown in Figure 4.26 as a function of permeability. The regression equations are:

H: $\alpha = 0.6774 + 0.01121 \times \log_{10}(k)$ (4.22)

V: $\alpha = 0.6099 + 0.00523 \cdot \log_{10}(k)$ (4.23)

Even though the values of R^2 are 6.1% and 1.4% for H-sample regression model and V-sample regression model, respectively. The Equation 4.22 and Equation 4.23 still reveal the relations between permeability and Biot's coefficient.

According to this study (see Figure 4.27), no relationship is found between Biot's coefficient and porosity for Bakken Formation.

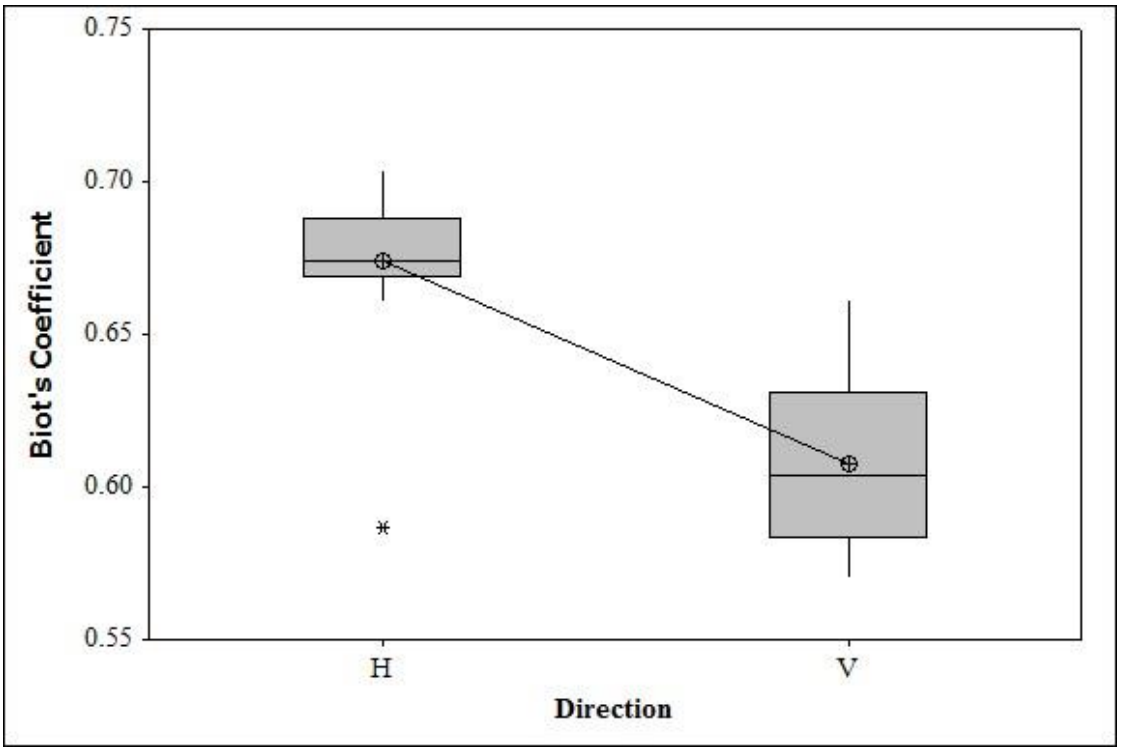

Figure 4.25 The BoxPlot of Biot's Coefficient with two groups (horizontal sample and vertical sample)

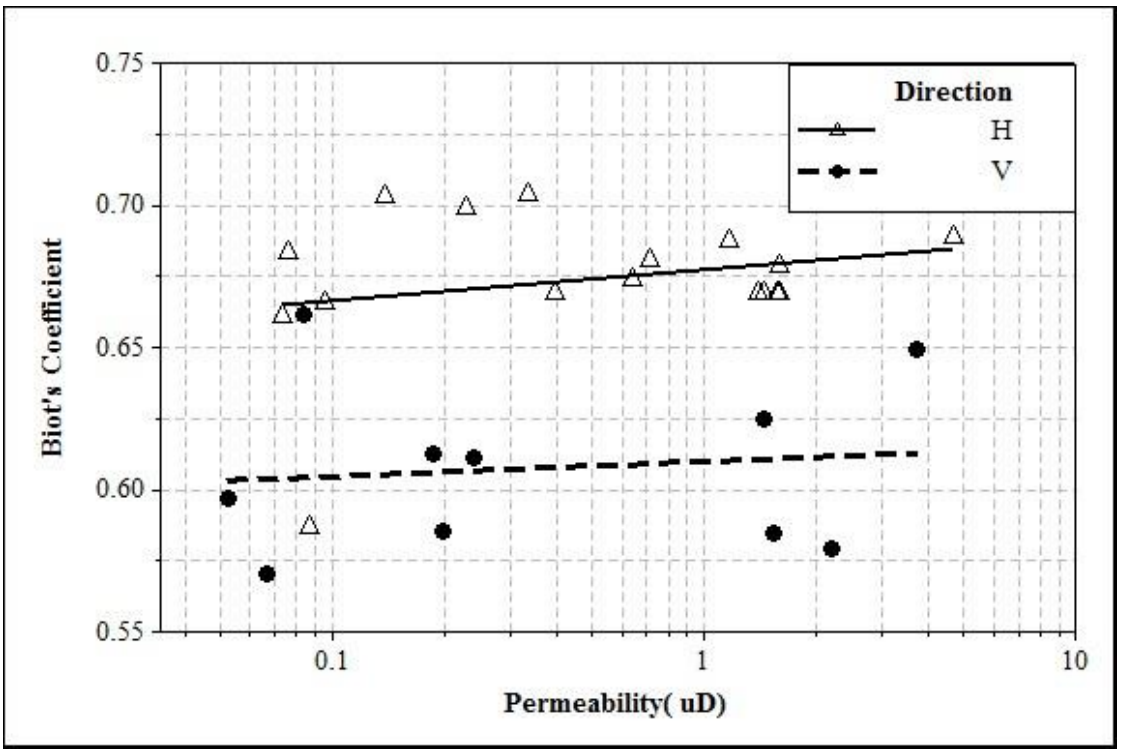

Figure 4.26 Biot's coefficient vs. Permeability

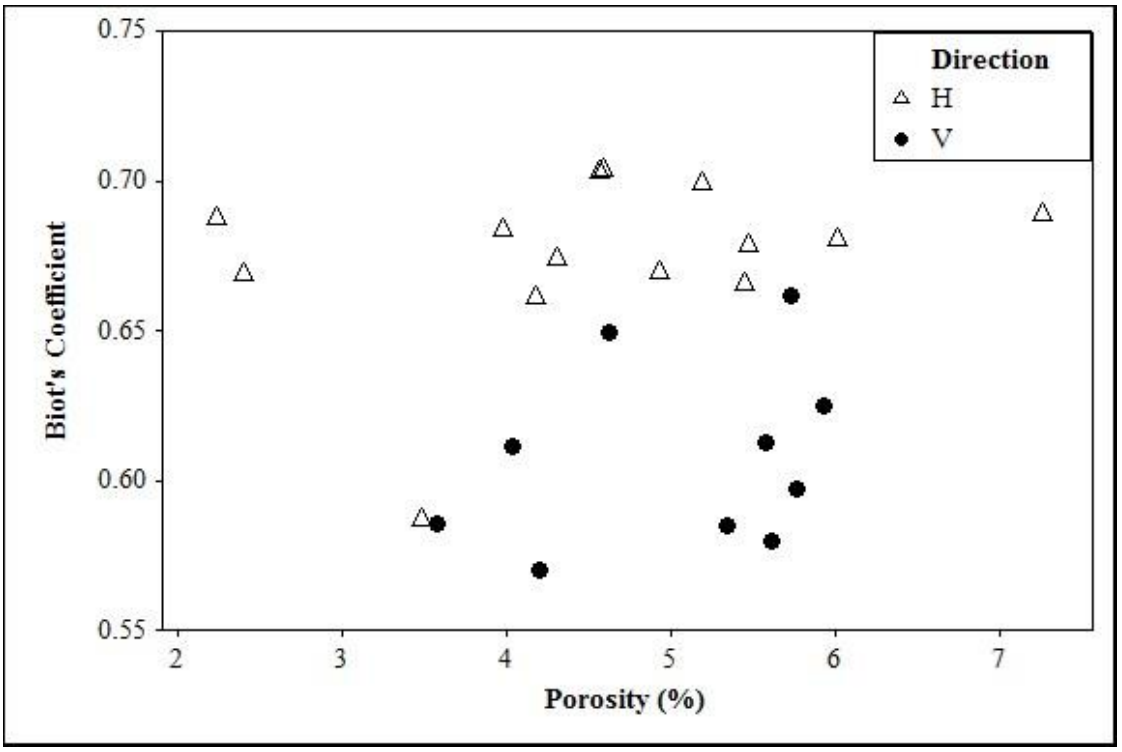

Figure 4.27 Biot's coefficient vs. Porosity

4.6. Compressive Strength Experimental Result

We have measured compressive strength for 104 Bakken core plugs from seven wells. For each individual test, the confining pressure was kept constant in a range from 0 to 20 MPa. Table 4.15 shows the mean compressive strengths at different confining pressures. The changes of compressive strength caused by confining pressure change are shown clearly in Figure 4.28.

Table 4.15 Compressive strength in different assessment unit, (MPa)

Assessment Unit	Map Number	Confining Pressure (MPa)				
		0	5	10	15	20
Nesson-Little Knife Structural AU	2	133.37		145.03		136.37
	96	115.82		120.43		190.17
Central Basin-Poplar Dome AU	13	131.80		166.10		233.55
Northwest Expulsion Threshold AU	18	105.80		164.10	181.90	
	86	101.91	118.87	145.18	169.93	
Elm Coulee-Billings Nose AU	20	130.46		149.52		156.36
Eastern Expulsion Threshold AU	70	135.91		161.36		165.94

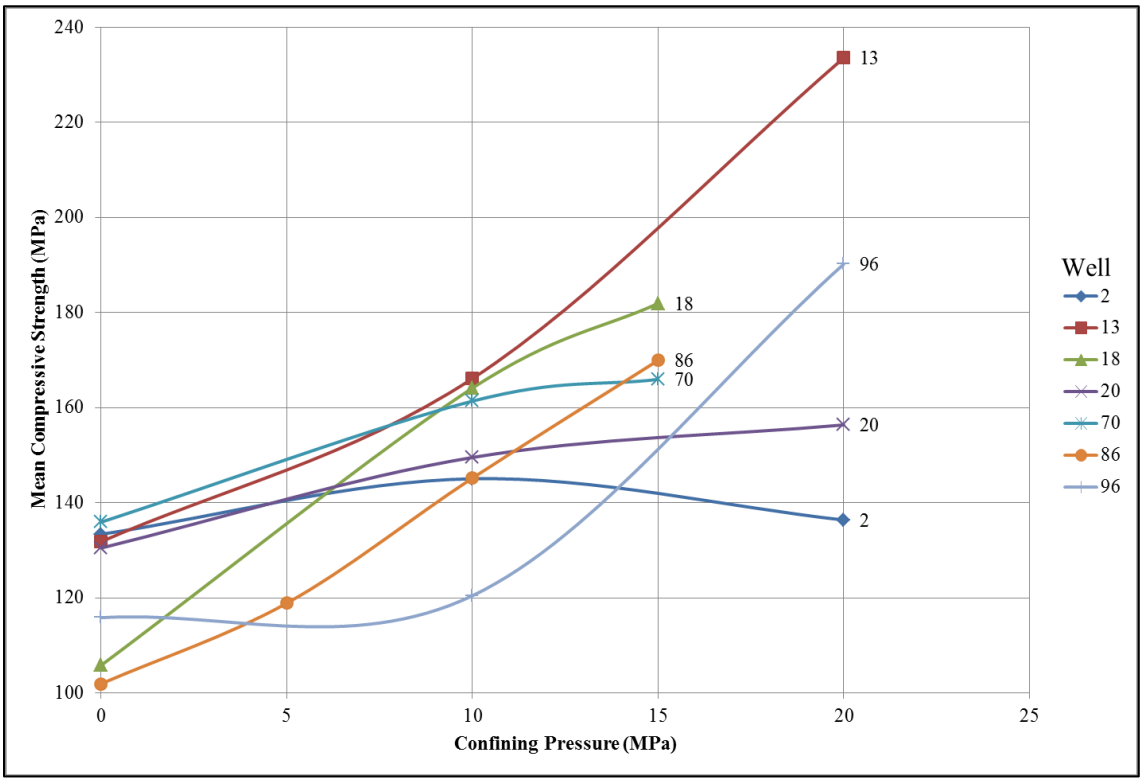

Figure 4.28 Mean Compressive Strength vs. Confining Pressure

If the stresses that rocks are subjected to are high enough, then plastic deformation will be permanent. With plastic deformation, rock cannot be recovered even upon the removal of the applied stresses. This condition for rock can be caused by three modes: tensile failure occurs when the effective tensile stress exceeds the tensile strength; compaction failure occurs under pure hydrostatic loading or non-hydrostatic stress conditions at high confining pressure; shear failure occurs when the shear stress along some plane is sufficiently high.

Shear failure is the most common failure mode, which can be described by many empirical standards. Mohr-Coulomb failure criterion is the most popular one among those criteria which describe the shear failure. It assumes a linear envelope can be

expressed as (Fjaer et al, 1992):

$$\tau = \mu\sigma + C \tag{4.24}$$

where τ is the shear strength, μ is the coefficient of internal friction, C is the rock cohesion, and σ is the normal stress on the shear plane (Figure 4.29).

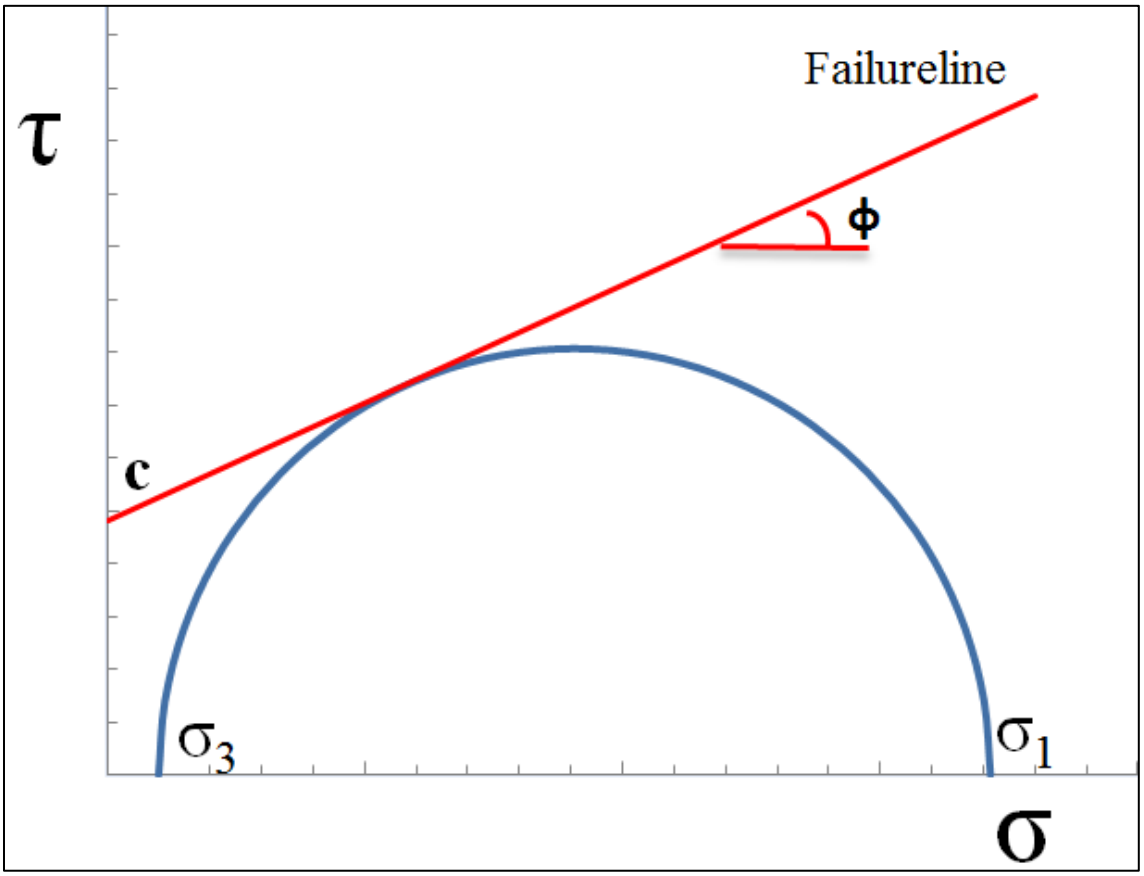

Figure 4.29 Schematic diagram of Mohr-Coulomb Criterion
σ_1: maximum principal stress, σ_3: minimum principal stress, and $\mu = \tan\phi$.

Based on the ultimate compressive strength, the Mohr-Coulomb failure envelopes are drawn for the five AUs in Figures E.1, E.2, E.3, E.4 and E.5, respectively. Moreover, those Mohr-Coulomb failure envelopes are expressed as:

Nesson-Little Knife Structural AU: $\tau = \sigma \tan(27.8^0) + 36.00MPa$ (4.25)

Central Basin-Poplar Dome AU: $\tau = \sigma \tan(45.17^0) + 25.25MPa$ (4.26)

Northwest Expulsion Threshold AU: $\tau = \sigma \tan(44.95^0) + 20.84MPa$ (4.27)

Elm Coulee-Billings Nose AU: $\tau = \sigma \tan(23.37^0) + 45.43MPa$ (4.28)

Eastern Expulsion Threshold AU: $\tau = \sigma \tan(23.39^0) + 48MPa$ (4.29)

According to the Mohr-Coulomb failure envelopes (Figures E.1 – E.5, and Equations (4.25) - (4.29)), there exist two classes roughly: one includes Central Basin-Poplar Dome AU and Northwest Expulsion Threshold AU, which has lower cohesion and higher coefficient of internal friction; other AUs belong to the second class which has higher cohesion and lower coefficient of internal friction.

CHAPTER V

CONCLUSION AND RECOMMENDATIONS

5.1. Conclusions

Upon the study we finished, following conclusions were made:

1) The freezing sample method is useful to overcome the difficulty of sampling.
2) The porosity of Bakken Formation is usually less than 6%.
3) Three methods to measure the low permeability in the tight rock were proved, and Radius-of-Investigation method is the fastest one.
4) The compressibility of rock can be obtained indirectly from two permeability experiments, Downstream Pressure Buil-up measurement and Radius-of-Investigation measurement.
5) A velocity correlation between P-wave and S-wave derived for Bakken Formation in this study can be used to estimate the velocity of S-wave from P-wave.
6) The comparison of static and dynamic elastic moduli shows that the static elastic modulus can be larger than that of dynamic for Bakken Formation.
7) A new method to determine Biot’s Coefficient was proposed.
8) The Biot's coefficients were obtained for Bakken samples which are taken along

two principal directions. Horizontal samples lie in the bedding plane, and vertical samples are perpendicular to the bedding. The average Biot's coefficient for horizontal samples is 0.67 higher than the one for perpendicular samples. This anisotropy of Biot's coefficient of Bakken Formation indicates that the Bakken Formation is heterogeneous. The influence of the pore pressure to the in-situ stress is greater along the bedding plane than perpendicular to the bedding.

9) According to the characteristic of Mohr-Coulomb failure envelopes made for the five AUs (Figure 3.1) with the ultimate compressive strength, there exists two classes roughly: one includes Central Basin-Poplar Dome AU and Northwest Expulsion Threshold AU; other AUs belong to the second class.

5.2. Recommendations

Further study focus on:

1) Verifying the permeability measurement with steady-state method.
2) Verifying the result with X-ray microanalysis.
3) Developing effective method to obtain tensile strength of high strength rock, such as Bakken shale.
4) Combining the core data of this study with well-logs to make a geological model to better understand Bakken Formation.

5) Verifying and using the result in hydraulic fracturing for Bakken Formation to create more accurate reservoir simulation.

APPENDICES

Appendix A

Derivation of Equation for Oscillating Pulse Measurement

Kranz et al. (1990) derived an analytical solution of the diffusion equation for 1-D flow along a finite sample excited by a pore pressure oscillation. The problem consists on finding *P(x, t)* such that

$$\frac{\partial P}{\partial t} = D\frac{\partial^2 P}{\partial x^2}(D>0)(0<x<L) \tag{A.1}$$

where *D* is the coefficient of diffusion, with two boundary conditions:

1) At x=0, $P(0,t) = Ae^{i\omega t}$,

2) At x=L, $\frac{\partial P}{\partial t} + \lambda\frac{\partial P}{\partial x} = 0(\lambda>0)$

where ω is the angular frequency, $\lambda = \frac{kA}{\mu c_g V_2}$. k is the permeability, A is the area of cross-section, V_2 is the volume of the downstream reservoir, and μ and c_g are the viscosity and compressibility of the gas, respectively.

The periodic solution as a function of distance x from the upstream and time t is

$$P(x,t) = \frac{A\{[i\omega-\lambda(1+i)N]e^{i\omega t+(1+i)N(x-L)} - [i\omega+\lambda(1+i)N]e^{i\omega t-(1+i)N(x-L)}\}}{[i\omega-\lambda(1+i)N]e^{-(1+i)\mathrm{NL}} - [i\omega+\lambda(1+i)N]e^{(1+i)\mathrm{NL}}} \tag{A.2}$$

where $N = \sqrt{\frac{\omega}{2D}}$. Thus, at *x=L*, *P(x, t)* reduces to:

$$P(\mathrm{L},t) = \frac{Ae^{i\omega t}[-2\lambda(1+i)N]}{[i\omega-\lambda(1+i)N]e^{-(1+i)\mathrm{NL}} - [i\omega+\lambda(1+i)N]e^{(1+i)\mathrm{NL}}} \tag{A.3}$$

By comparing *P(L, t)* with *P(0, t),* we have

$$\frac{P(\mathrm{L},t)}{P(0,t)} = \frac{-2\lambda(1+i)N}{[i\omega-\lambda(1+i)N]e^{-(1+i)\mathrm{NL}} - [i\omega+\lambda(1+i)N]e^{(1+i)\mathrm{NL}}} \tag{A.4}$$

The ratios of *P(L, t)* to *P(0, t)* is a function of λ and *N*. With two dimensionless variables $\alpha = \frac{N\lambda}{\omega}$, and $\gamma = NL$, the measurable amplitude ratios R and phase difference are expressed in terms of α and γ:

$$R^2 = \frac{4\alpha^2}{(2\alpha^2+1)\cosh 2\gamma + (2\alpha^2-1)\cos 2\gamma + 2\alpha(\sinh 2\gamma - \sin 2\gamma)} \tag{A.5}$$

$$\delta = \arctan\left[\frac{\tanh(2\alpha\tan\gamma+1)+\tan\gamma}{\tan\gamma-\tanh\gamma+2\alpha}\right] \tag{A.6}$$

After measuring R and δ from experimental measurement, we can calculate α and γ from Equations (A.5) and (A.6). Then permeability can be determined with Equation (A.7)

$$k = \frac{\mu c_g V_2}{A}\lambda = \frac{\mu c_g V_2}{A}\left(\frac{\alpha\omega L}{\gamma}\right) \tag{A.7}$$

Appendix B

Derivation of Equation for Downstream Pressure Build-up Measurement

Hsieh et al. (1981) and Dicker and Smits (1988) gave the exact solution to Equation (3.14) for the pressure in the downstream reservoir, which is:

$$\frac{m[p_2(t)]-m[p_2(0)]}{m[p_1(0)]-m[p_2(0)]} = \frac{b}{a+b+ab}+2\sum_{m=1}^{\infty}\frac{e^{-t_D\theta_m{}^2}\left(ab^2-b\theta_m{}^2\right)}{[\theta_m{}^4+\theta_m{}^2\left(a+a^2+b+b^2\right)+ab(a+b+ab)]\cos\theta_m} \qquad \text{(B.1)}$$

where θ_m can be calculated from the following equation

$$tan\theta=\frac{(a+b)\theta}{\theta^2-ab} \qquad \text{(B.2)}$$

where a is the ratio of the sample pore volume (V_p) over the upstream reservoir volume (V_1); and b is the ratio of the sample pore volume over the downstream reservoir volume (V_2), $\left(a=\frac{V_p}{V_1}, b=\frac{V_p}{V_2}\right)$.

In Equation (B.1) the dimensionless time, t_D, is defined as:

$$t_D=\frac{kt}{\phi\mu c_t L^2} \qquad \text{(B.3)}$$

By careful observation it is clear that uz can be treated as a constant in the range of pressure less than 2000 psi, which is the pressure conditions used in this study. According to $m(p)=\int_{p_b}^{p}\frac{2p}{\mu z}dp$, the left-hand side (LHS) of Equation (B.1) can be written as

$$\frac{m\left[p_2(t)\right]-m\left[p_2(0)\right]}{m\left[p_1(0)\right]-m\left[p_2(0)\right]}=\frac{\int_{p_2(0)}^{p_2(t)}\frac{2p}{uz}dp-\int_{p_2(0)}^{p_2(0)}\frac{2p}{uz}dp}{\int_{p_2(0)}^{p_1(0)}\frac{2p}{uz}dp-\int_{p_2(0)}^{p_2(0)}\frac{2p}{uz}dp}=\frac{{p_2}^2(t)-{p_2}^2(0)}{{p_1}^2(0)-{p_2}^2(0)}$$

Next, the RHS of Equation (B.1) is simplified. The upstream pressure p_1 is invariant throughout the test, which implies that the upstream volume V_1 leads to infinity, so the ratio of the sample pore volume to the upstream volume ($a=\frac{V_p}{V_1}$) can be considered as zero. Substituting a as zero and Equation (B.4) into Equation (B.1), we obtain:

$$\frac{{p_2}^2(t)-{p_2}^2(0)}{{p_1}^2(0)-{p_2}^2(0)}=1+2\sum_{m=1}^{\infty}\frac{e^{-t_D{\theta_m}^2}(-b{\theta_m}^2)}{[{\theta_m}^4+{\theta_m}^2(b+b^2)]\cos\theta_m}$$

which can be written as

$$\frac{{p_1}^2(0)-{p_2}^2(t)}{{p_1}^2(0)-{p_2}^2(0)}=2\sum_{m=1}^{\infty}\left(e^{-t_D{\theta_m}^2}\cdot\frac{b{\theta_m}^2}{[{\theta_m}^4+{\theta_m}^2(b+b^2)]\cos\theta_m}\right) \qquad \text{(B.5)}$$

For $a = 0$, Equation (B.2) becomes

$$tan\,\theta=\frac{b}{\theta} \qquad \text{(B.6)}$$

which can be written in the following format $\frac{\sin\theta}{\cos\theta}=\frac{b}{\theta}$ that leads to $cos\,\theta=\sqrt{\frac{\theta^2}{\theta^2+b^2}}$. This equation contains an infinite number of solution θm and the values of the solutions increase monotonically. Thus $\cos\theta_m=(-1)^{m-1}\frac{\theta_m}{\sqrt{{\theta_m}^2+b^2}}$. Inserting this into Equation (A.5), we obtain

$$\frac{p_1^{\,2}(0)-p_2^{\,2}(t)}{p_1^{\,2}(0)-p_2^{\,2}(t)}=2\sum_{m=1}^{\infty}\left(e^{-t_D\theta_m^{\,2}}\cdot\frac{(-1)^{m-1}b\sqrt{\theta_m^{\,4}+\theta_m^{\,2}b^2}}{\theta_m^{\,4}+\theta_m^{\,2}(b+b^2)}\right) \tag{B.7}$$

Although Dicker and Smits (1988) mentioned that theoretically Equation (B.7) is single exponentially decreasing only when the upstream reservoir and the downstream reservoir have the same volume, they still indicated that in order to expedite the experiment in practical operation the volume of the upstream reservoir is usually much larger than the volume of the downstream reservoir. In this case, a single exponential equation fit very well with the downstream pressure build-up curve when the right interval was selected. Thus, Equation (B.7) was simplified to:

$$\frac{p_1^{\,2}(0)-p_2^{\,2}(t)}{p_1^{\,2}(0)-p_2^{\,2}(t)}=e^{-t_D\theta_1^{\,2}}\cdot\left(2\frac{b\sqrt{\theta_1^{\,4}+\theta_1^{\,2}b^2}}{\theta_1^{\,4}+\theta_1^{\,2}(b+b^2)}\right) \tag{B.8}$$

Letting $\Delta p(t)=p_1^{\,2}(0)-p_2^{\,2}(t)$,

$$\frac{\Delta p(t)}{\Delta p(0)}=\left(2\frac{b\sqrt{\theta_1^{\,4}+\theta_1^{\,2}b^2}}{\theta_1^{\,4}+\theta_1^{\,2}(b+b^2)}\right)\cdot e^{-t_D\theta_1^{\,2}} \tag{B.9}$$

which can be written as:

$$\Delta p(t)=\left(2\Delta p(0)\cdot\frac{b\sqrt{\theta_1^{\,4}+\theta_1^{\,2}b^2}}{\theta_1^{\,4}+\theta_1^{\,2}(b+b^2)}\right)\cdot e^{-t_D\theta_1^{\,2}} \tag{B.10}$$

Taking the natural log of Equation (B.10) yields:

$$\ln\left[\Delta p(t)\right] = \ln\left(2\Delta p(0)\cdot\frac{b\sqrt{\theta_1^4+\theta_1^2 b^2}}{\theta_1^4+\theta_1^2(b+b^2)}\right)+\left(-t_D\theta_1^2\right) \tag{B.11}$$

Substituting t_D from Equation (B.3) into Equation (B.11):

$$\ln\left[\Delta p(t)\right] = \ln\left(2\Delta p(0)\cdot\frac{b\sqrt{\theta_1^4+\theta_1^2 b^2}}{\theta_1^4+\theta_1^2(b+b^2)}\right)-\frac{\theta_1^2 k}{\phi\mu c_t L^2}t \tag{B.12}$$

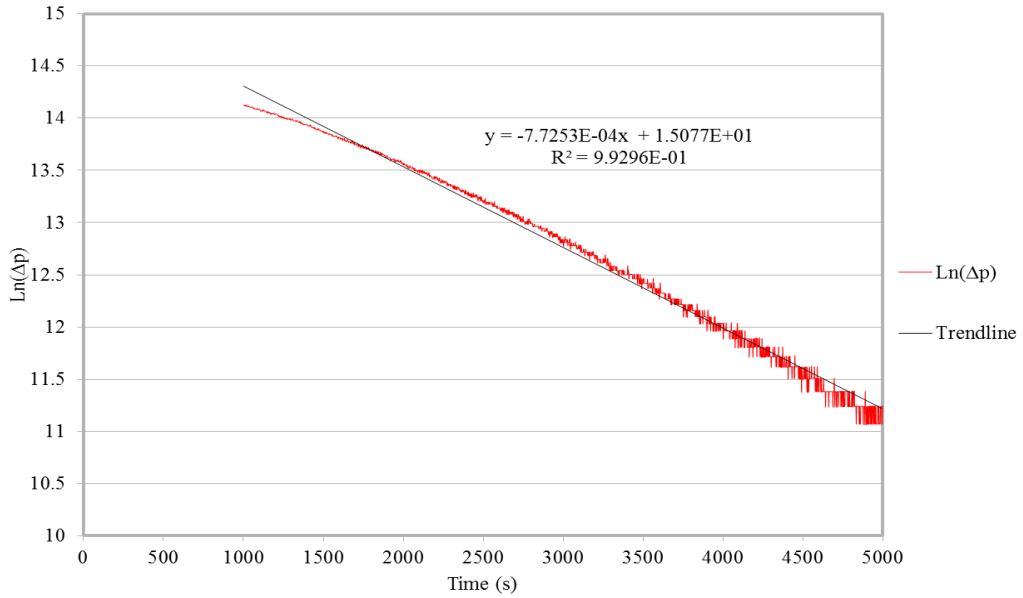

Figure B.1 ln(Δ*p*) vs. time plot for Core #1.

Assigning $s = \frac{-\theta_1^2 k}{\phi\mu c_t L^2}$, which is the slope of the pressure difference in a logarithm as a function of time based on Equation (B.12) (Figure B.1); permeability can be easily obtained from Equation (B.13) when s is fitted as in Figure B.1.

$$k = \frac{-\phi\mu c_t L^2}{\theta_1^2}\cdot s \tag{B.13}$$

Using the Taylor series of tanθ, $\tan\theta \approx \theta + \frac{\theta^3}{3}$, we can calculate θ1 from Equation (A.6):

$\theta_1 + \frac{\theta_1^3}{3} = \frac{b}{\theta_1}$, and

$$\theta_1^2 = \frac{3}{2}\left(-1 + \sqrt{1 + \frac{4}{3}b}\right) \tag{B.14}$$

Substituting Equation (B.14) into Equation (B.13):

$$k = \frac{2\phi\mu c_t L^2 s}{3 - 3\sqrt{1 + \frac{4}{3}b}} \tag{B.15}$$

Considering that $b = \frac{V_p}{V_2} = \frac{\phi AL}{V_2} = \frac{\phi\pi D^2 L}{4V_2}$, the equation becomes:

$$k = \frac{2\phi\mu c_t L^2 s}{3 - 3\sqrt{1 + \frac{\phi\pi D^2 L}{3V_2}}} \tag{B.16}$$

Appendix C

Derivation of Equation for Radius-of-Investigation Measurement

According to the solution to the diffusivity Equation (3.14), for an instantaneous pressure disturbance in an infinite linear system (Carslaw, 1959), we have:

$$m(p) = \frac{Q}{\sqrt{t}} \exp\left(\frac{-x^2}{4\frac{k}{\phi\mu c_t}t} \right) \tag{C.1}$$

where Q is a constant, which is related to the strength of the instantaneous pressure disturbance.

It is a physics problem of extreme value to find the time at which the pressure disturbance reaches its maximum. The maximum solution can be solved when the time derivative of the Equation (C.1) equals zero:

$$\frac{d\left[m(p)\right]}{dt} = \frac{d\left[\frac{Q}{\sqrt{t}} \exp\left(\frac{-x^2}{4\frac{k}{\phi\mu c_t}t} \right) \right]}{dt} = 0 \tag{C.2}$$

which is:

$$\frac{d\left[m(p)\right]}{dt}=\exp\left(\frac{-x^2}{4\frac{k}{\phi\mu c_t}t}\right)\frac{d\left[\frac{Q}{\sqrt{t}}\right]}{dt}+\frac{Q}{\sqrt{t}}\frac{d\left[\exp\left(\frac{-x^2}{4\frac{k}{\phi\mu c_t}t}\right)\right]}{dt}=0 \tag{C.3}$$

Simplifying the above equations lead to:

$$\frac{d\left[m(p)\right]}{dt}=\left[-\frac{Q}{2t^{\frac{3}{2}}}\right]\cdot\exp\left(\frac{-x^2}{4\frac{k}{\phi\mu c_t}t}\right)+\left(\frac{x^2Q}{4\frac{k}{\phi\mu c_t}t^{\frac{5}{2}}}\right)\cdot\exp\left(\frac{-x^2}{4\frac{k}{\phi\mu c_t}t}\right)=0 \tag{C.4}$$

Finally, Equation (C.5) is obtained as:

$$\frac{d\left[m(p)\right]}{dt}=\frac{Q}{2t^{\frac{3}{2}}}\cdot\exp\left(\frac{-x^2}{4\frac{k}{\phi\mu c_t}t}\right)\cdot\left[-1+\frac{x^2}{2\frac{k}{\phi\mu c_t}t}\right]=0 \tag{C.5}$$

Considering the initial condition at t=0 and $p(x,t=0)=p_2$, t=0 is a trivial solution to Equation (C.5). Dividing both sides of the Equation (B.5) by $\frac{Q}{2t^{\frac{3}{2}}}\cdot\exp\left(\frac{-x^2}{4\frac{k}{\phi\mu c_t}t}\right)$ yields

$$-1+\frac{x^2}{2\frac{k}{\phi\mu c_t}t}=0$$

.

Rearranging the equation, we get the time:

$$t_m = t = \frac{\phi \mu c_t x^2}{2k} \tag{C.6}$$

Expressing permeability in terms of porosity, viscosity, total compressibility, location, and time, Equation (C.6) can be written as:

$$k = \frac{\phi \mu c_t x^2}{2t_m} \tag{C.7}$$

Converting Equation (C.7) into U.S. field units we have:

$$k = \frac{1896 \phi \mu c_t x^2}{t_m} \tag{C.8}$$

where permeability k is in mD, porosity ϕ is dimensionless (in fraction), viscosity μ is in cp, total compressibility c_t is in psi^{-1}, time tm is in hour, and location (or distance) x is in ft.

Equations (C.7) and (C.8) are the governing equations to measure the rock permeability. They are used to calculate the permeability of any rock that meets the aforementioned assumptions and can be used for high-permeability rocks as well. The proposed method evaluates the permeability under unsteady-state flow and requires a short time period to determine the flow capacity of the low-permeability rock.

Appendix D

Pressure-Time Graphs

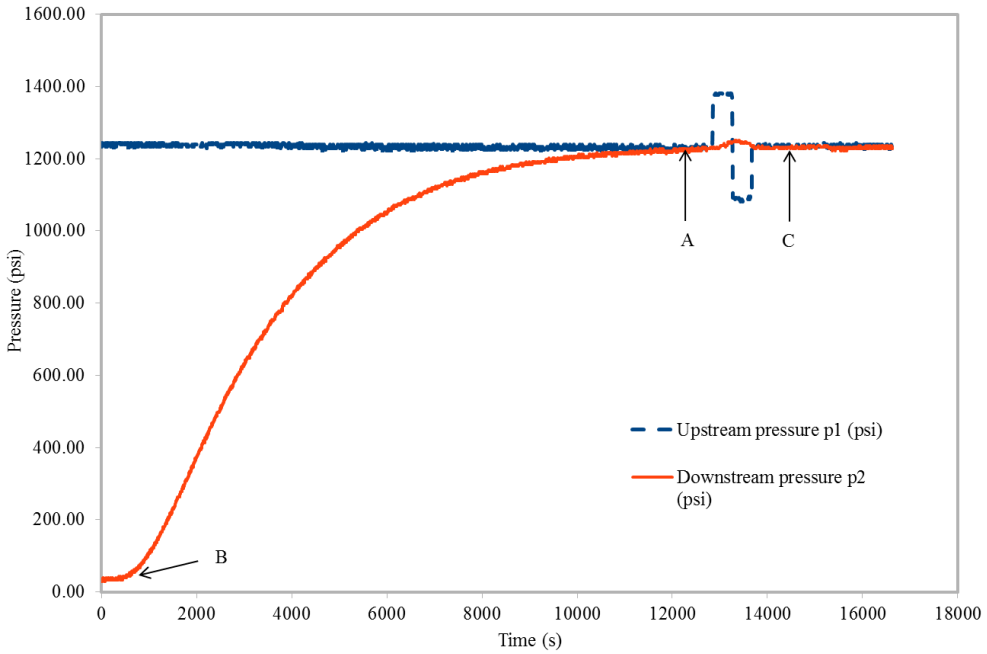

Figure D.1 Changes of the upstream and downstream pressure during one experiment for Core #2

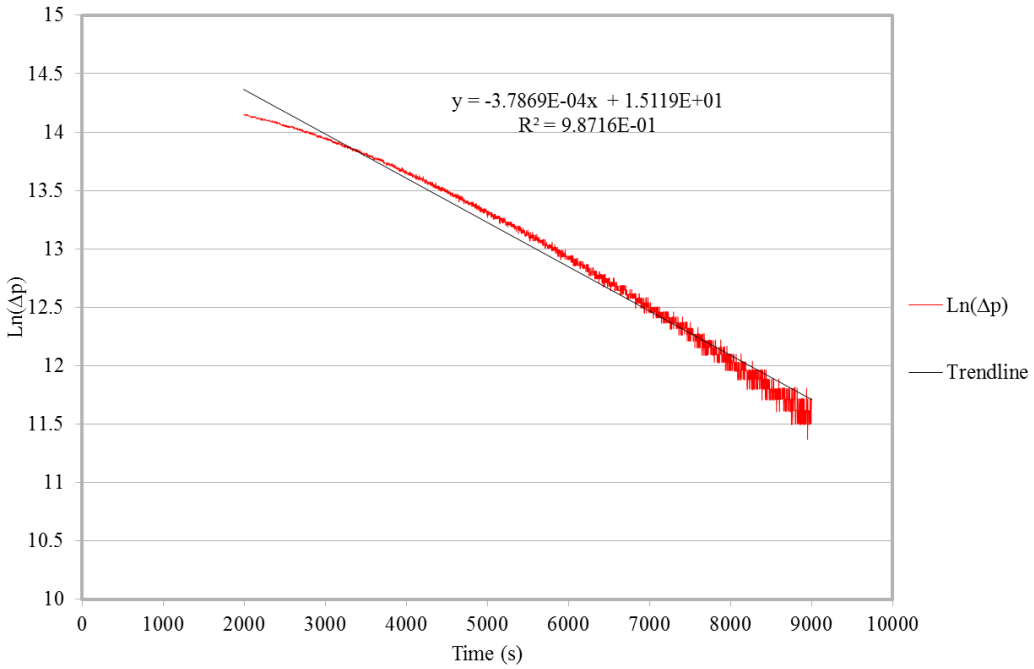

Figure D.2 ln(Δp) vs. time plot for Core #2

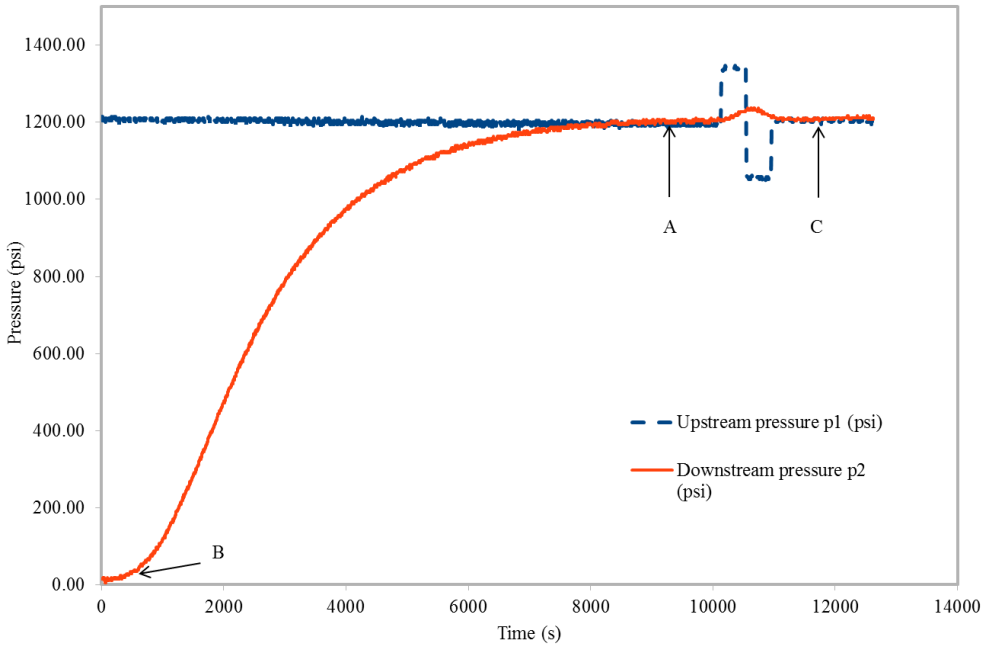

Figure D.3 Changes of the upstream and downstream pressure during one experiment for Core #3

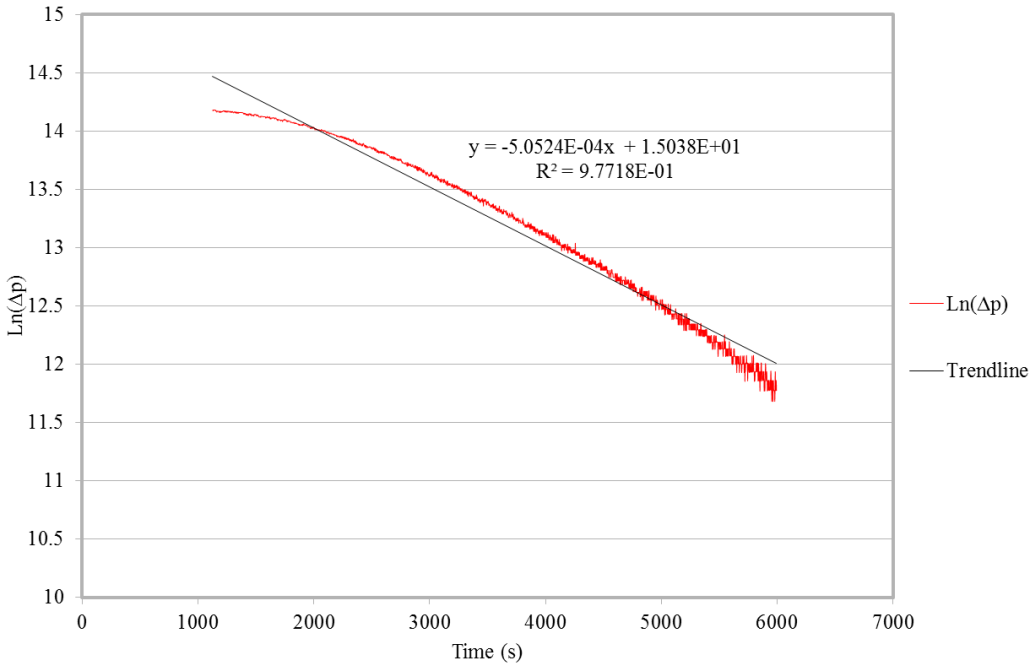

Figure D.4 ln(Δp) vs. time plot for Core #3

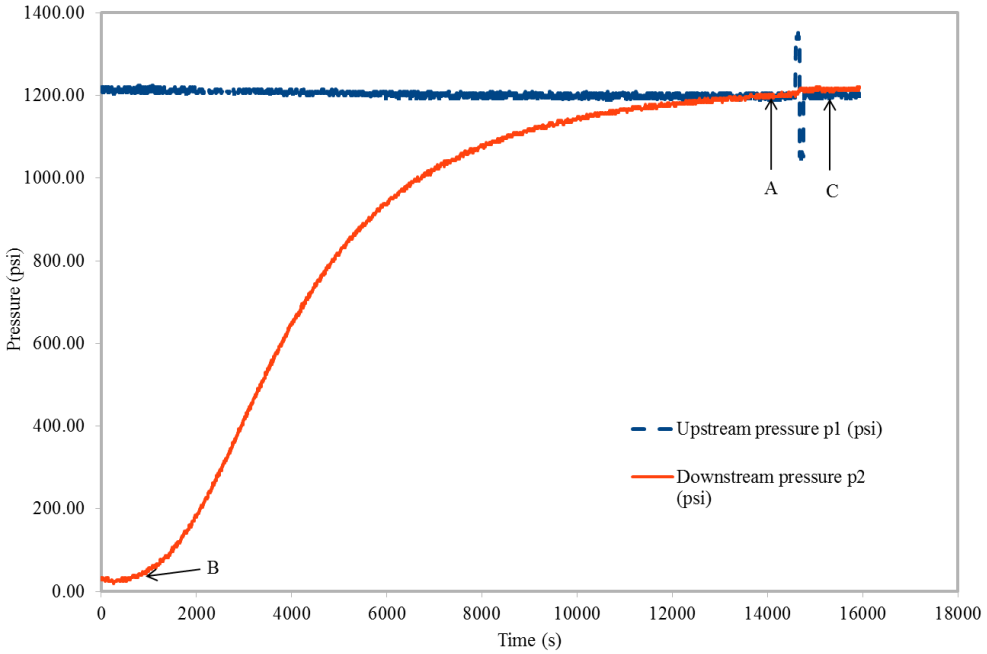

Figure D.5 Changes of the upstream and downstream pressure during one experiment for Core #4

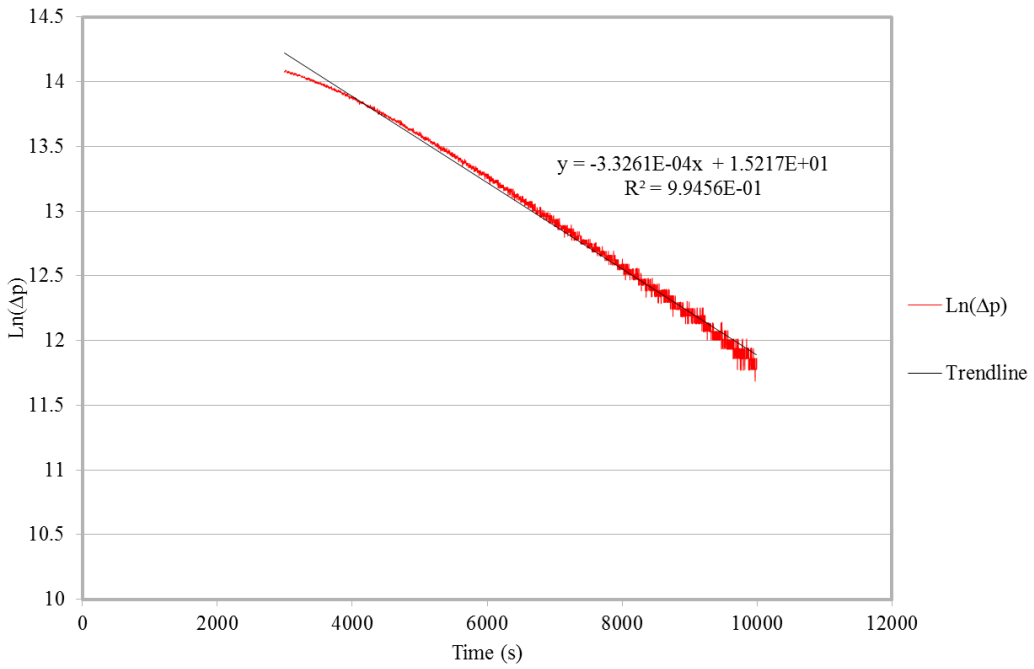

Figure D.6 ln(Δp) vs. time plot for Core #4

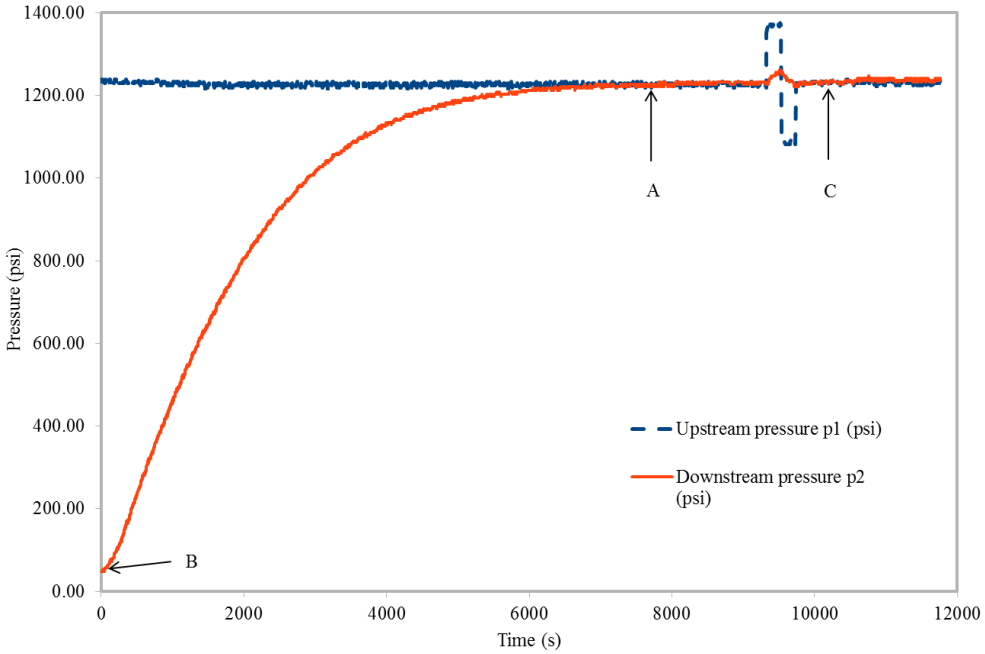

Figure D.7 Changes of the upstream and downstream pressure during one experiment for Core #5

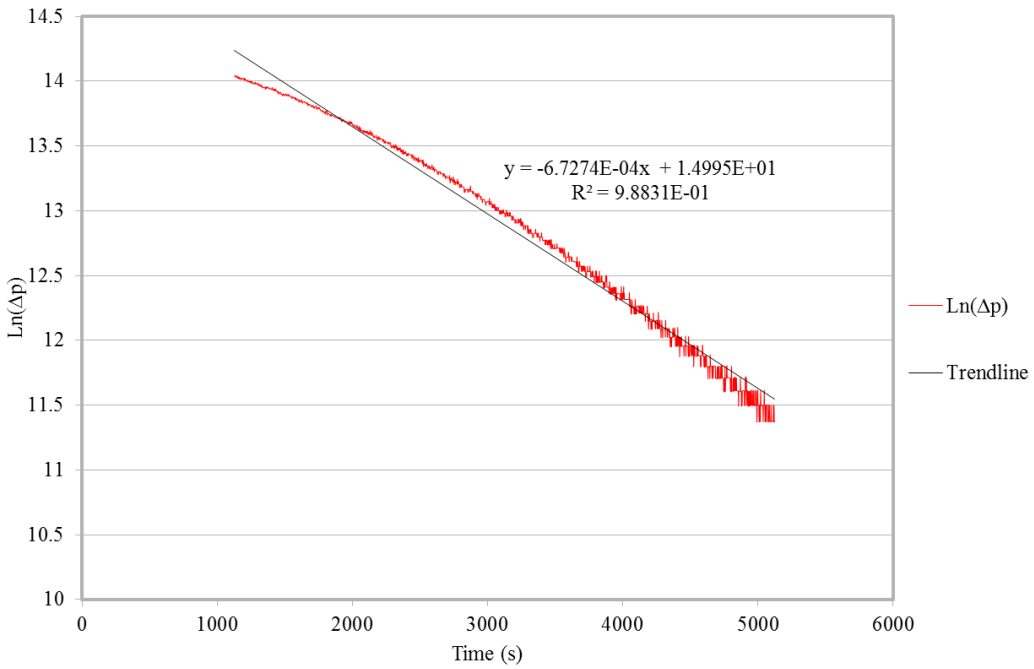

Figure D.8 ln(Δp) vs. time plot for Core #5

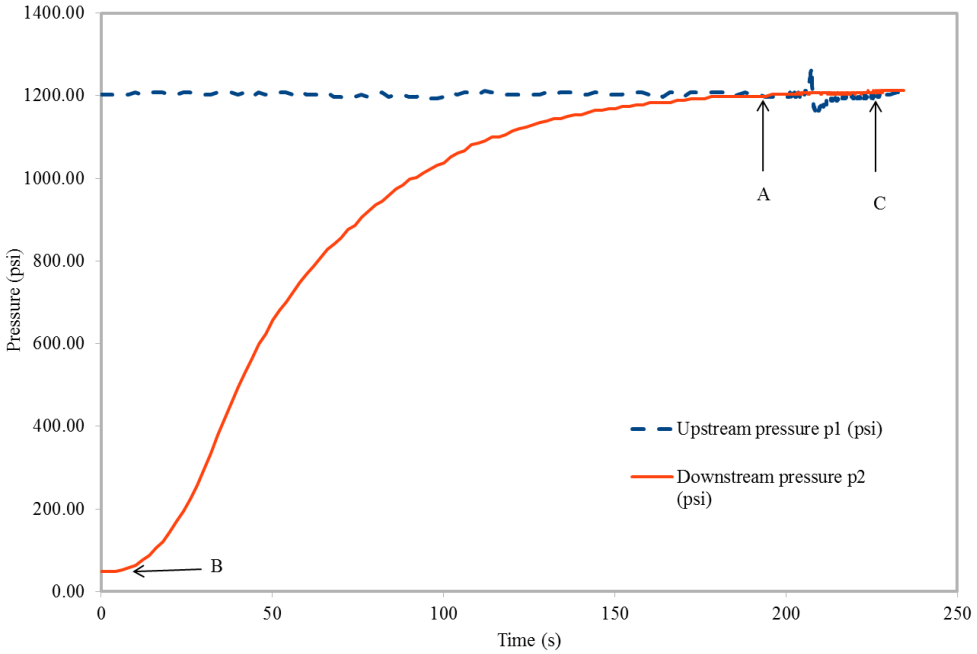

Figure D.9 Changes of the upstream and downstream pressure during one experiment for Core #6

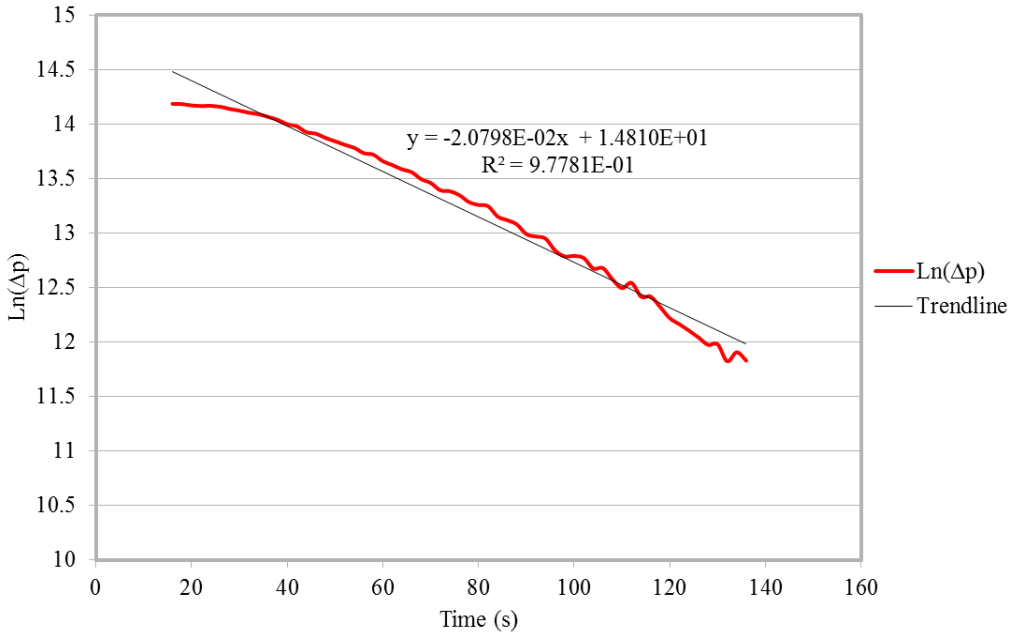

Figure D.10 ln(Δp) vs. time plot for Core #6

Appendix E

Mohr-Coulomb Failure Envelope

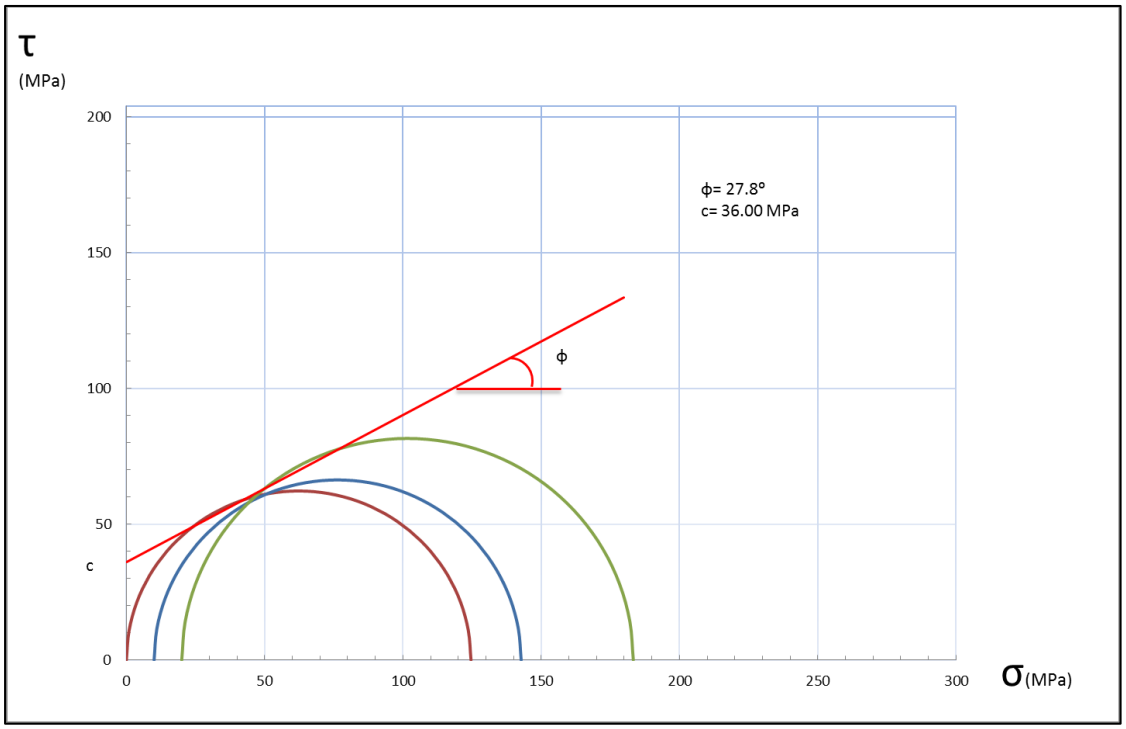

Figure E.1 Mohr-Coulomb failure envelope of Nesson-Little Knife Structural AU

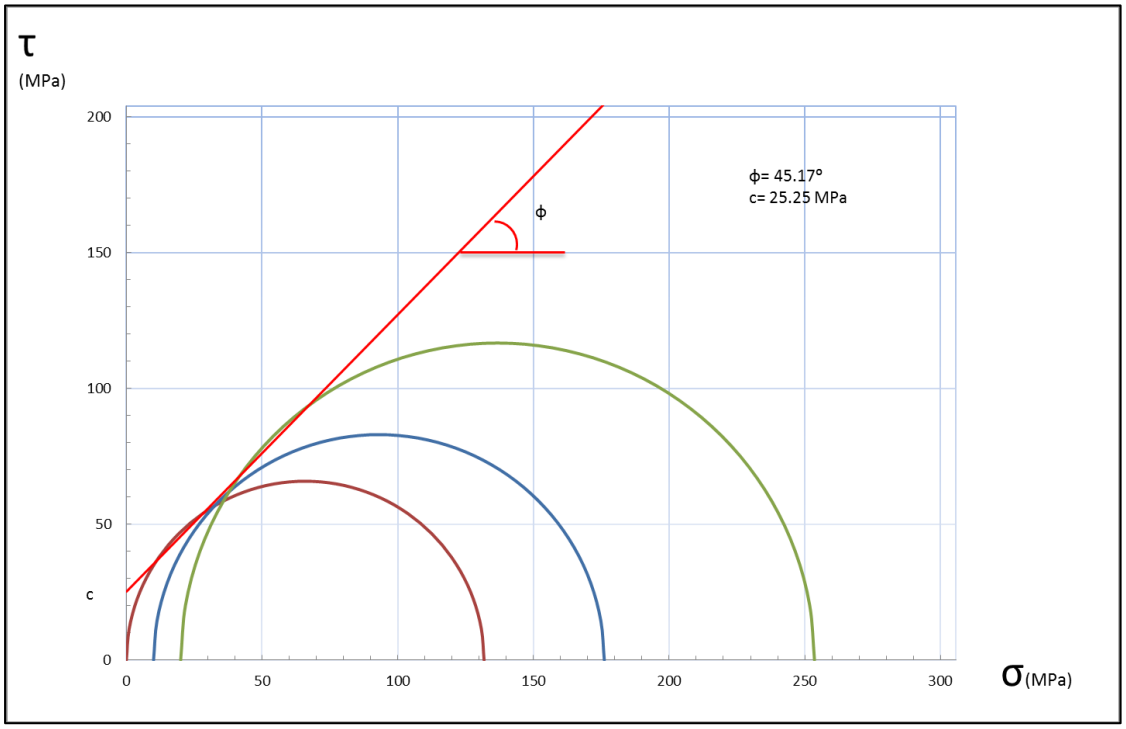

Figure E.2 Mohr-Coulomb failure envelope of Central Basin-Poplar Dome AU

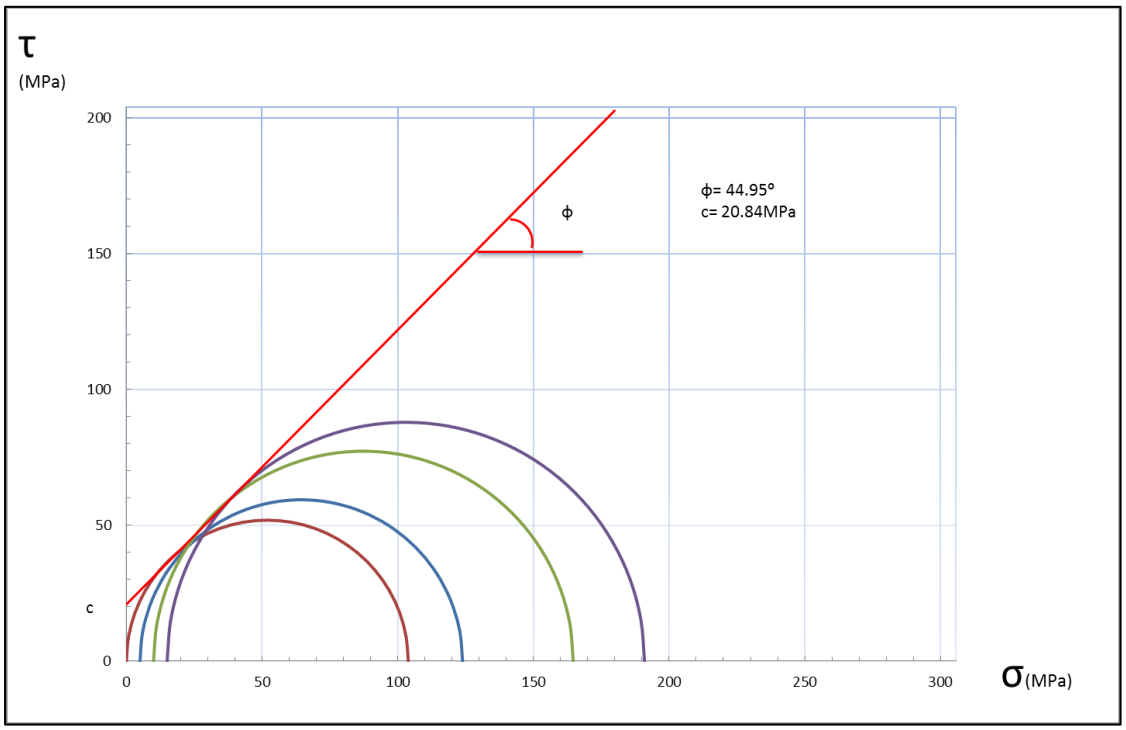

Figure E.3 Mohr-Coulomb failure envelope of Northwest Expulsion Threshold AU

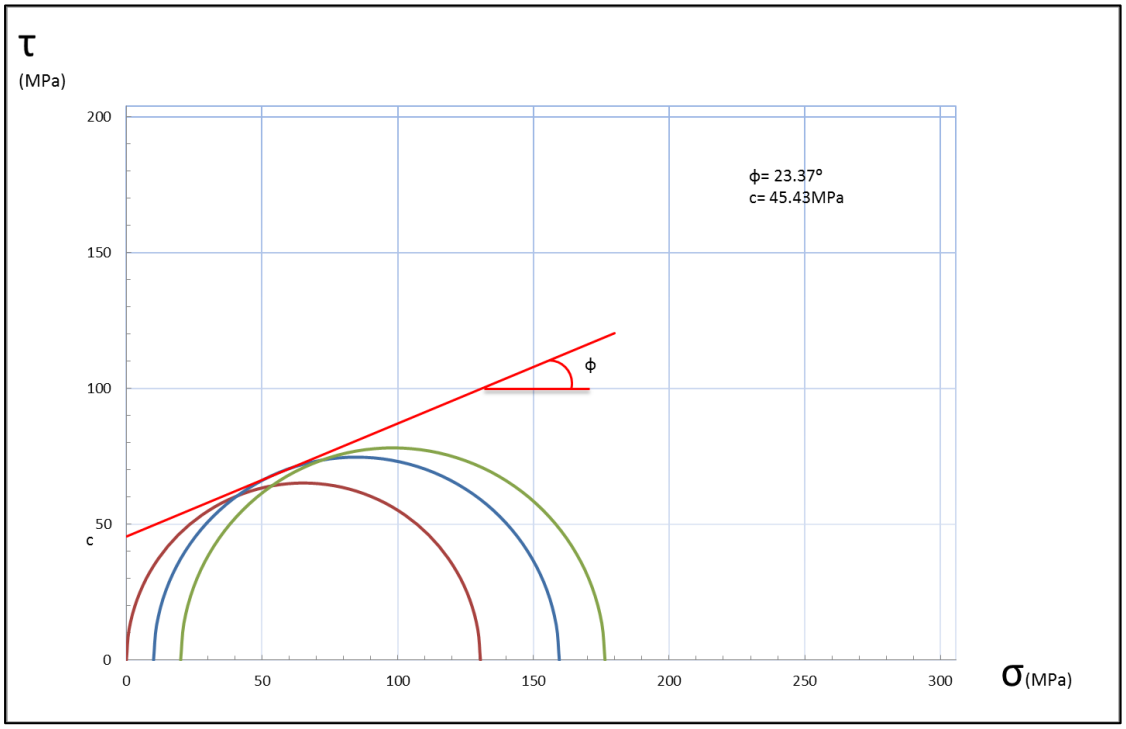

Figure E.4 Mohr-Coulomb failure envelope of Elm Coulee-Billings Nose AU

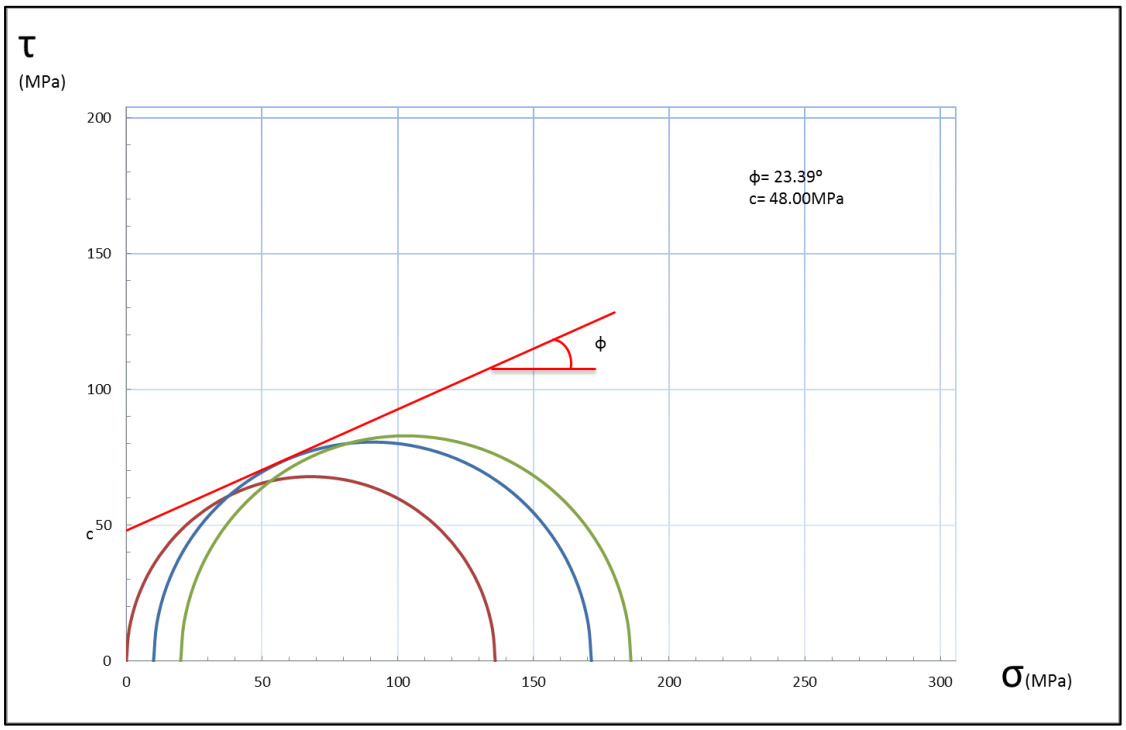

Figure E.5 Mohr-Coulomb failure envelope of Eastern Expulsion Threshold AU

REFERENCES

Al-Hussainy, R., Ramey, H. J., & Crawford, P. B. 1966. The Flow of Real Gases Through Porous Media. Society of Petroleum Engineers.

AutoLab 1500 Manual. 2009. New England Research Inc.

Aviles, C. A., C. H. Scholz, and J. Boatwright. 1987. Fractal analysis applied to characteristic segments of the San Andreas Fault, J. Geophys. Res., 92(B1), 331–344

Azeemuddin, M., Khan, K., Khan, M. N., Abdulraheem, A., Rahim, Z., & Al-Qahtani, M. Y. 2002. Experimental Determination of Elastic Anisotropy and Biot's Constant in a Saudi Arabian Reservoir Sandstone. Society of Petroleum Engineers. doi:10.2118/78503-MS

Bertoncello, A. and Honarpour, M.M., 2013. Standards for Characterization of Rock Properties in Unconventional Reservoirs: Fluid Flow Mechanism, Quality Control, and Uncertainties. SPE 166470-MS

Biot, M. A. 1941. General theory of three-dimensional consolidation, J. appl. Physics, Lancaster Pa., 12 (1941) 155–164.

Boitnott, G.N., 1997. Use of Complex Pore Pressure Transients to Measure Permeability of Rocks. SPE 38717-MS

Brace, W. F., and Martin, 1968. A test of the law of effective stress for crystalline rock of low porosity, International Journal of Rock Mechanics and Mining Science V5 (5)

Brace, W. F., Walsh, J. B., and Frangos, W. T. 1968. Permeability of Granite under High Pressure. Journal of Geophysical Research, p. 2225-2236.

Bravo, L. and M. Aldana. 2011. Volume curvature attributes to identify subtle faults and fractures in carbonate reservoirs: Cimarrona Formation, Middle Magdalena Valley Basin, Colombia. In the 2010 SEG Annual Meeting, Denver, Colorado. 17-22 October, 2010.

Brown, S.R. and C.H. Scholz, 1985. Broad bandwidth study of the topography of natural rock surfaces. Jour. of Geophys. Res., 90: 12,575 - 12,582.

Bruno, M., and Nakagawa, F. M. 1991, Pore pressure influence on tensile fracture propagation in sedimentary rock V28 (4) (1991) 261–273

Canady, W.J., 2011. A Method for Full-Range Young's Modulus Correction. Society of Petroleum Engineers.

Carlaw, H. S., and Jaeger, J. C. 1959. Conduction of Heat in Solids, second edition. Oxford at Clarendon Press, P50

Carlisle, W.J., Dryff, L., Fryt, M.S., Artindale, J.S., and Von Der Dick, H. 1996. The Bakken Formation – an Integrated Geologic Approach to Horizontal Drilling. In Production from Fractured Shales, SPE Reprint Series No. 45, Society of Petroleum Engineers, Texas.

Carpenter, C.R. and G.R. Spencer. 1940. Measurements of Compressibility of Consolidated Oil-Bearing Sandstones. Bureau of Mines RI 3540, October 1940.

Cart, J.R. and J.B. Warriner. 1987. Rock mass classification using fractal dimension. In Proc. 28th U.S. Symp. Rock Mech., I. Farmer, et al., eds., Balkema, Boston, p. 73-80.

Chalaturnyk, R.J. and J.D. Scott. 1992. Evaluation Of Reservoir Properties From Geomechanical Tests. Journal of Canadian Petroleum Technology. Vol. 31, No. 5, p. 31-40.

Coussy, O. 2005. Poromechanics of freezing materials. Journal of the Mechanics and Physics of Solids 53: 1689-1718.

Cui, X., Bustin, A.M.M., Bustin, R.M., 2009. Measurements of gas permeability and diffusivity of tight reservoir rocks: different approaches and their applications. Geofluids 9, P208–223.

Darcy, H. 1856. Les fontaines publiques de la ville de Dijon. Paris: V. Dalmont.

Dennis, B. and E. Slanden. 1988. Fracture Identification Techniques In Carbonates. In the 39th Annual Technical Meeting of the Petroleum Society of CIM, Calgary, Alberta. June 12 - 16, 1988.

Dicker, A. I., and Smits, R. M. 1988. A Practical Approach for Determining Permeability from Laboratory Pressure-Pulse Decay Measurements. SPE 17578, p. 285-292.

Dobrynin, V. M. 1962. Effect of Overburden Pressure on Some Properties Of Sandstones. Society of Petroleum Engineers. doi:10.2118/461-PA.

Dukes, R. T. 2013. Bakken Shale Map - USGS. http://bakkenshale.com/home/attachment/bakken-formation-map-usgs-2/

Economides, M.J. and Boney, C. 2000. Reservoir Stimulation in Petroleum Production. In Reservoir Stimulation (Economides and Nolte, eds.), Wiley and Sons, New York.

El-Gezeery, T. M. ., Al-Saqran, F., Archibong, E. I., and Al-Radhi, S. H. 2008. Utilizing Real Time Logging While Drilling Resistivity Imaging to Identify Fracture Corridors in a highly fractured Cabonate Reservoir. In the SPE Abu Dhabi International Petroleum Exhibition and Conference, Abu Dhabi, UAE. 3-6 November, 2008.

Fatt, I. 1953. The Effect of Overburden Pressure on Relative Permeability. Society of Petroleum Engineers. doi:10.2118/953325-G

Fatt, I. 1958a. Compressibility of sandstones at low to moderate pressures. AAPG Bulletin, August 1958, Vol. 42, p. 1924-1957.

Fatt, I. 1958b. Pore Volume Compressibilities of Sandstone Reservoir Rocks. Journal of Petroleum Technology, Vol. 10, No. 3, p. 64-66.

Fatt, I., and Davis, D. H. 1952. Reduction in Permeability With Overburden Pressure. Society of Petroleum Engineers. doi:10.2118/952329-G

Feng, Q., O. Stephansson, and A. Boberg. 1958. Fracture mapping at exposed rock faces by using close range digital photogrammetry and geodetic total station. In the 38th U.S. Symposium on Rock Mechanics (USRMS), Washington, D.C.. 7-10 July, 2001.

Fertl, W. H., and Rieke, H. H. 1980. Gamma Ray Spectral Evaluation Techniques Identify Fractured Shale Reservoirs and Source-Rock Characteristics. Journal of Petroleum Technology. Vol. 32, I. 11, p. 2053-2062.

Fischer, D., Smith, S., Peck, W., LeFever, J., LeFever, R., Helms, L., Sorensen, J., Steadman, E. and Harju, J. 2005. Overview of Williston Basin geology as it relates to CO2 sequestration. Report of the Plains CO2 Reduction Partnership Report, 169 Energy & Environmental Research Center, The University of North Dakota, Grand Forks, North Dakota.

Fjaer, E., 2008. Petroleum related rock mechanics. Elsevier, Amsterdam; Boston.

Franquet, J. A. S., and Abass, H. H. S. 1999. Experimental evaluation of Biot's poroelastic parameterThree different methods. American Rock Mechanics Association.

Geertsma, J. 1957. The Effect of Fluid Pressure Decline on Volumetric Changes of Porous Rocks. Society of Petroleum Engineers.

Greenwald, R.F. and W.H. Somerton. 1981a. Pore Volume Compressibility Data for Bandera, Berea, and Boise Sandstones, SPE 9746-MS.

Greenwald, R.F. and W.H. Somerton. 1981b. A Theoretical Model For Determination of Pore Volume Compressibilities of Consolidated Sandstones. SPE 10076-MS, SPE Annual Technical Conference and Exhibition, 4-7 October 1981, San Antonio, Texas.

Hall, H.N. 1953. Compressibility of Reservoir Rocks. Journal of Petroleum Technology. Vol. 5, No. 1, p. 17-19.

Han, G. 2011. Natural Fractures in Unconventional Reservoir Rocks: Identification, Characterization, and its Impact to Engineering Design. In the 45th US Rock Mechanics/Geomechanics Symposium held in San Francisco, CA, June 26–29, 2011.

Harville, D.W. and Hawkins, M. F. 1969. Rock Compressibility and Failure as Reservoir Mechanisms in Geopressured Gas Reservoirs. Journal of Petroleum Technology. Vol. 21, No. 12, p. 1528-1530.

He, J., and Ling, K. 2014. A New Method to Determine Biot Coefficients of Bakken Samples. American Rock Mechanics Association.

Heck, T.J., LeFever, R.D., Fischer, D.W. and LeFever, J. 2002. Overview of the Petroleum Geology of the North Dakota Williston Basin. North Dakota Geological Survey, Bismarck, ND.

Hester, T.C., and Schmoker, J.W. 1985. Selected physical properties of the Bakken Formation, North Dakota and Montana part of the Williston Basin: U.S. Geological Survey Oil and Gas Investigations Chart, OC-126, 1 sheet.

Hilbert, L.B.J., Hwong, T.K., Cook, N.G.W., Nihei, K.T., Myer, L.R., 1994. Effects of Strain Amplitude on the Static and Dynamic Nonlinear Deformation of Berea Sandstone. 1st North American Rock Mechanics Symposium.

Hsieh, P. A., Tracy, J. V., Neuzil, C. E., Bredehoeft, J. D., and Silliman, S. E. 1981. A transient laboratory method for determining the hydraulic properties of 'tight' rocks-I. Theory. International Journal of Rock Mechanics and Mining Sciences & Geomechanics Abstracts, 18, P245-252.

Hu, X., Liang, W., and Hou, S., et al. 2012. Experimental study of effect of temperature and stress on permeability characteristics of raw coal and shaped coal. Chinese Journal of Rock Mechanics and Engineering, 31 (6): 1222-1229.

Hudson, P.J. and Matson, R.P. 1992. Hydraulic Fracturing in Horizontal Wellbores. Paper SPE 23950, SPE Permian Basin Oil and Gas Recovery Conference, March 18-20, Midland, TX.

Hundere, I. 1984. The Effect of Freezing on Unconsolidated Core Ma¬terial from Troll Field. Internal paper, Saga Petroleum A/S, Oslo.

Ide, J.M., 1936. The elastic properties of rocks: A correlation of theory and experiment. Proceedings of the National Academy of Sciences of the United States of America 22, 482.

Jaeger, J. Cook, N. G., and Zimmerman, R. 2007. Fundamentals of Rock Mechanics, 4th edition, Malden, MA: Blackwell Pub.

Jones, S. C. 1997. A Technique for Faster Pulse-Decay permeability Measurements in Tight Rocks. SPE 28450.

K. Terzaghi. 1936. The shearing resistance of saturated soil, Proceeding of the First International Conference in Soil Mechanics V1 (1936) 54–56.

K. Terzaghi. 1943. Theoretical soil mechanics, J. Wiley & Sons, inc.

Karcher, B. J., Giger, F. M., and Combe, J. 1986. Some Practical Formulas To Predict Horizontal Well Behavior. Society of Petroleum Engineers. doi:10.2118/15430-MS

Khatchikian, A. 1996. Deriving Reservoir Pore-Volume Compressibility From Well Logs. SPE Advanced Technology Series. Vol. 4, No. 1, p. 14-20.

Kindt, R.K. 1985. The Effect of Freezing on Permeability of Uncon¬solidated Sandstones – An Experimental Investigation. Norwegian Institute of Technology, Trondheim, Norway.

Kranz, R. L., Saltzman, J. S., and Blacic, J. D. 1990. Hydraulic diffusivity measurements on laboratory rock samples using an oscillating pore pressure method. International Journal of Rock Mechanics and Mining Sciences & Geomechanics Abstracts 27, p. 345-352.

Labuz, J.F., L.H. Chen, and Cattaneo S. 2001. Fracture of rock from wedge indentation. In the 38th U.S. Symposium on Rock Mechanics (USRMS), Washington, D.C. 7-10 July, 2001.

Landes, K. 1970. Petroleum Geology of the United States. John Wiley and Sons, New York.

Lantz, T. Greene, D. Eberhard, M., Norrid, S. and Pershall, R. 2007. Refracturing Treatments

Law, B. E., and Spencer, C. W. 1993. Gas in tight reservoirs-an emerging major source of energy. The Future of Energy Gasses, US Geological Survey, Professional Paper1570, P233-252.

Lee, w. J. 1982. Well Testing. SPE Text book Series V1, p.13-15.

LeFever, J. A. 1991. History of oil production from the Bakken Formation, North Dakota, in, W. B. Hansen, ed., Montana geological Society 1991 Guidebook to Geology and Horizontal Drilling of the Bakken Formation, Billings, MT, pp. 3-17.

Li, C., X. Chen, and Z. Du. 2004. A New Relationship of Rock Compressibility with Porosity. SPE 88464-MS, in SPE Asia Pacific Oil and Gas Conference and Exhibition, Perth, Australia, 18-20 October 2004.

Lin, D., and Fairhurst, C. 1991. The Topological Structure of Fracture Systems In Rock. American Rock Mechanics Association.

Lin, Q., Labuz, J. F., and Cattaneo, S. 2010. Digital Image Correlation And the Fracture Process In Rock. American Rock Mechanics Association.

Ling, K. 2012. Correlation between Rock Permeability and Formation Resistivity Factor-A Rigorous and Theoretical Derivation. In the SPE Middle East Unconventional Gas Conference and Exhibition. Abu Dhabi, UAE. 23-25 January, 2012.

Locker, D.A. 1993. Acoustic Emission And Rock Fracture. In the 34th U.S. Symposium on Rock Mechanics (USRMS), Madison, Wisconsin. 28-30 June, 1993.

Look2See1. 2015. Williston Basin. [WWW page]. URL https://en.wikipedia.org/wiki/Williston_Basin

Macini, P. and E. Mesini. 1998. Static and Dynamic Reservoir Rock Compressibility at High Pressure. SPE 49549-MS, in SPE Abu Dhabi International Petroleum Exhibition and Conference, Abu Dhabi, United Arab Emirates, 11-14 November 1998.

Marchina, P., Brousse, A., Fontaine, J., Dano, C., and Alonso, C. 2004. In-situ Measurement of Rock Compressibility in a Heavy Oil Reservoir. SPE 86940-MS, in SPE

Mashinsky, E.I., 2003. Differences between static and dynamic elastic moduli of rocks: Physical causes. Differences 44, 953–959.

Mavko, G., Mukerji, T., and Dvorkin, J., 2009. The rock physics handbook tools for seismic analysis of porous media. Cambridge University Press, Cambridge, UK; New York.

McLatchie, A. S., Hemstock, R. A., and Young, J. W. 1958. The Effective Compressibility of Reservoir Rock and Its Effects on Permeability. Society of Petroleum Engineers. doi:10.2118/894-G.

Metwally, Y. M. and Sondergeld, C. H. 2011. Measuring low permeabilities of gas-sands and shales using a pressure transmission technique. International Journal of Rock Mechanics & Mining Sciences, p. 1135-1144.

Mukherjee, H., and Economides, M. J. 1991. A Parametric Comparison of Horizontal and Vertical Well Performance. Society of Petroleum Engineers. doi:10.2118/18303-PA

Neaupane, K., Yamabe, T. and Yoshinaka, R. 1999. Simulation of a fully coupled thermo-hydro-mechanical system in freezing and thawing rock. International Journal of Rock Mechanics and Mining Sciences, 36: 563-580.

Nelson, R.A. 1976. An Experimental Study of Fracture Permeability in Porous Rock. In the 17th U.S. Symposium on Rock Mechanics (USRMS), Snow Bird, Utah. 25-27 August, 1976.

Newman, G.H. 1973. Pore-Volume Compressibility of Consolidated, Friable, and Unconsolidated Reservoir Rocks Under Hydrostatic Loading. Journal of Petroleum Technology. Vol. 25, No. 2, p. 129-134.

Nordeng, S.H., 2010, A brief history of oil production from the Bakken Formation in the Williston Basin: Geo News, v. 37, no. 1, p. 5-9.

Nur, A., and J. D. Byerlee. 1971. An exact effective stress law for elastic deformation of rock with fluids, J. Geophys. Res., 76(26), 6414–6419

Passey, Q.R., Bohacs, K.M., Esch, W.L., Klimentidis, R., and Sinha, S. 2010. From Oil-Prone Source Rock to Gas-Producing Shale Reservoir-Geologic and Petrophysical Characterization of Unconventional Shale-Gas Reservoirs. SPE 131350 presented at the CPS/SPE International Oil& Gas Conference and Exhibition,

Petrowiki, Compreissibility definition, http://petrowiki.org/Compaction_drive_reservoirs

Plona, T. J. J., and Cook, J. M. J. 1995. Effects of stress cycles on static and dynamic Young's moduli in Castlegate sandstone. American Rock Mechanics Association.

Poisson's Ratio. 2007. http://www.pavementinteractive.org/article/poissons-ratio

Pollastro, R. M., T. A. Cook, L. N. R. Roberts, C. J. Schenk, M. D. Lewan, L. O. Anna, S. B. Gaswirth, P. G. Lillis, T. R. Klett, and R. R. Charpentier, 2008, Assessment of undiscovered oil resources in the Devonian-Mississippian Bakken Formation, Williston Basin Province, Montana and North Dakota, 2008: U.S. Geological Survey Fact Sheet 2008-3021, 2 p.

Poston, S.W. and H.Y. Chen. 1987. The Simultaneous Determination of Formation Compressibility and Gas-in-Place in Abnormally Pressured Reservoirs. SPE 16227, in SPE Production Operations Symposium, Oklahoma City, Oklahoma, 8-10 March 1987.

Price, L.C. 2000. Origin and Characteristics of the Basin-Centered Continuous-Reservoir Unconventional Oil-resource Base of Bakken Source System, Williston Basin. Energy and Environmental research Center

Qiao, L. P., Wong, R. C. K., Aguilera, R., and Kantzas, A. 2012. Determination of Biot's Effective-Stress Coefficient for Permeability of Nikanassin Sandstone. Society of Petroleum Engineers. doi:10.2118/150820-PA

Salehi, I. A., & Ciezobka, J. 2013. Controlled Hydraulic Fracturing of Naturally Fractured Shales - A Case Study in the Marcellus Shale Examining How to Identify and Exploit Natural Fractures. In the SPE Unconventional Resources Conference-USA, The Woodlands, Texas, USA. 10-12 April, 2013.

Samson Resources Company. 2006. CMS-300 Conventional Plug Analysis (Corelab Report, Core Lab File No. Hou-060143). April 24, 2006. In Well File # 16089, Well File Retrieved from North Dakota Industrial Commission, Oil and Gas Division Database. https://www.dmr.nd.gov/oilgas/subscriptionservice.asp.

Sanyal, S., Marsden, S. and Ramey, H., 1974. Effect of temperature on petrophysical properties of reservoir rocks. Paper SPE 4898 presented at the SPE California Regional Meeting, San Francisco, California, 4-5 April.

Sinha, S., Braun, E.M., Passey, Q.R., Leonardi, S.A., Wood, A.C., Zirkle, T., Boros, J.A., and Kudva, R.A. 2012. Advances in Measurement Standards and Flow Properties Measurements for Tight Rocks such as Shales. SPE 152257-MS, SPE/EAGE European Unconventional Resources Conference and Exhibition, 20-22 March, Vienna, Austria

Skempton,A W. 1961. Effective stress in soil, concrete and rocks, Pore Pressure and Suction in Soils (1961) 4–16.

Sloss, L. L. , 1963, Sequences in the cratonic interior of North America: Geological Society of America Bulletin, v. 74, p. 93-114.

Somerton, W.H., Mehta, M.M. and Dean, G.W. 1965. Thermal Alteration of Sandstones. Journal of Petroleum Technology, May 1965: 589-593.

Sone, H., Zoback, M.D., 2013. Mechanical properties of shale-gas reservoir rocks — Part 1: Static and dynamic elastic properties and anisotropy. GEOPHYSICS 78, D381–D392.

Stanchits S., A. Surdi, E. Edelman, and R. Suarez-Rivera. 2012. Acoustic Emission And Ultrasonic Transmission Monitoring of Hydraulic Fracture Propagation In Heterogeneous Rock Samples. In the 46th U.S. Rock Mechanics/Geomechanics Symposium, Chicago, Illinois. 24-27 June, 2012.

Suman, A. 2009. Uncertainties in Rock Pore Compressibility and Effects on Seismic History Matching. Master Thesis, Stanford University.

Thorpe, R.K. 1981. An Example Of Fracture Characterization In Granitic Rock. In the 22nd U.S. Symposium on Rock Mechanics (USRMS), Cambridge, Massachusetts. 29 June-2 July, 1981.

Tian, H., Kempka, T. and Schluter, R., et al. 2009. Influence of high temperature on rock mass surrounding in situ coal conversion sites. Proceedings of the 10th International Symposium on Environmental Geotechnology and Sustainable Development, Bochum, Germany, 7-11 September.

Tinni, A., Fathi, E., Agarwal, R., Sondergeld, C., Akkutlu, Y., and Rai, C. 2012. Shale Permeability Measurements on Plugs and Crushed Samples. SPE 162235, Canadian Unconventional Resources Conference, 30 October-1 November 2012, Calgary, Alberta, Canada.

Torsaeter, O. and Beldering, B. 1987. The effect of freezing of slightly consolidated cores. SPE Formation Evaluation, 2 (3): 357-360. Paper SPE 14300-PA.

Triab, D., and Donaldson, E. C. 2004. Petrophysics (second edition): Theory and Practic of Measuring Reservoir Rock and Fluid Transport Properties. Amesterdam: Gulf Professional publishing.

Van der Knaap, W. 1959. Nonlinear Behavior of Elastic Porous Media, Petroleum Transactions. AIME, Vol. 216, p. 179-187.

Vincent, M.C. 2011. Optimizing Transverse Fractures in Liquid-Rich Formations. SPE 146376, SPE Annual Technical Conference and Exhibition held in Denver, Colorado, USA, 30 October–2 November 2011

Vodak, F., Trtik, K. and Kapickova, O., et al. 2004. The effect of temperature on strength – porosity relationship for concrete. Construction and Building Materials, 18: 529-534.

Wang, Z. and Nur, A. (eds.), 2000. Seismic and Acoustic Velocities in Reservoir Rocks, vol. 3,Recent Developments, Geophysics Reprint Series, no. 19. Tulsa, OK: Society of Exploration Geophysicists.

Yao, T., Li, J. and Huang, Y. 2012. Effects of temperature and stress on porosity and permeability reservoir. Journal of Shenzhen University Science and Engineering, 29 (2):154-158.

Yildiz, T. 1998. Prediction of In-Situ Formation Compressibility from Production Data, SPE 47379-MS, in SPE/ISRM Rock Mechanics in Petroleum Engineering, Trondheim, Norway, 8-10 July 1998.

Yuan, Z., Schubert, J., Teodoriu, C., and Gardoni, P. 2012. HPHT Gas Well Cementing Complications and its Effect on Casing Collapse Resistance. Paper SPE153986 presented at the SPE Oil and Gas India Conference and Exhibition, 28-30 March 2012, Mumbai, India.

Zhou, xuejun. 2011. Geomechanical Stability Analysis for C02 Sequestration in Carbonate Formation. PhD Dissertation, North Dakota University (May, 2011)

Zimmerman, R. W., W. H. Somerton, and M. S. King. 1986. Compressibility of Porous Rocks. Journal of Geophysical Research. Vol. 91, No. B12, p. 12765-12777.

Zoback, M. D., and Byerlee, J. D. 1975. Permeability and Effective Stress: GEOLOGIC NOTES. AAPG Bulletin, 59(1), 154-158.

NOMENCLATURE

A	:	area of the cross section of the core plug
AU	:	assessment unit
C	:	constant linear coefficient
C		rock cohesion
C_{f}	:	formation compressibility
C_g	:	gas isothermal compressibility
cp	:	centipoise
C_t	:	total compressibility
D	:	Darcy
D	:	diameter of core
D_{core}	:	core diameter
DOE	:	U.S. Department of Energy
E_{dynamic}	:	dynamic Young's modulus
$\mathrm{E_{static}}$	:	static Young's modulus
$f_{i,mineral}$	:	volumetric fraction of mineral i in total matrix
G	:	shear modulus
GPa	:	gigapascal
GRI	:	Gas Research Institute
ϕ	:	porosity, or original porosity

$\phi_{freezer\ temperature}$	:	porosity at freezer temperature
$\phi_{original}$	:	original porosity
k	:	permeability
K	:	bulk modulus of the rock
K_s	:	matrix modulus of the rock
L	:	length of core
L_{core}	:	length of core
M	:	molecular weight
$m(p)$	:	gas pseudopressure
mD	:	milli-darcy
MPa	:	megapascal
n	:	exponential coefficient
n_1	:	gas moles in Chamber 1
n_2	:	gas moles in Chamber 2
ND	:	North Dakota
nD	:	nano-Darcy
NDIC	:	North Dakota Industial Commission
OOIP	:	original oil in place
p	:	pressure
p_1	:	initially the pressure in Chamber 1
p_1	:	upstream reservoir pressure
p_1	:	pressure at Chamber 1
p_2	:	initially the pressure in Chamber 2

p_2	:	downstream reservoir pressure
p_2	:	pressure at Chamber 2
p_3	:	pressure at Chambers 1 and 2 after pressure reaches equilibrium
p_b	:	base pressure
p_c	:	confining pressure
Pp	:	pore pressure
P-wave	:	primary wave
Q	:	strength of the instantaneous pressure disturbance
q_g	:	gas rate
R	:	universal gas constant
s	:	slope of the pressure difference in a logarithm as a function of time
S_w	:	water saturation
S-wave	:	secondary wave
T	:	temperature
t	:	time
T_1	:	temperature at Chamber 1
T_2	:	temperature at Chamber 2
T_3	:	temperature at Chambers 1 and 2 after pressure reaches equilibrium
$T_{freezer}$	:	freezer temperature
$T_{freezing\ point}$	:	water freezing temperature
t_m	:	time at which the pressure disturbance is a maximum at x
UND	:	University of North Dakota

USGS	:	United States Geological Survey
v	:	Poisson’s ratio
$v_{dynamic}$	:	dynamic Poisson’s ratio
v_{static}	:	Static Poisson's ratio
V_1	:	volume of the upstream reservoir
V_1	:	volume of chamber 1 + pipeline volume between Gas Inlet Valve and Gas Outlet Valve
V_2	:	volume of the downstream reservoir
V_2	:	volume of chamber 2 (without core) + pipeline volume between Gas Outlet Valve and Gas Vent Valve
$V_{bulk,\ core}$	:	bulk volume of core
$V_{chamber\ 1}$	:	volume of chamber 1
$V_{chamber\ 2}$	:	volume of chamber 2 (without core)
V_{ice}	:	ice volume
$V_{original}$	:	original volume
V_{water}	:	water volume
V_p	:	pore volume of the core
V_p	:	velocity of P-wave
V_s	:	velocity of S-wave
v_x	:	gas velocity in x direction
x	:	distance from original point in x direction
z	:	gas z-factor
z_1	:	gas z-factor at Chamber 1
z_2	:	gas z-factor at Chamber 2

z_3	:	gas z-factor at Chambers 1 and 2 after pressure reaches equilibrium
α	:	Biot's coefficient
$\alpha_{i,mineral}$	:	coefficient of thermal expansion of mineral *i*
α_{ice}	:	coefficient of thermal expansion of ice
ε	:	strain
ε_1	:	first principal normal strain
ε_2	:	second principal normal strain
ε_3	:	third principal normal strain
ε_a	:	strain of specimen in axial direction
ε_r	:	strain of specimen in radial direction
ε_v	:	volumetric strain
ρ_g	:	gas density
σ	:	stress
σ'	:	effective stress
σ_1	:	first principal normal stress
σ_2	:	second principal normal stress
σ_3	:	third principal normal stress
τ	:	shear strength
τ_m	:	mean stress
μ	:	viscosity
μ	:	coefficient of internal friction
μ_g	:	gas viscosity

μD	:	micro-Darcy
Δp	:	pressure difference
Δp_c	:	Variation of the confining pressure
Δp_P	:	Variation of the pore pressure
$\Delta \varepsilon_v$	:	variation of the volumetric strain
$\Delta \sigma'$	:	variation of the effective stress
Δt	:	time period
ΔV	:	variation of the total rock volume
ΔV	:	volume change
$\Delta V_{contraction,\ matrix}$	:	matrix contraction volume
$\Delta V_{contraction,ice}$	:	ice contraction volume
$\Delta V_{expansion}$	:	expansion volume due to water phase change
$\Delta V_{i,,mineral}$	:	mineral i contraction volume
ΔV_p	:	variation of the pore volume
ΔV_{total}	:	total volume change
Δx	:	incremental distance in x direction